JULY 2023

Ph.D. in Mechanical Engineering

MUSA YILMAZ

REPUBLIC OF TÜRKİYE

GAZİANTEP UNIVERSITY

GRADUATE SCHOOL OF NATURAL & APPLIED SCIENCES

AGENT-BASED DUAL NEEDLE ADDITIVE MANUFACTURING OF POLYMERIC FILAMENTS IN DIFFERENT ALIGNMENTS FOR MANUFACTURING COMPOSITES

Ph.D. THESIS

IN

MECHANICAL ENGINEERING

BY

MUSA YILMAZ

JULY 2023

AGENT-BASED DUAL NEEDLE ADDITIVE MANUFACTURING OF POLYMERIC FILAMENTS IN DIFFERENT ALIGNMENTS FOR MANUFACTURING COMPOSITES

Ph.D. Thesis

in

Mechanical Engineering

Gaziantep University

Supervisor

Prof. Dr. Necip Fazıl YILMAZ

Co-Supervisor

Asst. Prof. Dr. Ali KILIÇ

by

Musa YILMAZ

July 2023

AGENT-BASED DUAL NEEDLE ADDITIVE MANUFACTURING OF POLYMERIC FILAMENTS IN DIFFERENT ALIGNMENTS FOR MANUFACTURING COMPOSITES

submitted by **Musa YILMAZ** in partial fulfillment of the requirements for the degree of Doctor of Philosophy in **Mechanical Engineering Department, Gaziantep University** is approved by,

Prof. Dr. Mehmet İshak YÜCE
Director of the Graduate School of Natural and Applied Sciences …….....

Prof. Dr. Mehmet Sait SÖYLEMEZ
Head of the Department …….....

Prof. Dr. Necip Fazıl YILMAZ
Supervisor …….....

Asst. Prof. Dr. Ali KILIÇ
Co-Supervisor, Mechanical Engineering
Gaziantep University …….....

Exam Date: 7 July 2023

Examining Committee Members:

Prof. Dr. Ömer EYERCİOĞLU
Gaziantep University …….....

Prof. Dr. Necip Fazıl YILMAZ
Gaziantep University …….....

Prof. Dr. Oğuzhan YILMAZ
Gazi University …….....

Prof. Dr. Ali Rıza YILDIZ
Bursa Uludağ University …….....

Prof. Dr. Ali Tolga BOZDANA
Gaziantep University …….....

I hereby declare that all information in this document has been obtained and presented in accordance with academic rules and ethical conduct. I also declare that, as required by these rules and conduct, I have fully cited and referenced all material and results that are not original to this work.

Musa YILMAZ

ABSTRACT

AGENT-BASED DUAL NEEDLE ADDITIVE MANUFACTURING OF POLYMERIC FILAMENTS IN DIFFERENT ALIGNMENTS FOR MANUFACTURING COMPOSITES

YILMAZ, Musa
Ph.D. in Mechanical Engineering
Supervisor: Prof. Dr. Necip Fazıl YILMAZ
Co-Supervisor: Asst. Prof. Dr. Ali KILIÇ
July 2023
155 pages

Additive manufacturing, a rapidly growing production technology in the industrial sector, offers significant advantages for complex geometry production through methods such as fused deposition modeling (FDM). However, polymer parts produced via FDM often exhibit low strength, which limits their practical application. This thesis focuses on improving the mechanical properties of additive manufacturing parts produced using 3D printers. The research investigates diverse strategies to increase the strength of FDM products. A central focus of the thesis is the development of a novel composite material utilizing peroxide as a reinforcement agent and the finding of a regional-based strength-enhancing method during production by cross-linking peroxide and polymer. The 3D printing system enables in-situ composite production, allowing for partial strengthening through agent-based reinforcement while considering stress concentration in the manufactured part. Experimental observations reveal the occurrence of a chemical reaction between the polymer and peroxide materials, resulting in the formation of cross-linking. Additionally, other strategies such as different fiber alignments in pre-production and annealing in post-production were conducted to investigate their impact on the mechanical properties of additive manufacturing products. The findings from both pre-production and post-production interventions demonstrate significant improvements in the mechanical properties of the 3D-printed products.

Key Words: Additive Manufacturing, Agent-Based Production, Composite, Cross-Linking, Peroxide

ÖZET

FARKLI HİZALANMIŞ POLİMERİK FİLAMENTLERİN ÇİFT BAŞLIK KULLANARAK EKLEMELİ İMALAT YÖNTEMİYLE AJAN TABANLI KOMPOZİT ÜRETİMİ

YILMAZ, Musa
Doktora Tezi, Makine Mühendisliği
Danışman: Prof. Dr. Necip Fazıl YILMAZ
İkinci Danışman: Dr. Öğr. Üyesi Ali KILIÇ
Temmuz 2023
155 sayfa

Eklemeli imalat, endüstriyel sektörde kullanımı günden güne hızla artan bir üretim teknolojisi olup, eriyik yığma modelleme (EYM) gibi yöntemlerle karmaşık geometri üretimi için önemli avantajlar sunmaktadır. Bununla birlikte, EYM ile üretilen parçaların pratik uygulamalarda kullanımı düşük mukavemet sebebinden dolayı sınırlı olmaktadır. Bu tez, 3B yazıcılar kullanılarak üretilen parçalarının mekanik özelliklerinin iyileştirilmesi için farklı stratejiler üzerine odaklanmaktadır. Tezin ana odak noktası, peroksit katkılı yeni bir kompozit malzeme çalışmaları ve peroksitle polimerin çapraz bağ oluşturması ile üretim esnasında bölgesel bazlı mukavemet artırıcı yöntemin bulunmuş olmasıdır. Geliştirilen 3B yazıcı sistemi in-situ olarak kompozit üretimi yapabilmekle beraber üretilen parçadaki gerilme konsantrasyonunu dikkate alarak ajan tabanlı olarak yani kısmı güçlendirme ile kompozit üretimine olanak sağlamaktadır. Deneysel gözlemler, polimer ve peroksit malzeme arasında kimyasal reaksiyonun gerçekleştiğini ve bunun sonucunda çapraz bağlanmanın oluştuğunu ortaya koymaktadır. Ayrıca, fiberlerin farklı hizalanması gibi üretim öncesinde ve tavlama işlemi gibi üretim sonrası müdahale ile EYM ürünlerinin mekanik özelliklerindeki değişim araştırılmıştır. Hem üretim öncesi hem de üretim sonrası yapılan bu çalışmaların sonucunda, 3B basılı ürünlerin mekanik özelliklerinde dikkate değer gelişmeler saptanmıştır.

Anahtar Kelimeler: Eklemeli İmalat, Ajan-Tabanlı Üretim, Kompozit, Çapraz Bağlama, Peroksit

''Dedicated to my family''

ACKNOWLEDGEMENTS

I would like to express my deepest gratitude to my esteemed thesis supervisor, Prof. Dr. Necip Fazıl Yılmaz, for his invaluable guidance, unwavering support, and profound expertise throughout the entirety of this thesis. I am truly appreciative of his insightful feedback, constructive criticism, and continuous motivation, which have significantly enriched the quality and depth of this work.

Furthermore, I extend my heartfelt appreciation to my co-supervisor, Asst. Prof. Dr. Ali Kılıç, for his invaluable guidance and support throughout the course of my thesis. Additionally, I would like to express my sincere gratitude to Prof. Dr. Hidayet Mazı for his valuable contributions and insightful suggestions. I am immensely grateful for the helpful contributions, profound discussions, and unwavering support provided by Assoc. Prof. Dr. Abdulcabbar Yavuz throughout my thesis. Her friendship and support have been instrumental in shaping my research direction.

I also extend my profound gratitude to Prof. Dr. Krzysztof Jan Kurzydłowski from the Bialystok University of Technology and Prof. Dr. Cezary Rapiejko from the Lodz University of Technology for providing me with laboratory opportunities in Poland.

I would like to acknowledge the Scientific Research Projects Unit (BAPYB) of Gaziantep University for its financial support of my study (Project numbers: MF.DT.22.28 and MF.HZP.22.13).

Most importantly, I would not have been able to embark on this effort without the unwavering support of my family. Despite the physical distance, my parents, sister, and brother have consistently encouraged me with their love and have motivated me throughout my Ph.D. I extend my heartfelt gratitude to my wife, Fatma Zehra, driving me to work diligently every day toward completing this work. Her selflessness and

sacrifices have allowed me to focus on my studies and provided me with the strength to overcome the associated challenges.

Finally, thank you my daughter, Zümra, for making my life happy and wonderful, particularly during the final months of my doctoral journey. Her innocent interruptions, as she knocked on my study room's door and beckoned me away from my desk, insisting that I join her in play and momentarily disrupt my work, have been lovely and sweet. Despite my reminders of the importance of my studies, her irresistible sweetness has effortlessly sabotaged my focused efforts, reminding me of the precious moments that truly matter.

TABLE OF CONTENTS

LIST OF TABLES

Page

LIST OF FIGURES

Page

LIST OF ABBREVIATIONS

3D	Three Dimensional
3DP	Three-Dimensional Printing
ABS	Acrylonitrile Butadiene Styrene
AM	Additive Manufacturing
BJ	Binder Jetting
BPO	Benzoyl Peroxide
CAD	Computer-Aided Design
CAM	Computer-Aided Manufacturing
CDLP	Continuous Digital Light Processing
CF	Carbon Fibers
CNTs	Carbon Nanotubes
DIW	Direct Ink Writing
DLP	Digital Light Processing
DMLS	Direct Metal Laser Sintering
DOD	Drop On Demand
DPE	Direct Pellet Extrusion
DSC	Differential Scanning Calorimetry
e-3D	Embedded 3D Printing
EBAM	Electron Beam Additive Manufacturing
EBM	Electron Beam Melting
FDM	Fused Deposition Modeling
FEA	Finite Element Analysis
FFF	Fused Filament Fabrication
FTIR	Fourier Transform Infrared Spectroscopy
HDPE	High-Density Polyethylene
HL	Holographic Lithography
IJP	Inkjet Printing
IoT	Internet of Things

LENS	Laser-Engineered Net Shaping
LOM	Laminated Object Manufacturing
MEX	Material Extrusion Technique
MJM	MultiJet Modelling
PμSL	Projection Micro Stereo-Lithography
PBAT	Poly (Butylene Adipate-Co-Terephthalate)
PBF	Powder Bed Fusion
PE	Polyethylene
PEEK	Polyetheretherketone
PEI	Polyetherimide
PEI	Polyetherimide
PLA	Polylactic Acid
PVA	Polyvinyl Acetate
SEM	Scanning Electron Microscopy
SGC	Solid Ground Curing
SLA	Stereolithography
SLM	Selective Laser Melting
SLP	Selective Laser Printing
SLS	Selective Laser Sintering
STL	Standard Tessellation Language
UV	Ultraviolet
XRD	X-Ray Diffraction

CHAPTER 1

INTRODUCTION

Manufacturing is today experiencing profound transformations driven by megatrends that have far-reaching implications for both people and industry. These megatrends, described by their long-term and transformative nature, include a wide range of factors that are shaping the future of manufacturing [1], [2]. Improvements in digitalization and the emergence of Industry 4.0 have revolutionized manufacturing processes through the integration of technologies such as big data, the Internet of Things (IoT), and cyber-physical systems [3]–[8]. Concurrently, sustainable manufacturing procedures and the adoption of circular economy codes have gained a certain traction, concentrating on resource efficiency, waste reduction, and environmental stewardship [9]. Additive manufacturing, or 3D printing, has emerged as a disruptive technology that enables on-demand and customized production, while smart manufacturing techniques improve operational efficiency through the utilization of interconnected systems and real-time data [10]. Also, agile and flexible production techniques, optimized global supply chains, and the pursuit of human-centric approaches are reshaping the manufacturing landscape [11]. Understanding and harnessing these megatrends are crucial to manufacturers in terms of remaining competitive, driving innovation, and adapting to the changing needs of a rapidly growing industry.

The advent of Industry 4.0, also known as the Fourth Industrial Revolution, has brought about significant advancements in production and manufacturing technologies [11], [12]. Additive manufacturing is recognized as a pivotal technology within the context of Industry 4.0, which involves the integration of digital technologies and automation into manufacturing processes. It may be considered a key enabler of Industry 4.0 due to its ability to transform traditional manufacturing methods and facilitate the adoption of advanced production techniques [11], [13].

This technology is revolutionizing the manufacturing landscape by offering enhanced customization, increased design freedom, and improved efficiency, thereby contributing to the realization of Industry 4.0's vision for highly connected and automated production systems [14], [15].

Smart production methods are revolutionizing the manufacturing sector by introducing innovative approaches that significantly transform traditional production processes [6], [16]. These methods aim to enhance operational efficiency through real-time data utilization and interconnected systems, thereby optimizing production processes. The adoption of smart manufacturing methods is increasingly widespread, offering companies a competitive edge and paving the way for future industrial transformation [17].

In today's rapidly evolving technological landscape, the continuous development of innovative machines is imperative to enhance functionality, efficiency, and quality, while reducing costs and enabling more flexible production processes. The advantages of developing new machines encompass improved performance, enhanced precision and repeatability, accelerated production, and reduced energy consumption [18]. Moreover, the development of new machines stimulates industry innovation, unlocks novel opportunities, and drives industrial transformation. Thus, the ongoing enhancement of machines and the design of new machines offering innovative solutions are pivotal to the success of modern manufacturing [19].

Additive manufacturing is recognized as one of the most promising technologies in the manufacturing industry. Additive manufacturing is a process whereby products are built layer by layer using digital data [20]–[23]. It allows for digital control of the production process and direct manufacturing of parts from design specifications. Industry 4.0 aims to achieve customized production and shorter lead times, which can be facilitated through the use of additive manufacturing technology. Industry 4.0 enhances the potential of additive manufacturing, and in turn additive manufacturing serves as one of the application areas of Industry 4.0 [24]. By incorporating sensors, data analytics, artificial intelligence, and other digital technologies, additive manufacturing processes can become smarter and more connected [25], [26]. This enables more flexible, efficient, and optimized production processes. In summary,

there is a mutually beneficial relationship between Industry 4.0 and additive manufacturing [26]. Industry 4.0 enables the digitalization and automation of additive manufacturing processes, while additive manufacturing serves as a production technology that supports the goals of Industry 4.0 [27].

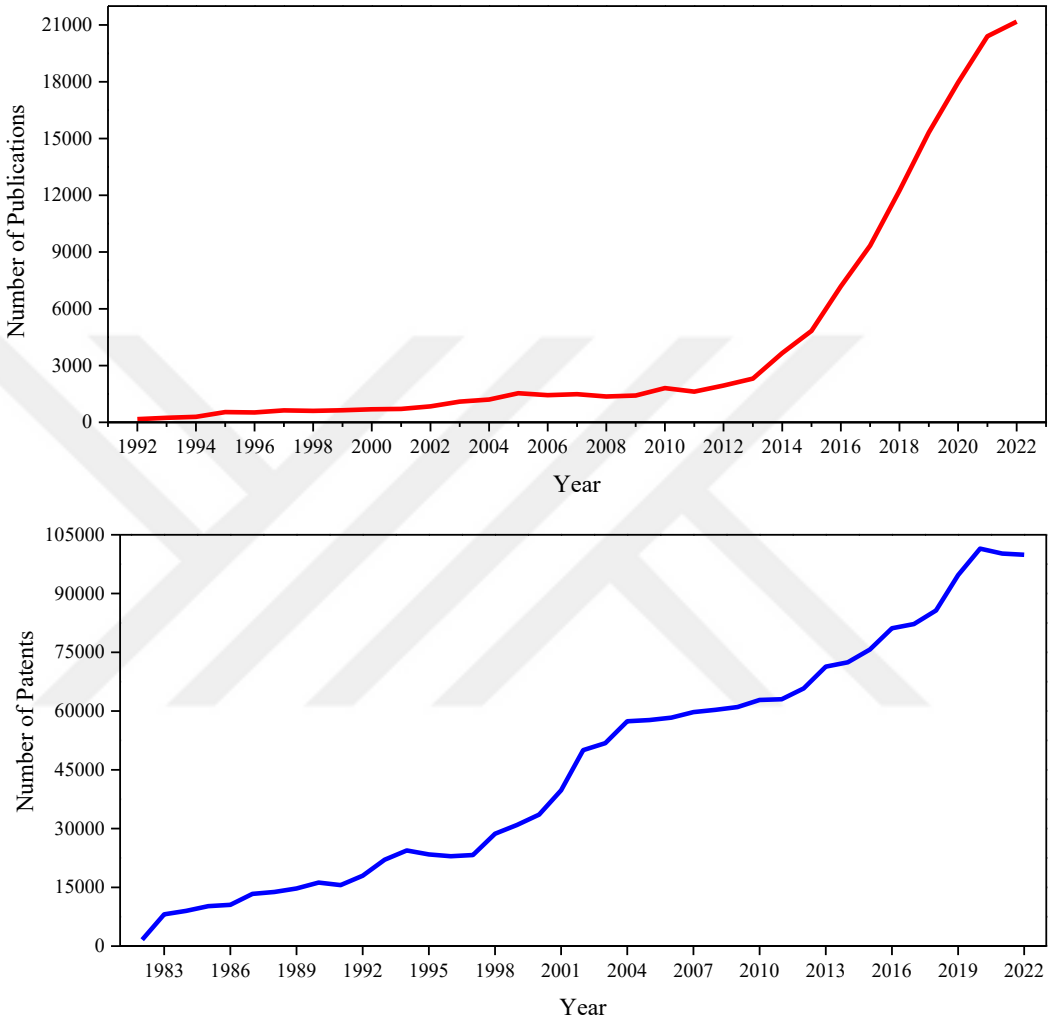

Figure 1. 1 The annual trend in publications and patents related to additive manufacturing over recent years (Extracted from Scopus with search terms: "additive manufacturing, 3D printing, and rapid prototyping") [28]

In recent years, with its numerous advantages and transformative potential, additive manufacturing has garnered significant attention both in industry and academia [29]. Additive manufacturing has experienced substantial growth and progress; indeed, this period has witnessed the commercialization of new methods and devices and a surge in scientific research. Figure 1. 1 depicts the tends in publications and patents related to additive manufacturing in recent years, as observed through an analysis of

publications indexed in Scopus. The interest in additive manufacturing is rapidly advancing, as indicated by the significant number of patents and scientific publications dedicated to this technology. This data was obtained by examining the Scopus database only; from this, it can be seen that confidence in additive manufacturing has steadily grown, accompanied by notable improvements in the efficiency of additive manufacturing devices.

Additive manufacturing has emerged as a crucial technology with several distinct advantages over traditional manufacturing techniques. One fundamental advantage is the unparalleled design freedom it offers, allowing for the fabrication of complex and customized geometries that have previously been unattainable [30]–[34]. This capability is of particular utility in the aerospace, medical, and automotive industries, where intricate and lightweight structures are highly sought after [35]. Additive manufacturing is also notable for rapid prototyping, enabling faster product development cycles and reducing time-to-market. Moreover, it promotes sustainability by minimizing material waste since it is an additive process that selectively deposits materials layer by layer [36]. Additionally, the on-demand nature of additive manufacturing decreases inventory requirements and simplifies the supply chain [37], [38].

Nevertheless, despite these advantages, additive manufacturing does have its limitations. The material selection remains a challenge as not all materials can be effectively utilized in additive processes, limiting the range of available materials compared to traditional methods [39]–[41]. Surface finish and resolution can also be drawbacks, as additively manufactured parts may exhibit rougher surfaces and have lower resolution than conventionally manufactured parts [42]. Additionally, additive manufacturing may have some limitations in terms of the mechanical properties exhibited by the produced parts. These limitations manifest in relatively lower mechanical performance, which can impact the overall strength and durability of the components [43]. Furthermore, production speed can be a limiting factor for large-scale manufacturing, and additional post-processing steps may be required to achieve desired specifications [32]. While additive manufacturing continues to evolve and address these limitations, careful consideration of the current advantages and

limitations is crucial when determining its suitability for specific applications in various industries.

Enhancing the mechanical properties of products fabricated using additive manufacturing is a crucial objective. Presently, it is recognized that parts produced through particularly popular 3D printing techniques like Fused Deposition Modeling (FDM) exhibit limitations in terms of durability and strength [44], [45]. FDM has emerged as a popular additive manufacturing method for producing various products. It involves melting thermoplastic filament in a heated extruder head and depositing it layer by layer to create the desired object [46], [47]. FDM technology has achieved widespread adoption, particularly among hobbyists and in industrial settings, allowing for rapid prototyping in diverse fields such as automotive, defense, architecture, biomedical, aviation, and space [48], [49]. However, FDM-printed parts have limitations in terms of durability and are primarily suited for prototyping rather than functional or end-user applications [50]. While materials like polylactic acid (PLA) and acrylonitrile butadiene styrene (ABS) are commonly used in FDM printers, they offer relatively low strength [51]. Despite efforts to enhance mechanical properties by utilizing engineering materials such as polycarbonate (PC), polyetherimide (PEI), and polyether ether ketone (PEEK) at higher printing temperatures, achieving final product suitability remains a particular challenge. Although parts manufactured via the FDM technique may exhibit lower strength compared to their injection-molded counterparts, they still hold promise for various applications. Therefore, a comprehensive understanding of the mechanical behavior of FDM-printed products is necessary, allowing for a detailed assessment of their mechanical properties. To attain the desired enhancement in strength and enable the production of functional parts, it is necessary to improve the mechanical properties of products manufactured using 3D printers.

Efforts to enhance the mechanical properties of 3D-printed products involve the development of new/reinforced filament materials, or the implementation of additional processes during or after manufacturing. Although research aims to improve the mechanical properties of existing thermoplastic materials, the desired level of enhancement has not, to date, been achieved. The incorporation of composite materials and the integration of specialized reinforcements present a promising opportunity to enhance the mechanical properties of additive manufacturing parts. By combining

high-strength and lightweight materials, composites have the potential to enhance durability and enable the production of functional parts. As a result, there is a growing demand for 3D printers capable of producing composite materials, thus to some extent shifting the focus away from conventional thermoplastic-based printers [52]. Recent research has explored the development of 3D printers utilizing the FDM method, specifically designed to produce composite materials [53].

While incorporating engineering-grade materials like PC, PEI, and PEEK in FDM printing has shown marginal improvements in mechanical properties, these materials have not yet achieved the desired level of suitability for end-use applications [54], [55]. Consequently, there is a growing necessity to shift from standard thermoplastic-based 3D printers to ones capable of producing composite materials in order to attain the desired strength enhancement and facilitate the production of functional parts [52].

The mechanical strength of polymers is significantly compromised once they exceed their respective melting temperatures [56]. To mitigate the degradation of mechanical properties at elevated temperatures, various modifications have been explored for pristine PLA. Enhancement of the crystallinity of PLA can be achieved through annealing or the addition of nucleating agents. Additionally, chemical modifications of the PLA chain involve introducing new monomer units or functional groups. Cross-linking of polymer chains offers a promising avenue for improving mechanical properties and fostering the development of novel materials. Different methods, such as chemical cross-linking, peroxide cross-linking, ultraviolet (UV) cross-linking, and silane cross-linking, are commonly employed when polymer cross-linking is required. Among them, the chemical method, mainly using peroxides, is the most widely used. Peroxides are incorporated into the polymer via extrusion below the activation temperature of the peroxide [57]. Subsequently, the extruded cross-linked polymer undergoes curing under specific pressure or temperature conditions.

This study focuses on the fabrication of a novel composite material through peroxide reinforcement during the deposition of PLA filament using a 3D printer based on FDM technology. The primary objective is to enhance the strength properties by facilitating cross-linking in the PLA/peroxide composite system.

1.1 Motivation behind the Thesis

In the manufacturing sector, megatrends and smart manufacturing methods are transforming the industry, and with profound implications. Additive manufacturing, such as 3D printing, provides on-demand production and customization, while smart production techniques develop operations through real-time data utilization and interconnected systems. To effectively embrace and leverage these megatrends, innovation in additive manufacturing devices is crucial to the adaption of the dynamic manufacturing landscape.

The transformative potential of additive manufacturing is yet to be fully realized, as the implications of fabricating parts through additive processes, rather than subtractive methods, are still being explored. Despite the numerous advantages of 3D printing, such as its design flexibility and rapid prototyping capabilities, the strength characteristics of 3D-printed materials remain a key limitation. Compared to traditional manufacturing methods, 3D-printed materials often exhibit lower mechanical properties, including reduced tensile strength, flexural strength, and impact resistance. The inherent layer-by-layer deposition process of 3D printing introduces interlayer bonding weaknesses, resulting in anisotropic properties and reduced structural integrity. Moreover, the limited selection of printable materials available, typically thermoplastics with lower strength profiles, further contributes to the weakness of 3D-printed parts. Consequently, addressing the strength limitations of 3D-printed materials is imperative to maximizing the potential of additive manufacturing across diverse industries and applications.

Traditionally, FDM systems have been able to fabricate parts mostly from standard thermoplastics filament, and current FDM systems can print parts in a variety of engineering plastics. Although there have been recent advancements in FDM-based composite production, these systems are still limited in their capabilities. Furthermore, 3D-printed polymer products are predominantly utilized as conceptual prototypes, rather than functional components, due to their inferior strength and functionality as compared to fully functional and load-bearing parts.

1.2 Objectives of the Thesis

The main objectives of this thesis are to contribute to the scientific literature and industrial applications by realizing the following developments:

- The main aim of the current study is to develop a novel composite material for FDM additive manufacturing systems and an innovative 3D printing system utilizing an agent-based approach for printing this material. In essence, the objective is to create an intelligent production system that integrates the newly developed composite material and the agent-based 3D printing approach. The agent-based approach involves selectively incorporating a composite material, supplemented by an additional agent material, into regions of high-stress concentration that the part will encounter during application. Conversely, areas with lower stress concentrations are constructed using the matrix material alone. The findings of the research related to this aim have been accepted for publication in a scientific journal [58].

- On the other hand, the objective is to enhance the mechanical properties of 3D-printed products, specifically addressing the limitations related to strength. The focus lies on investigating strategies and techniques that can reinforce the structural integrity and durability of FDM-produced parts. To enhance the mechanical properties of 3D-printed parts, investigations focused on the process parameters of the 3D printer. Subsequently, post-production strengthening techniques were explored to enhance the performance of the printed parts further. The findings of the research related to this aim have been published in scholarly journals [59], [60].

1.3 Thesis Organization

This thesis is structured according to nine chapters, addressing key aspects related to the enhancement of strength in 3D-printed materials. The research focuses on layer alignments and post-processing methods for strength improvement, the development of a new composite material for 3D printing, and the design and manufacture of a specialized 3D printer capable of utilizing this material. The developed 3D machine exhibits agent-based and in-situ composite production capabilities. Each chapter

delves into specific areas of investigation, contributing to an in-depth understanding of the strength enhancement process in additive manufacturing. The content and layout of each chapter have been carefully planned to ensure a logical progression of ideas and facilitate the presentation of key findings. The following paragraphs offer a succinct overview of the content.

Chapter 1: Introduction

This chapter lays the foundation for the thesis by presenting an overview of the research topic, stating the research motivation, and providing a rationale for the study. The chapter concludes by outlining the subsequent chapters.

Chapter 2: Literature Survey

The literature survey chapter examines relevant literature and studies related to the thesis topic. It provides a comprehensive analysis of existing theories, concepts, and findings in the field. The review covers key research studies, theoretical frameworks, and methodologies employed by previous researchers. This chapter aims to establish the theoretical basis and context for the current study.

Chapter 3: Fundamentals of Additive Manufacturing

This section of the thesis provides a comprehensive overview of the underlying principles and essential concepts in additive manufacturing. It delves into the fundamental aspects of various additive manufacturing technologies, including their working principles, and the process parameters involved. This section explores the key advantages and limitations of additive manufacturing compared to traditional manufacturing methods, highlighting its potential for customization, rapid prototyping, and complex geometries. This chapter serves as a foundation for the subsequent chapters, laying the groundwork for the research and analysis conducted in the thesis.

Chapter 4: Material and Method

In this chapter, the research methodology employed in the study is detailed. It also justifies the chosen methodology by discussing its appropriateness with regard to addressing the research objectives and ensuring the reliability and validity of the findings.

Chapter 5: Design and Construction of an Agent-Based 3D Printing System

This section of the thesis presents the development and manufacturing of a novel 3D printing system with agent-based capabilities, providing an in-depth description of the design process and outlining the various components and functionalities incorporated into the system, especially the second nozzle. The construction phase is discussed, highlighting the technical considerations encountered during the implementation of the proposed design. The section concludes with a comprehensive overview of the agent-based features integrated into the 3D printing system, emphasizing the potential benefits and implications for the field of additive manufacturing.

Chapter 6: In-Situ Manufacturing of a Novel Cross-Linked Composite Material for Fused Deposition Modeling in Additive Manufacturing

This section of the thesis focuses on the development and application of a new cross-linked composite material specifically designed for the FDM technique in additive manufacturing. This section provides an overview of the research objectives and methodology employed to create the composite material. The section explores the synthesis process of the composite, discussing the selection of constituent materials, their compatibility, and the cross-linking mechanism employed. The in-situ manufacturing approach, which involves the production of the composite material during the 3D printing process itself, is emphasized as a novel and efficient method. The results are presented systematically, enabling the interpretation and discussion of the main findings. The implications of the results are discussed in relation to the research objectives, with references to the relevant literature. The section concludes by highlighting the potential applications and advantages of the developed cross-linked composite material in the field of additive manufacturing.

Chapter 7: Relation Between Layer Orientation and Mechanical Properties of 3D-printed Parts

This section presents the research findings on enhancing the mechanical properties of 3D-printed products through the process parameter. The results are presented in a clear and organized manner, facilitating the interpretation and discussion of key findings. The subsequent discussion section further scrutinizes the results in the context of the research objectives and the existing literature.

Chapter 8: Relation Between Annealing Process and Mechanical Properties of 3D-printed Parts

This section presents the research findings on improving the mechanical properties of 3D-printed products through post-processing. The results are presented systematically, enabling the interpretation and discussion of the main findings. The implications of the results are discussed in relation to the research objectives, with references to the relevant literature. The section concludes with recommendations for future research and potential practical applications in the field.

Chapter 9: Conclusion

The concluding chapter summarizes the main findings of the study and their implications. It restates the research objectives and highlights the contributions made by the research. The chapter also discusses the limitations of the study and suggests avenues for further research. Finally, it concludes with a concise summary of the overall study and its significance.

CHAPTER 2

LITERATURE SURVEY

2.1. Introduction

The literature review section of this thesis provides a comprehensive overview of existing theories, research, and scholarly discussions related to the topic at hand. It provides a critical examination and synthesis of the pertinent literature, highlighting key findings, methodologies, and theoretical frameworks.

2.2 Composite Materials Manufacturing

Developments in reinforced plastic composites fabricated with additive manufacturing have recently been consistently on the rise.

2.2.1 Additive Manufacturing of Composite Materials

Wang et al. [61] fabricated 3D-printed composite material composed of polylactic acid (PLA) and carbon nanotubes (CNTs) with the goal of enhancing its electromagnetic interference shielding properties. The 3D-printed PLA scaffold was immersed in an aqueous dispersion of CNTs using the dip-coating method. Subsequently, the CNT-coated PLA scaffold was subjected to hot compression at 10 MPa and 130°C for 10 minutes, followed by cold compression to prevent warping. The production process and its results are presented in Figure 2.1. The authors claimed that 3D printing technology is an effective and straightforward approach to enhancing the performance of conductive polymer composites in various applications, including radiation source fields and electronic devices. However, it has been found that conductive polymer composites exhibit worsened bending performance due to weak interface reactions between adjacent polymer domains, which are impeded by conductive fillers.

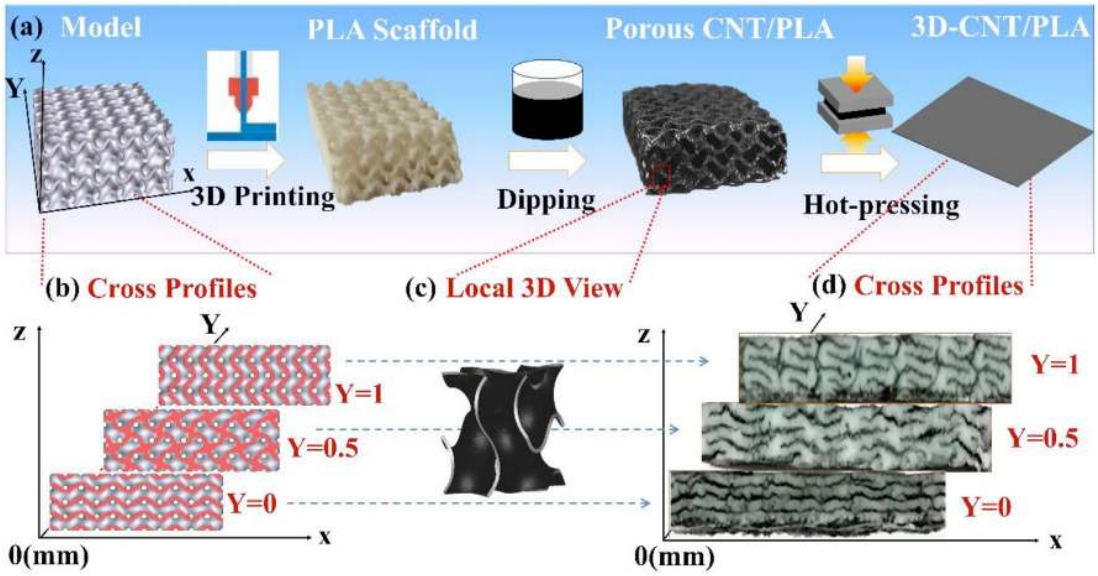

Figure 2.1 CNT/PLA composite preparation procedure [61]

Nikzad et al. [62] investigated the mechanical and thermal performance of new metal particle-reinforced acrylonitrile butadiene styrene (ABS) composites for applications in the fused deposition modeling (FDM) rapid prototyping process. Test samples of iron/ABS and copper/ABS composites with metal content of up to 40% by volume have been fabricated by controlled centrifugal mixing, and thermally compounded through a single-screw extruder and compression molding. It has been reported that the significant developments in ABS mechanical and thermal performance due to the incorporation of metallic particles could potentially promote the processing of superior-quality working prototypes on the market's FDM applications.

Shemelya et al. [63] focused on the manufacturing and characterization of tungsten-doped polycarbonate (PC) polymer matrix composites especially designed for X-ray radiation shielding applications. The manufacturing process, from tungsten functionalization to filament extrusion and material characterization, was investigated, including printability, estimation of gigahertz permittivity, and in terms of mechanical properties such as impact resistance, and tensile strength. The study findings indicate favorable enhancements in impact resistance, X-ray attenuation factor, and dielectric permittivity, as reported by the authors.

Mazlan et al. [64] conducted a study investigating the occurrence of defects, including warping effects, shrinkage, and poor dimensional accuracy, during the fabrication of 3D-printed PLA composite parts, which may adversely affect their functional

performance. Subsequently, the dimensional accuracy of the composite parts manufactured utilizing commercially available filaments of carbon fiber-reinforced PLA and wood-based PLA was compared with the PLA material. It was noted that the utilization of composite materials not only conferred favorable mechanical properties but also improved dimensional accuracy by enhancing dimensional stability during the printing process. Furthermore, the incorporation of composite materials mitigated the warping effects commonly observed in thermoplastic materials, including PLA.

Hwang et al. [65] conducted a comprehensive investigation of the thermomechanical properties of ABS composites reinforced with copper particles for use in 3D printing applications. This study's findings revealed that the composites' tensile strengths decreased with increasing amounts of metal particles. The authors attributed this reduction in tensile strength to the corresponding increase in voids and the disruption in bonding between the layers caused by the presence of copper particles.

Boparai et al. [66] compared the tribological properties of Nylon6/Al/Al_2O_3 and ABS objects printed using a 3D printer working with FDM. The tribological performance of parts with three different varying proportions of aluminum and aluminum oxide under dry sliding conditions and ambient temperature was investigated. 5, 10, 15, and 20 N loads were used at a sliding velocity of 1.36 m/s for durations of 5 and 10 minutes. The findings revealed that all Nylon6/Al/Al_2O_3 composites exhibited superior wear resistance in comparison to their ABS counterparts. Furthermore, it was reported that the composite materials exhibited lower frictional coefficients and frictional forces when compared to commercially used ABS materials.

Zhong et al. [67] investigated the properties of the short fiber-reinforced composite used in manufacturing and rapid prototyping. ABS was modified through the incorporation of diverse property modifiers, such as short glass fibers, plasticizers, and compatibilizers. The addition of fiber content to composites was limited to a maximum of 40 wt%, with further increments resulting in printing challenges related to nozzle clogging. In addition, it has been reported that composites with higher fiber loadings are difficult to form into continuous filaments for FDM due to loss of toughness. The investigation revealed that the inclusion of glass fibers in ABS filaments led to notable

improvements in strength; however, this was accompanied by a trade-off in terms of reduced flexibility and handleability.

Yadav et. al. [68] conducted a study on the impact of FDM parameters on the tensile strength of various materials, including polyethylene terephthalate glycol (PETG), ABS, and a composite material consisting of 60% ABS and 40% PETG. During the fabrication of composite materials, the initial 60% of the layers are deposited using ABS filament, followed by the subsequent 40% that are deposited with PETG filament, resembling a sandwich model where one material was overlaid upon the termination of the other. The study examined the effects of various process parameters on 3D printing, including extrusion temperature, layer thickness, and material density. The maximum tensile strength is attained in PETG material when utilizing an extrusion temperature of 225°C and a layer height of 0.1 mm, as evidenced by the experimental results. This particular investigation indicated that the tensile strength of the composite material exhibits a notable reduction in comparison to the primary ABS and PETG materials.

Alarifi [69] proposed a new method for simulating the failure of a 3D-printed structure. The study utilized a 3D printer to fabricate the structure using commercial PETG reinforced with carbon fibers (CF). The mechanical properties of the PETG/CF composite materials were evaluated through modeling, and the results were quantitatively correlated with experimental data. The study demonstrated how finite element analysis (FEA) of 3D printing was employed to assess the performance of a helmet chinstrap design under different fabrication conditions, potentially decreasing the time required for structure design and development.

Magri et al. [70] fabricated samples using commercially available PLA and short CF-reinforced PLA composite filaments with a 3D printer. Subsequently, mechanical and thermal analyses were conducted on the PLA and PLA composite samples that were produced under various processing parameters. Although the addition of short fibers leads to certain improvements in mechanical properties, it was also observed that this results in increased porosity in the produced structure, which prevents it from attaining its maximum strength.

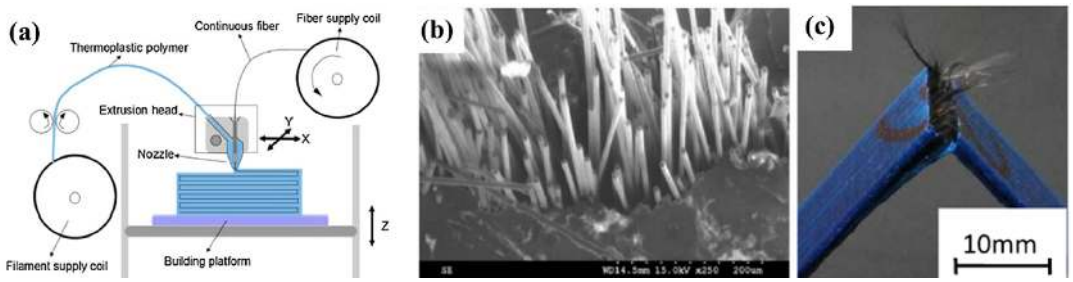

Figure 2.2 a) Schematic illustration of the setup for the 3D printing that can produce composites, b) image of matrix and reinforcement material interfacial adhesion zone, and c) fracture pattern of fractured composites [71]

Xiaoyong et al. [71] studied a 3D printer working with continuous fiber-reinforced thermoplastic composites; the 3D printer and printed composite are shown in Figure 2.2. In this study, continuous carbon fiber was employed as the reinforcement material, while PLA filament was used as the matrix material, and both were concurrently fed into the 3D printer working with the FDM to achieve integrated forming and preparation of composites. The performance and interfaces of the manufactured composites were methodically investigated by analyzing the influence of process parameters on the pressure and temperature in the process. They fabricated composite components to demonstrate the process's feasibility.

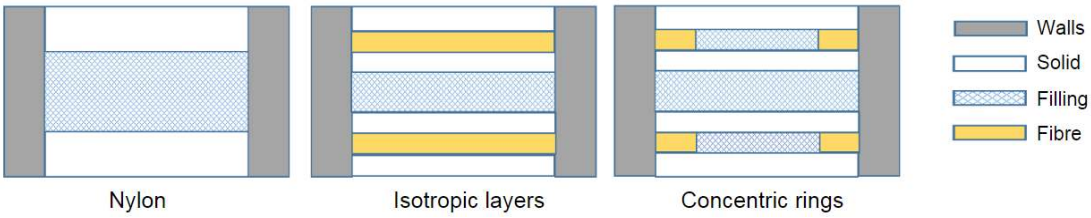

Figure 2.3 Cross-section of the test samples for various configurations of fiber reinforcement

Alberto et al. [72] investigated the tensile and fatigue behaviors of continuous fiber-reinforced polymer composites produced from a nylon matrix with fiberglass, Kevlar, and carbon fibers. Figure 2.3 shows the configuration of 3D-printed samples. The study reports the effects of several printing parameters, including filling rate, fiber orientation, the filling pattern of the nylon matrix, fiber materials, and number of concentric rings used in the printing configuration, on the performance of the fabricated composites. They reported that samples with isotropic carbon fiber layers

had a higher ultimate tensile stress, at 165 MPa. It was observed that specimens with nylon matrix reinforced with carbon fiber showed better fatigue performance. The mechanical characterization of continuous fiber-reinforced thermoplastic composites was systematically investigated, revealing their promising potential as composite materials for engineering applications.

2.2.2 Cross-linked Composites Materials

It is widely recognized in the literature that cross-linking induces an elevation in the viscosity of the polymer melt, enhances tensile strength, and improves resistance to environmental stress cracking, as evidenced by previous studies [73]. Wong et al. [74] investigated the influence of molecular structure on the silane cross-linking process of three distinct types of polyethylene (PE). The study delved into the examination of silane grafting efficiency in different PE types, alongside an investigation of the moisture diffusion rate of the cross-linked polymer.

The study conducted by Khonakdar et al. [75] aimed to examine the impact of cross-linking content on the thermal and mechanical properties of high-density polyethylene (HDPE). This involved determining HDPE's physical and chemical properties, estimating the molecular weights between cross-links, and cross-link density using a novel approach, and investigating their correlation with the associated peroxide content.

Yamoum et al. [76] fabricated cross-linked PLA by mixing commercial PLA with peroxide materials using a twin-screw extruder, and subsequently examined the rheological, thermal, and mechanical properties of the resulting cross-linked material. The study revealed that the addition of peroxide resulted in improved thermal stability of PLA.

Zhang et al. [77] investigated a microcross-linking approach to enhance the melt strength of PLA. In addition, cross-linked PLA (C-PLA) and poly(butylene adipate-co-terephthalate) (PBAT) were blended in a single-screw extruder to improve melt strength and viscosity. Rheological, thermal, and microstructural analyses were conducted, revealing that microcross-linking and the addition of PBAT resulted in the increased viscosity of C-PLA and C-PLA/PBAT blends, leading to improved melt

strength. Furthermore, an enhancement in the crystallinity ratio of PLA material was reported.

Zhu et al. [78] conducted research on cross-linked nanocomposite films fabricated using heat-resistant polyetherimide (PEI) and alumina (Al_2O_3). The nanocomposites were produced with polymerization and solution casting technique. It was stated that cross-linked networks in the samples develop the breakdown strength and suppress dielectric loss. The authors concluded that cross-linked nanocomposites lay a foundation for the application of high-performance polymer dielectric films in high-temperature energy storage.

Bi et al. [79] worked on the fabrication of 3D-printable cross-linked composites with notable attributes such as superior thermal, mechanical, shape memory, and self-healing properties. The thermoreversible cross-linked networks are comprised of covalent and transient cross-links via Diels-Alder reactions, which are formed by the combination of thermoplastic polyurethane and poly(ε-caprolactone). The authors reported the successful fabrication of a 3D-printable polymeric composite with a thermoreversible network, which exhibited integrated shape memory and self-healing functions.

Mietner et al. [80] aimed to develop a bio-based hybrid material consisting of polymer-modified cellulose nanofibers cross-linked with calcium ferrite nanoparticles, with the goal of utilizing it as a gel ink for 3D printing. Composited specimens were characterized by IR, SEM, and TGA. The authors reported the successful development of a 3D-printable cross-linked gel ink suitable for use in 3D pneumatic extrusion printers.

Upon reviewing the literature, numerous studies have considered additive manufacturing techniques to produce composite materials. In some, the reinforcement material was blended with commercially available filaments and subsequently processed through a screw extruder to produce a composite filament [62]–[70]. Thereafter, the composite filament was used to fabricate the final product. Although some studies have shown improvements in the mechanical and physical properties of composites produced via additive manufacturing, others have reported poorer results.

This decrease in mechanical properties is attributed to weak interfacial adhesion strength between the matrix and reinforcement material, as reported in several studies. Moreover, none of these studies produced the composites in situ during the printing process but rather used pre-made commercial composite filaments. Some studies have investigated printers capable of producing composites reinforced with continuous fiber material, which have shown a relatively improved mechanical performance [71], [72]. However, the issue of weak interfacial adhesion persists. Furthermore, the production of complex shapes with fiber reinforcement using this method is currently limited, thereby restricting its potential applications. Despite the longstanding recognition of the process of polymer strengthening through cross-linking [73]–[78], no 3D printer or process capable of applying cross-linking in situ during three-dimensional printing has been identified in the literature to date. While studies utilizing filaments produced with the cross-linking technique using screw extruders do exist, none incorporate the cross-linking process into the 3D printing process itself [79], [80].

2.3 Enhancing the Mechanical Properties of Additively Manufactured Parts: Strengthening Techniques

In the recent literature, there is a growing body of research investigating strategies to enhance the mechanical properties of structures produced through additive manufacturing processes.

2.3.1 Investigation of Process Parameters

Numerous studies have been conducted in the literature aimed at enhancing the mechanical properties of 3D-printed products. Sharma et al. [81] conducted an experimental study on the effect of process parameters, including printing speed, infill percentage, and layer thickness on the mechanical properties of parts fabricated from ABS filament. The results revealed that increasing the infill percentage led to improvements in both the compression and tensile properties of the material.

Rajpurohit et al. [82] worked on mechanical properties, as the tensile strength of PLA fabricated parts depends on layer thickness, raster angle, and raster width. Five different values of the raster angle are selected such as 0, 30, 45, 60, and 90°. The researchers identified that the raster angle is a significant factor in terms of its influence on the strength of the test sample in their study. Also, raster width was identified as

another crucial parameter affecting the mechanical properties of 3D-printed objects. The research findings revealed that enhancing the raster width up to 600 μm led to an increase in the strength, but was observed to decrease on further increment; this was attributed to the formation of voids.

Chacón et al. [83] conducted an investigation on the influence of 3D-printing-process parameters, including build orientation, layer height, and feed rate, on the mechanical behavior of PLA specimens. Their findings revealed that PLA samples with on-edge orientation, low layer height, and high feed rate exhibited superior mechanical performance. Moreover, they observed that an increase in layer thickness and feed rate resulted in reduced ductility of the 3D-printed PLA products.

Mohamed et al. [84] studied the impact of 3D printers working with FDM process parameters on time-dependent mechanical characteristics. A mathematical model was developed to analyze the creep displacement of PC-ABS. The study focused on process parameters including slice build direction, thickness, bead width, raster angle, air gap, and number of shells. The findings indicated that creep displacement reduced as the raster angle decreased, with the optimum raster angle for achieving the highest mechanical performance being 0°.

Samykano et al. [85] investigated the impact of three main process parameters – raster angle, layer height, and infill density – on the mechanical behavior of ABS. Specimens were fabricated using a 3D printer working with FDM using three different raster angles (45°, 55°, and 65°). The findings revealed that the optimal process parameters for FDM printing with ABS were a raster angle of 65°, an infill percentage of 80%, and a layer thickness of 0.5 mm.

Huynh et al. [86] examined the impact of process parameters on the mechanical properties of PLA specimens fabricated via the FDM method. The Taguchi method was employed to generate a design matrix consisting of three process parameters, namely layer height, printing speed, and temperature. The results demonstrated that optimal mechanical performance in 3D-printed specimens was achieved with a layer height of 0.15 mm, printing speed of 48 mm/s, and extrusion temperature of 220°C.

Taylor et al. [87] examined the flexural properties of the polyetherimide samples printed with different build orientations and raster angles. The study involved three build orientations (on edge, flat, and upright) and two raster angles (0°/90° and 45°/-45°). Additionally, a finite element model was developed to simulate the flexural properties of 3D-printed FDM objects. The finite element simulation data suggested that the 3D-printed parts could potentially be suitable for industrial applications.

Motaparti [88] conducted a thesis investigating the impact of build parameters on the mechanical properties of ULTEM 9085 parts. The results from their bending test showed that the yield strength of parts built in the vertical direction was 15-30% higher than that of parts built in the horizontal direction. Furthermore, it was found that for both horizontal and vertical build directions, at angles of 0° and 90° the flexural strength of parts built with a raster angle had a 5-10% higher strength compared to those built with a raster angle of 45°/-45°.

2.3.2 Post-Processing Techniques

Han et al. [89] proposed a novel method involving the use of an infrared laser to heat the interface between layers during the Fused Filament Fabrication (FFF) printing of PEI. The experimental setup for this method is illustrated in Figure 2.4. The findings revealed that the application of this method led to the formation of a stronger bond between the layers, resulting in improved strength of the printed parts.

Singh et al. [90] aimed to enhance the mechanical properties of 3D-printed ABS samples using a heat treatment process. The authors systematically investigated the impact of annealing temperature and holding time on the mechanical properties of the specimens. It was observed that when thermoplastic materials constructed using the FDM technique were subjected to heat treatment above the glass transition temperature, the voids between the filaments were reduced. Subsequently, through statistical analysis of the mechanical test results, the researchers determined that the applied temperature was a more significant parameter than the holding time in terms of influencing the subsequent mechanical properties of the printed ABS specimens.

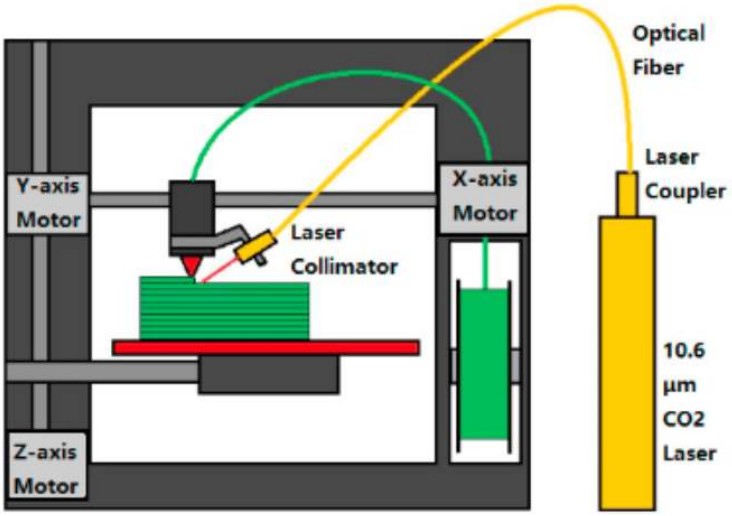

Figure 2.4 Schematic representation of an FFF 3D printer incorporating pre-deposition laser heating [89]

Belter and Dollar [91] published an article entitled "Strengthening of 3D Printed Fused Deposition Manufactured Parts Using the Fill Compositing Technique". In this work, a technique called "fill compositing" was proposed to enhance the strength of thermoplastic parts. The authors discussed the theoretical improvement in bending stiffness and strength that can be achieved through this technique. The process of strengthening a fabricated sample using the fill compositing technique is illustrated in Figure 2. 5. Their findings indicated that by incorporating gaps in the produced parts and filling them with high-strength resins, their overall stiffness and strength could be increased by up to 45% and 25%, respectively.

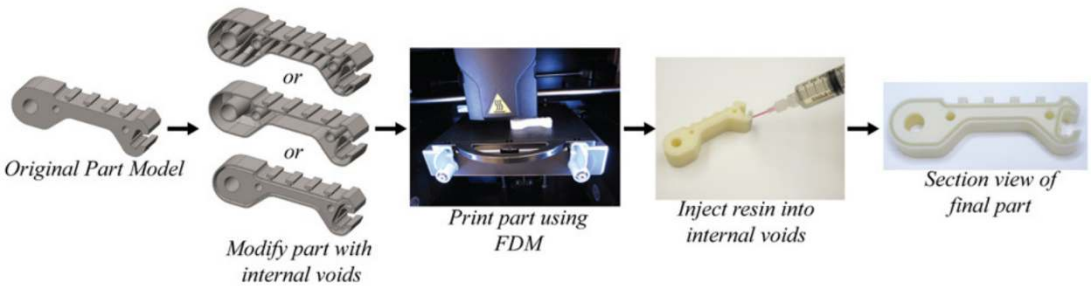

Figure 2. 5 The process of fill compositing with higher-strength resin [91]

Bhandari et al. [92] conducted a study on the interlayer tensile strength of composites fabricated from short carbon fiber-reinforced PETG and PLA with the aim of improving the interlayer tensile strength of these extrusion-based 3D-printed composites. The authors reported that the reinforcement from the short carbon fibers

in the 3D-printed composites resulted in a significant reduction in interlayer tensile strength, with a decrease of 66% observed for an amorphous polymer and 50% for a semi-crystalline polymer when compared to their neat polymer counterparts. Furthermore, they noted that the addition of carbon fibers to the polymers led to an increase in viscosity and a deceleration of the interlayer diffusion process. However, the authors highlighted that the interlayer tensile strength of 3D-printed composites can be restored through the utilization of an annealing process, thus indicating a potential for improving interlayer tensile strength in these composites.

The current industrial additive manufacturing methods are mostly based on PLA or ABS materials, but their strengths are limited. Also, several works into the characterization of PLA and ABS materials fabricated by 3D printing have been reported in the literature [81]–[86]. In order to enhance the strength of 3D-printed products, it is crucial to work on new materials and combine them in FDM. Polyetherimide (PEI/ULTEM 1010), due to its exceptional mechanical strength and heat resistance properties compared to conventional 3D printing materials, has emerged as a promising substitute. The superior properties of PEI/ULTEM 1010, such as high strength, dimensional stability, and excellent chemical resistance, have drawn considerable attention in recent years as a material for advanced applications in various industries. There are several studies in the literature focusing on the optimization of process parameters for the production of PEI materials, as well as for ABS and PLA, but there is a lack of comprehensive investigation regarding the impact of print orientation (raster angle) on the mechanical properties of PEI-based 3D-printed structures [87], [88]. Similar to the previous section, prior research has primarily focused on investigating the impact of annealing on the mechanical properties of commonly used 3D-printing materials, such as ABS and PLA, which exhibit relatively low strengths [90], [92]. However, the effect of annealing on the interfacial adhesion strength of 3D-printed PEI material has not been extensively explored in previous studies. Therefore, to enhance the mechanical properties of 3D-printed products, it is imperative to investigate novel materials and incorporate them into FDM.

2.4 Dual Needle 3D Printer

Ali et al. [93] developed a novel five-nozzle extrusion model to address the limitations of color and material limitations, as well as slow print speeds, in 3D printing working

with FDM. The proposed extrusion model allows for simultaneous printing with five different colors and materials, without the need to stop the printing process for filament switching. The findings of this study suggest that the proposed extrusion model presents a promising technique for achieving multi-color and multi-material 3D printing. The schematic representation of the new extruder design is presented in Figure 2.6.

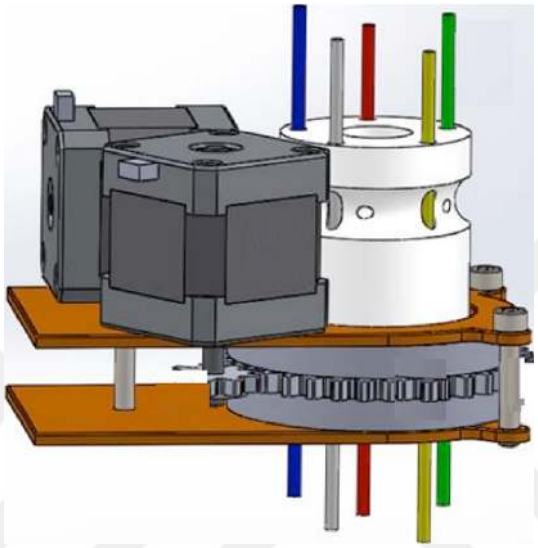

Figure 2.6 Schematic representation of the new extruder design [93]

Yoon et al. [94] propose a three-nozzle extrusion system that can be integrated with a robot to achieve conformal 3D printing with multi-resolution capabilities. The system includes one extruder dedicated to printing support materials, while the other two extruders are utilized to fabricate structural materials with varying resolutions. Specifically, a larger diameter nozzle is used to print the interior regions of the part, while a smaller diameter nozzle is employed to print the surface of the part. It was concluded that this multi-resolution approach not only accelerates the build times but also results in an improved surface finish of the printed parts.

Zhang et al. [95] conducted a study with the objective of producing bilayer samples utilizing dual-nozzle 3D printing techniques, where each nozzle deposits a different polymer. Schematic representation of Bowden extrusion of 3D printer is depicted in the Figure 2.7. Bilayer samples were successfully formulated and fabricated using a dual-nozzle FDM 3D printer. However, the authors observed that the increased

frequency of nozzle switching during the printing process, under otherwise identical printing conditions, adversely affected the printing quality of the tablet.

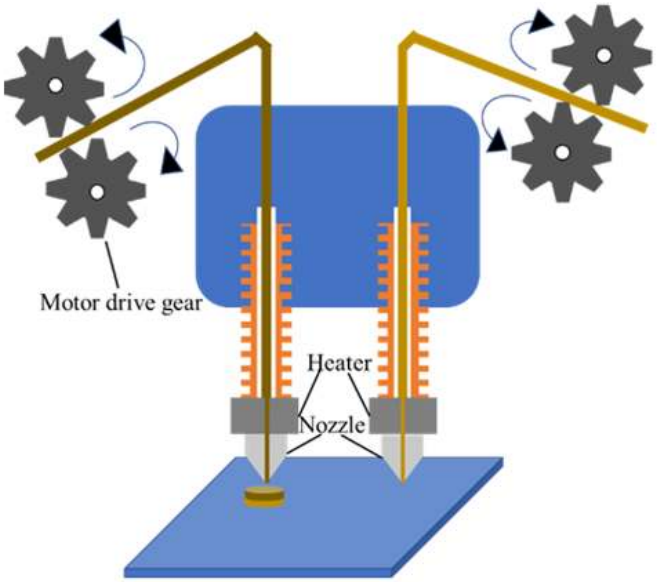

Figure 2.7 Schematic representation of Bowden extrusion of a 3D printer [95]

Mei et al. [96] investigated the mechanical properties of mixed isotropic carbon fiber composites produced using a 3D printer with dual nozzles operating with FDM. One nozzle was used for the deposition of Nylon filament as the matrix material, while the other nozzle was used for deposition the reinforcement fibers at different angles. The scheme of the two dual nozzles is illustrated in Figure 2.8. The study elucidated the impact of fiber deposition angles on the mechanical properties of the composites, providing information on the relationship between fiber orientation and composite performance.

There exist commercially available FDM printers equipped with dual nozzles [97] that also have been utilized for academic studies. However, these academic investigations have focused primarily on either producing [93] or multi-material prints [95], generating support material with a secondary nozzle [94], or implementing continuous carbon fiber reinforcement [96]. The utilization of FDM 3D printers with dual needles for the production of composites has not been extensively investigated in the existing literature. The objective of employing a second nozzle for support material deposition in FDM printing is to prevent material deflection, thereby leading to a smoother surface finish. However, this system does not enhance the mechanical properties of the

3D-printed part. Similarly, the use of a second nozzle in FDM printing for producing multicolored parts is aimed at enhancing the aesthetic appeal of the printed product without influencing its mechanical properties. In contrast, the use of a second nozzle for the deposition of continuous carbon fiber reinforcement material leads to increased mechanical properties of 3D-printed structures. However, this method is limited in its application to complex print geometries.

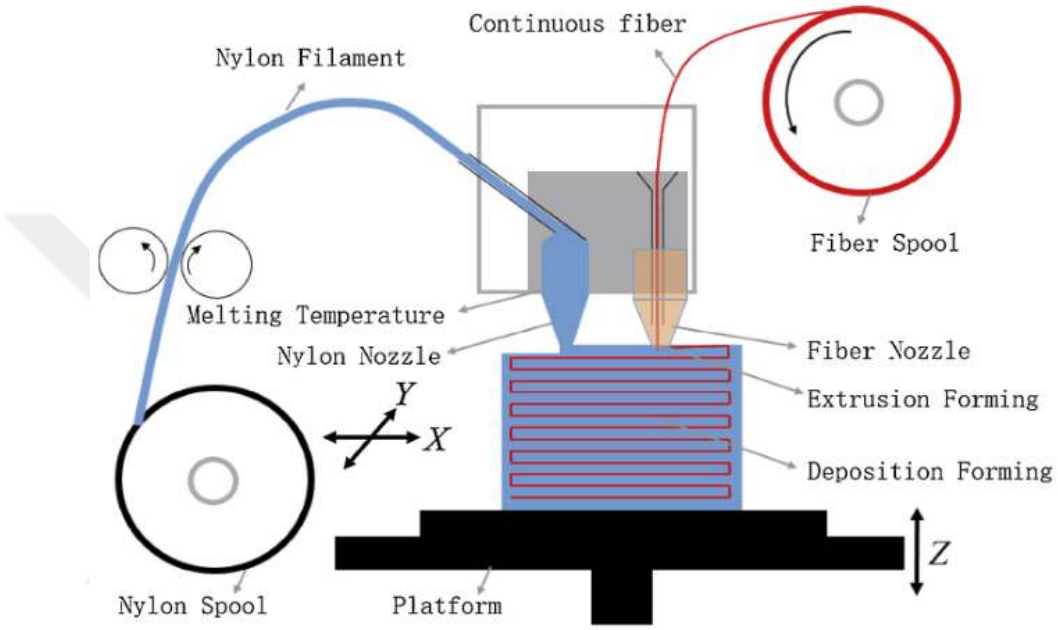

Figure 2.8 The scheme of the two dual nozzles [96]

CHAPTER 3

FUNDAMENTALS OF ADDITIVE MANUFACTURING

3.1 Introduction

This chapter serves as a foundational introduction to the fundamental principles and concepts that underpin additive manufacturing (AM), also commonly known as 3D printing. The historical origins and evolutionary trajectory of AM are also examined, mentioning its development from its nascent stages to its current status.

3.2 What is Additive Manufacturing?

AM is a process of joining materials to create objects from three-dimensional (3D) model data, generally layer by layer, in contrast to subtractive manufacturing techniques (e.g., machining methods) or traditional formative (e.g., injection molding) [46]. The alignment of the different layers defining each section of the 3D model allows the construction of the real part in three dimensions. The foundation of AM technology is dependent on the fact that any object, at least theoretically, can be sliced into layers and reconstructed using consecutive layers, whatever the geometry's degree of complexity [98]. Figure 3.1 represents the working principle of the AM method. This figure underlines the foundation of AM.

AM is the formalized term for what used to be called rapid prototyping and what is widely known as 3D printing; other synonyms include additive processes, additive techniques, additive fabrication, additive layer manufacturing, layer manufacturing, and freeform fabrication. AM is standardized in Germany (VDI 3405) [99], and in the US (ASTM F2792) [46], and the usage of additive manufacturing is widespread across the globe [98]. A schematic representation of the difference between subtractive and additive methods is shown in Figure 3.2.

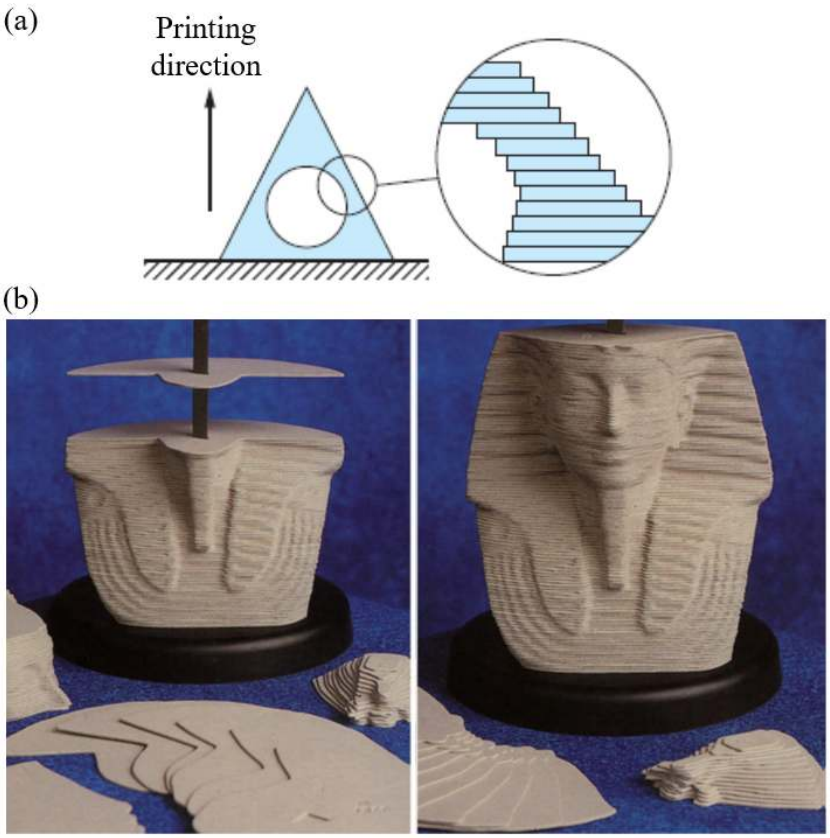

Figure 3.1 Principle of additive manufacturing technology:
(a) schematic representation of a 3D-printed model (left) and the created layer model (right) [100], (b) illustration of additive manufacturing by the successive stacking of layers to obtain a real model in the form of a portrait of a pharaoh (Hasbro-MB puzzle)

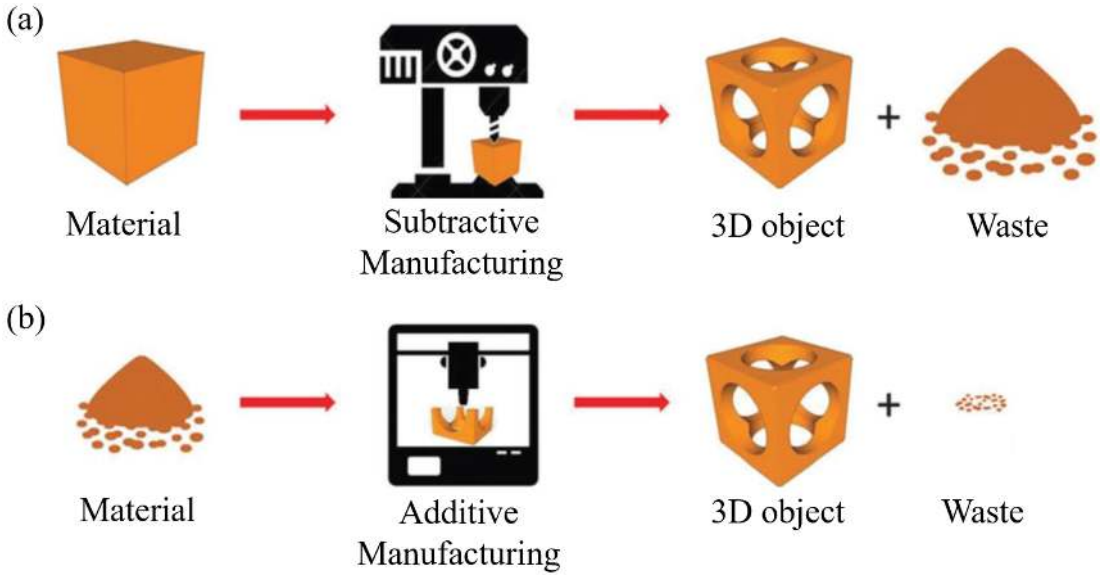

Figure 3.2 Schematic representation of (a) subtractive, and (b) additive manufacturing processes [101]

In subtractive manufacturing, a material block is machined by material-removing machines in accordance with a 3D computer-aided design (CAD) model to construct the final 3D product, along with a significant quantity of waste. AM does not need the cutting tools, other supplementary materials, or coolants used in conventional manufacturing processes. The AM process typically starts with a digital design that is created using CAD software. The CAD file is then sent to a 3D printer machine, which interprets the design and adds material layer by layer to produce the final object. The materials used in AM can include plastics, metals, ceramics, and even food, concrete, and living cells, depending on the type of 3D printer and application. It has the potential to revolutionize manufacturing processes via significantly reducing waste, customization, rapid prototyping, and increased design flexibility. The amount of waste residual after the process is remarkably lower than that from subtractive manufacturing. AM has a wide range of applications across industries, including aerospace, automotive, medical, dental, architecture, food, textile, consumer goods, and others. Its many advantages compared to traditional manufacturing methods have resulted in AM being classified as part of "industry 4.0". Several significant advantages of AM in terms of working principles can be listed as follows:

- Near-net-shape printing
- Easy to learn and use
- Innovations in fabrication using multiple materials
- Reduced raw material wastage
- Reduced fixturing and tooling
- Customization to the individual
- Digital design integration
- Faster cycle times for the first prototype
- Faster cycle times from prototype to production
- Lower start-up costs
- Lower energy and environmental costs
- Low-volume production runs
- Geometric flexibility

Historically, the origins of AM have been considered by many to be based on a development of the 1951-patented "photo-glyph recording" technique [102], which duplicates an item by simultaneously exposing selective layers of a transparent photo emulsion while scanning its cross-sections [103]. However, the development of related technology (computers, controllers, lasers, etc.) only caught up with the concept in the 1980s. Intriguingly, concurrent patent applications were made in the US, France, and Japan in 1984 by Masters in July, Hull in August, and Andre et al., and Murutani, respectively. These patents all discussed the same idea of creating a 3D object in a layer-by-layer manner whilst adding certain materials. Scott Crump patented the fused deposition modeling (FDM) process in 1989 and formed the Stratasys Company. Also, researchers from MIT patented the 3D Printing (3DP) process in 1989 [21]. In the 1990s, a significant turning point was reached in AM technology, and various AM techniques were commercialized. These methods are known as solid ground curing (SGC), laminated object manufacturing (LOM), and FDM [59], [104], [105]. In addition, 3D printers based on direct metal laser sintering (DMLS) technology were developed in 1994 [106]–[108]. Another essential trend that is affecting the growth of AM technology is the end of many of the basic patents for AM processes. Since the initial FDM patents expired in the early 2010s, there has been a surge in the number of material extrusion machines and systems. The development of AM has significantly accelerated over the last twenty years.

3.3 The Generic Additive Manufacturing Process

AM includes several stages that translate virtual CAD files into 3D-printed products. In its simplest form, the AM workflow consists of the following: (1) product design (conceptualization, computer-aided design (CAD)), (2) surface geometry transformation, i.e., standard tessellation language (STL), (3) exporting the files to the 3D printing machine standards, (4) slicing or path planning (print preferences, materials characteristics, geometric consideration, process parameters to generate a machine-executable g-Code and first layer), (5) printing/build (typically layer by layer), (6) removal and cleanup, (7) post-processing (e.g., ultraviolet (UV)-curing or thermal-curing), and (8) application and quality control.

AM techniques are each based on different working principles. However, as mentioned above, the sequence of steps is typically suitable for all AM technologies. There could

be differences depending on which technology is used and the part's design, while specific steps can be related to some 3D printing machines but may be trivial for others. The eight main stages of the AM techniques follow similar processes for each method, at least to some extent [109]. The stages are presented in Figure 3. 3 and can be detailed as follows:

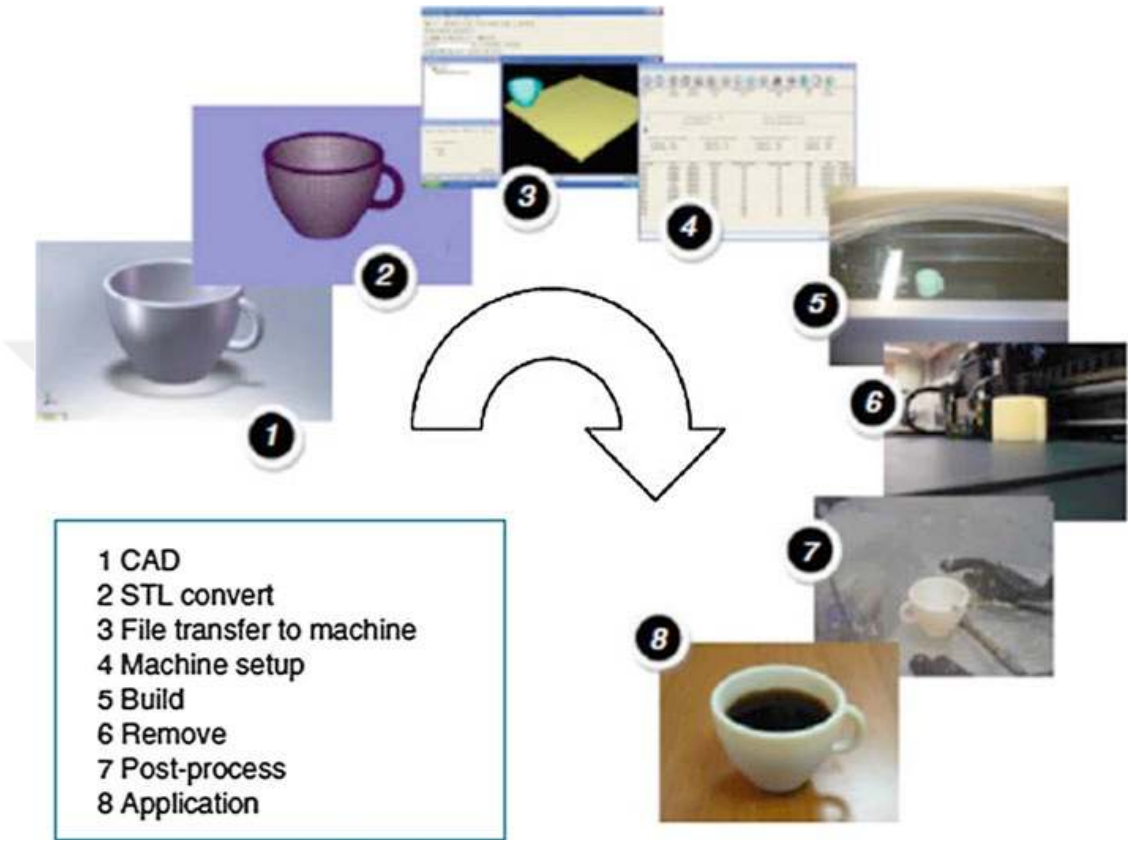

Figure 3. 3 AM workflow (the eight stages of the AM process) [21]

Design, Conceptualization, and CAD

The first step in developing the parts and products to be created by AM must start with a CAD model that fully describes the external geometry. Therefore, CAD processes are particularly closely related to the use of AM techniques. There are two global design methods: the virtual model using CAD software, and reverse engineering tools (e.g., optical and laser scanning). Virtual model CAD files can be obtained with the use of almost any professional solid modeling software, but the output must be a 3D solid or surface representation. The virtual model is obtained via a 3D scan of a real object. The principle is to reconstitute the covering of the real object as a virtual model in the form of a set of elementary facets defined by points (Figure 3.4).

Dimension of CAD Elements	Element	Type of CAD Model
0D	Point 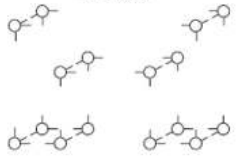	Corner Model
1D	Line 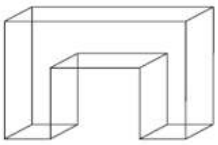	Edge Model
2D	Surface 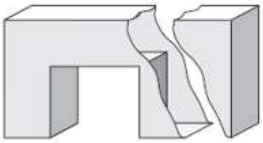	Surface Model
3D	Solid / Volume 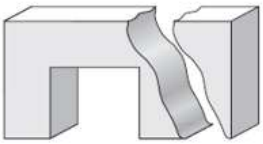	Solid or Volume Model

Figure 3.4 CAD elements and model types [98]

The point-based corner model is not usable for AM operations. It serves as an intermediary model, for instance, in the automated conversion of grid data or 2D CAD models into 3D CAD models.

Conversion to STL

The standard format for defining the surface geometry of an object design is called standard tessellation language (STL), and is used to transmit the design to an AM machine. All further design details (such as color, material, etc.) that are not directly related to the geometry are eliminated. The approximation is made by creating small triangles using a cartesian coordinate system, namely their vertices and the normal vector that points out the outer surfaces (Figure 3.5) [109]. To ensure that pieces are printed at the highest quality feasible, the triangles' dimensions must be smaller than the machine's minimum resolution.

Figure 3.5 CAD model and converted STL model

The STL file format is now widely adopted by AM machines, and almost all CAD systems can produce files in this format. This file serves as the foundation for the computation of the slices and describes the exterior closed surfaces of the original CAD model.

Transfer to AM Machine and STL File Manipulation

The STL file describing the part must be transferred to the AM machine. Before starting the construction of the part, the virtual model must be prepared using computer-aided manufacturing (CAM) software, that is, the one provided by the company marketing the AM machine, by importing its source file in STL format. There may be several actions that need to be taken prior to building the part. Therefore, it is necessary to attribute characteristics to the virtual model allowing for the concrete realization of the part, such as:

- The orientation of the virtual model according to the build platform
- The addition of manufacturing supports connecting the part to the platform. The supports play an important role because they prevent the part from deforming or coming off, but also allow it to be detached more easily from the platform subsequent to manufacture

Multiple parts can be uploaded at this stage and so be printed together. These parts may be multiples of the same part (thus requiring a copy function) or completely different STL files. STL files can easily be linearly scaled.

Machine Setup

The AM machine must be properly set up prior to the build process. Such settings would relate to build parameters like slicing the model into thin layers, defining print parameters such as layer thickness, material type, print temperature, and print speed, and generating machine-specific instructions for the printer. Apart from configuring software parameters, physical preparation of the machine is also necessary prior to starting a build. The operator needs to verify that there is sufficient build material loaded in the machine to complete the printing process. Once the build parameters of AM machine are selected and the build materials are loaded, the 3D model is ready for printing.

Build

While leveraging computer assistance, the initial stages of the AM process involve semi-automated tasks that may necessitate substantial manual control, interaction, and decision making. Once these preparatory steps are complete, the process transitions to the computer-controlled building phase. The 3D printer begins the AM process, following the instructions from the machine setup (pre-processing) step. The process of fabricating the part is largely automated, and the machine can largely operate without supervision. Layer by layer, the material is solidified, cured, or deposited, depending on the specific technology, to build the final object. The material may be selectively deposited or solidified using lasers, heat, or other forms of energy sources, or by using a binding agent or adhesive to join the material layers together. As long as no errors like running out of material, power or software glitches, etc., occur during the construction, AM machines will repeat the layering process until production is complete.

Removal and Cleanup

Following the completion of the build process of the 3D part, removal and cleanup steps are typically required to extract the printed object from the build platform and prepare it for use or further processing. Some AM methods require the use of secondary support materials, which are materials in addition to those used to manufacture the component itself. Even though various methods have been developed to make supports that are simple to remove, this stage typically requires a large amount of personal labor on the part of the user. Depending on the AM technology employed,

the printed components are separated from the build platform or support structures. The 3D-printed part may have excess material or residual debris on its surface, such as filament strands, powder, or support remnants, which need to be cleaned. It is essential to note that the removal and cleanup procedure can vary according to the AM technology, the material used, and the requirements of the printed object.

Post-processing

Post-processing refers to the steps of finishing the printed parts for application purposes. Depending on the intended properties of the printed component, additional post-processing steps may be required. This may involve heat treatment, surface treatment, or some other process to refine the surface finish, enhance the mechanical properties, or add functional features to the 3D-printed part. Heat treatments are used to reduce residual stresses of metal parts. Surface treatments, especially grinding and polishing, are applied to reduce surface roughness. This is usually due to the staircase effect during manufacture along the Z axis. The quality of the printed product must be carefully handled, and the post-processing must be performed correctly if it is to retain its functionality and performance.

Application

The printed part may be subjected to inspection and quality control processes to ensure it meets desired specifications, tolerances, and performance criteria. Following post-processing, the finished 3D-printed parts are ready for use or further integration into some final product, depending on the specific application. However, products may need additional treatment before these printed parts are acceptable for use. For instance, products may need painting and priming to ensure a suitable surface quality and texture. Products may also need to assembled together with other electronic or mechanical components to form a final model or product.

3.4 Classification of AM Processes

AM methods contain ever-expanding material classes, primarily polymers [110], ceramics [111], and metals [112].

Table 3.1 An overview of frequently used classification schemes for the AM process [113]

AM category	Example technologies	Common materials
 Material extrusion	Fused filament fabrication (FFF) or Fused deposition modeling (FDM) Direct ink writing (DIW) or robocasting Embedded 3D printing (e-3D)	Thermoplastics Composites
 Powder bed fusion	Selective laser melting (SLM) Direct metal laser sintering (DMLS) Selective laser sintering (SLS) Electron beam melting (EBM)	Metal Ceramic Plastic
 Vat photo-polymerization	Stereolithography (SLA) or (SL) Digital light processing (DLP) Continuous digital light processing (CDLP) Selective laser printing (SLP) Projection micro stereo-lithography (PμSL) Holographic lithography (HL)	Thermoset plastic
 Material jetting	Inkjet printing (IJP) Three-dimensional printing (3DP) Multijet modelling (MJM) Drop on demand (DOD)	Plastic Metal Wax
 Binder jetting	Binder jetting (BJ)	Gypsum Sand Metal Plastic
 Direct energy deposition	Laser-engineered net shaping (LENS) Electron beam additive manufacturing (EBAM)	Metal

The literature includes a number of different representations concerning the systematics of AM processes. It is essential to remember that the field of AM is rapidly developing, and that new techniques and technologies could easily emerge in the future, resulting in the classification or reclassification of AM processes. Table 3.1

provides an overview of common AM technologies and materials. Below, some frequent classification schemes for AM technologies are given [46]:

3.4.1 Material Extrusion

In the material extrusion technique (MEX), materials in the form of pellets or filaments are melted and extruded through a nozzle to create layers that solidify to form the final object. To build a section of the part, the extruder nozzle or the build platform moves along the X- and Y-axes. To build the next section, either the build platform moves down, or the extrusion nozzle moves up along the Z-axis. Fused Filament Fabrication (FFF) or Fused Deposition Modeling (FDM), and Direct Pellet Extrusion (DPE) are examples of material extrusion AM processes (Figure 3. 6).

FDM is the acronym for Fused Deposition Modeling, which is a popular additive manufacturing technique used to create three-dimensional objects in a layer-by-layer manner. In FDM, a thermoplastic filament is fed into a heated nozzle, where it melts and is extruded onto a build platform. The nozzle moves along a predetermined path, depositing the melted material in a pattern that forms the desired object. As each layer solidifies, either the build platform moves down or the nozzle moves up to allow deposition of the subsequent layer. FDM is known for its versatility, cost-effectiveness, and ability to produce functional prototypes, complex geometries, and end-use parts [114]. FDM stands as a prevalent technique within the realm of additive manufacturing for the production of thermoplastic parts. Stratasys Inc. pioneered the commercial release of this technology in 1991 [115], [116]. The utilization of FDM is experiencing a notable surge in popularity across various domains including everyday life, academia, and industry. This stems from the advancements in production methodologies that enable the straightforward manufacturing of components with intricate geometries, which may be unattainable or time-consuming to produce using alternative methods [117], [118]. This methodology facilitates the fabrication of functional and operational components, as well as the production of prototypes, employing biocompatible materials with robust mechanical properties [119]–[121].

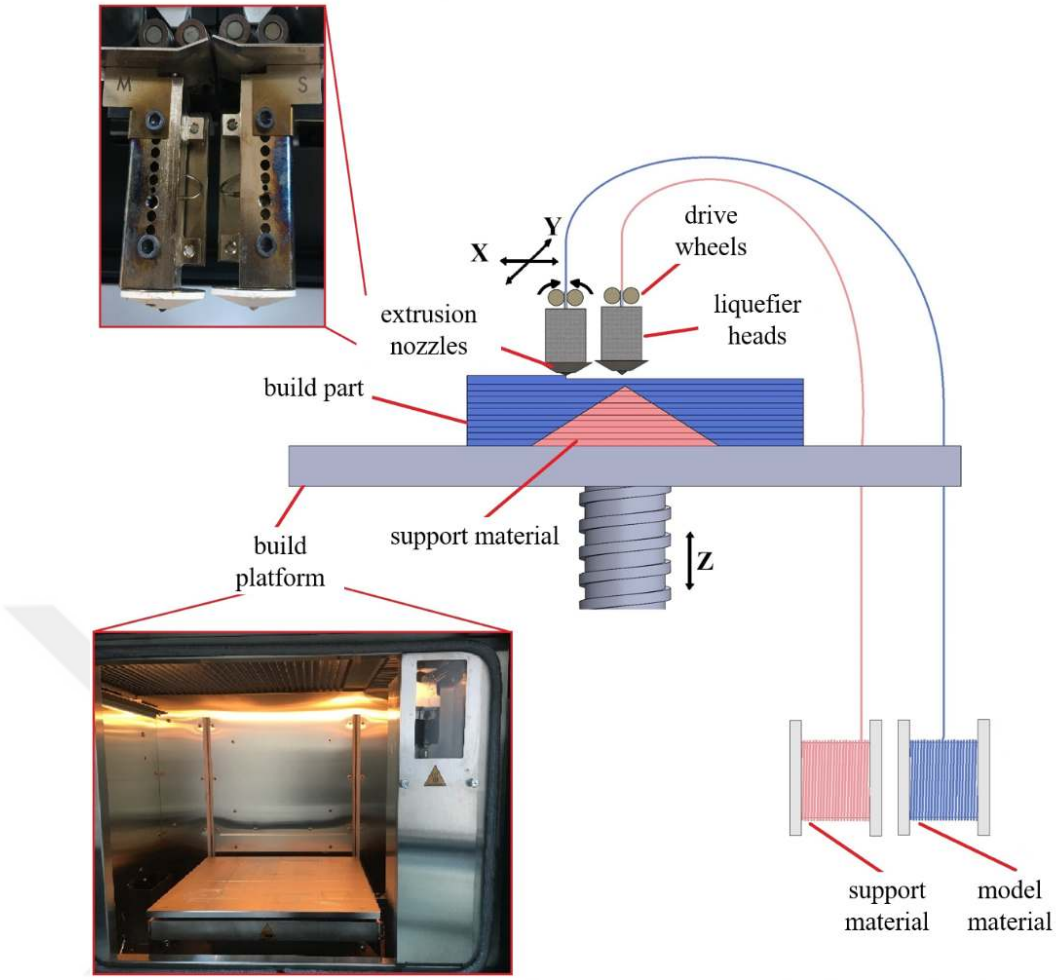

Figure 3. 6 Schematic diagram of material extrusion processes

- Thermoplastic polymer-based filament extrusion processes: Thermoplastic polymers are polymers that deform irreversibly when they undergo heating. Heating this type of polymer, therefore, makes it possible to soften it to various degrees of viscosity depending on the heating temperature. When it is cooled, it solidifies. The polymer filaments are wound around a spool. The most commonly used thermoplastic polymers are polymers based on acrylonitrile butadiene styrenes (ABS) and polylactic acid (PLA).
- Extrusion processes for gels, or viscous liquids made of various materials (composites, food, concrete, clays, etc.): These materials are deposited by extrusion via a piston system, often without heating.

Extrusion processes are the most frequently used in AM for the following reasons:

- Their low cost, resulting from the materials used (thermoplastic polymers) or the machines used.

- Their ease of use. The machines can be of very different sizes: they can be simply put on a desk to manufacture small parts, up to the use of machines allowing the manufacture of houses via extrusion of concrete.

3.4.2 Powder Bed Fusion

In this technique, a layer of powder material is spread over a build platform, and a heat source, such as an electron beam or a laser, selectively melts the powder to form the object layer by layer. Powder bed fusion (PBF) processes are a type of additive manufacturing, commonly known as 3D printing, where a part is built in a layer-by-layer manner using a powdered material. A layer of powder is spread over the previous layer by means of a spreading system (generally composed of a roller and a scraper). The newly spread layer is selectively melted by the action of an energy source to form a new section of the object.

PBF processes are widely used in various industries, including aerospace, automotive, medical, and tooling, for the production of functional prototypes, end-use parts, and complex geometries that may be difficult or impossible to achieve via traditional manufacturing methods. PBF processes offer advantages such as design freedom, reduced material waste, and the ability to create complex internal structures, making them a popular choice for advanced manufacturing applications. There are several different PBF technologies, each with its own specific characteristics and applications. Some of the commonly used PBF processes include:

3.4.2.1 Selective Laser Sintering

In selective laser sintering (SLS), a high-powered laser is used to selectively heat and fuse powdered material, typically polymers, to create a solid part. The laser scans the powder bed, melting the particles together to form a layer; a new layer of powder is then spread on top, and the process is repeated until the part is fully built (Figure 3.7). The use of thermoplastic polymer powders has two practical advantages: the first is that it only takes low laser powers to soften the powder; the second is that it is not necessary to have any form of support connecting the manufacturing platform to the part, as the unsintered powder serves directly as such.

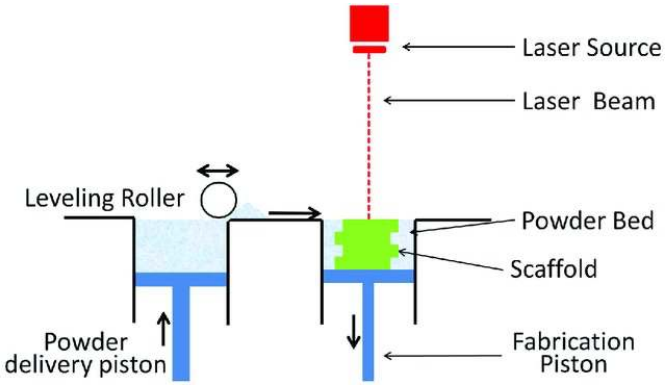

Figure 3.7 Schematic diagram of the thermoplastic polymer powder bed fusion process by laser beam [122]

3.4.2.2 Selective Laser Melting

Selective Laser Melting (SLM) is similar to SLS, but instead of sintering, the laser entirely melts the powdered material to produce an object. In the SLM process, a thin layer of metal powder is spread onto a build platform, and a powerful laser is used to selectively melt and fuse the powder particles together according to a pre-design model. The laser scans the powder-covered build platform, melting the particles to create a solidified and hardened layer, after which a new layer of powder is spread on top and the process repeated until the part is completely constructed, layer by layer (Figure 3.8). This method is commonly applied to metals and alloys, and it allows for the production of complex and highly detailed pieces with superior mechanical qualities.

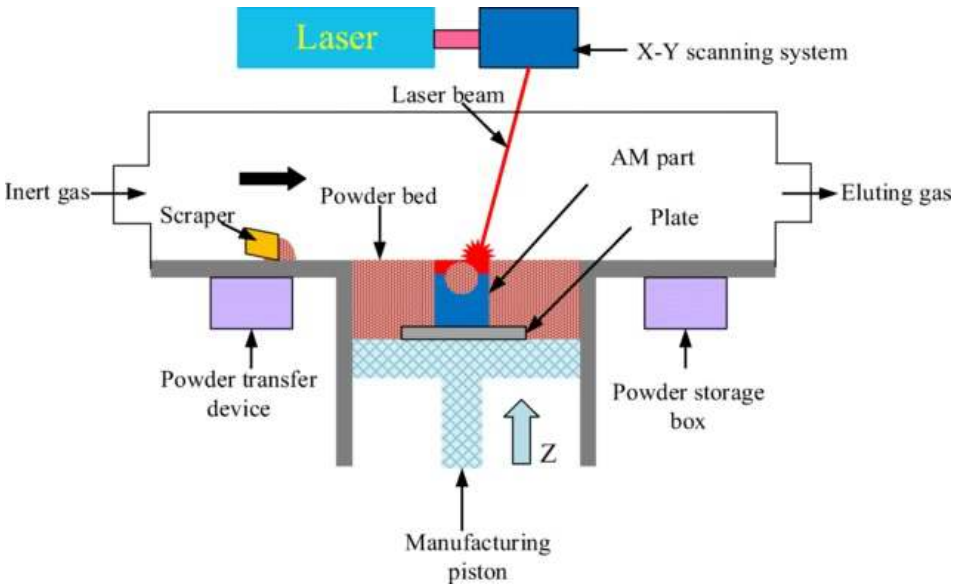

Figure 3.8 Schematic representation of the selective laser melting system [123]

The SLM's key feature is the complete melting and fusion of the powder particles, which produces extremely dense and structurally sound metal parts with good mechanical properties. SLM is appropriate for a variety of applications in industries including aerospace, automotive, and medical, amongst others, because it can produce intricate internal structures, complex geometric shapes, and parts with fine detail.

3.4.2.3 Electron Beam Melting

Electron Beam Melting (EBM) is similar to SLM in that it uses a powder bed and layer-by-layer approach, but instead of a laser it uses an electron beam to melt the powdered material. In the EBM technique, a thin layer of metal powder is applied to a build platform, and an electron beam is utilized to selectively melt and fuse the powder particles together according to a pre-design model (Figure 3. 9). The electron beam scans the powder-covered build platform, melting the particles to create a solidified layer, after which a new layer of powder is spread on top and the process repeated until the object is completed. EBM is frequently used for metals and is known for its capacity to create components with good material density and high mechanical properties.

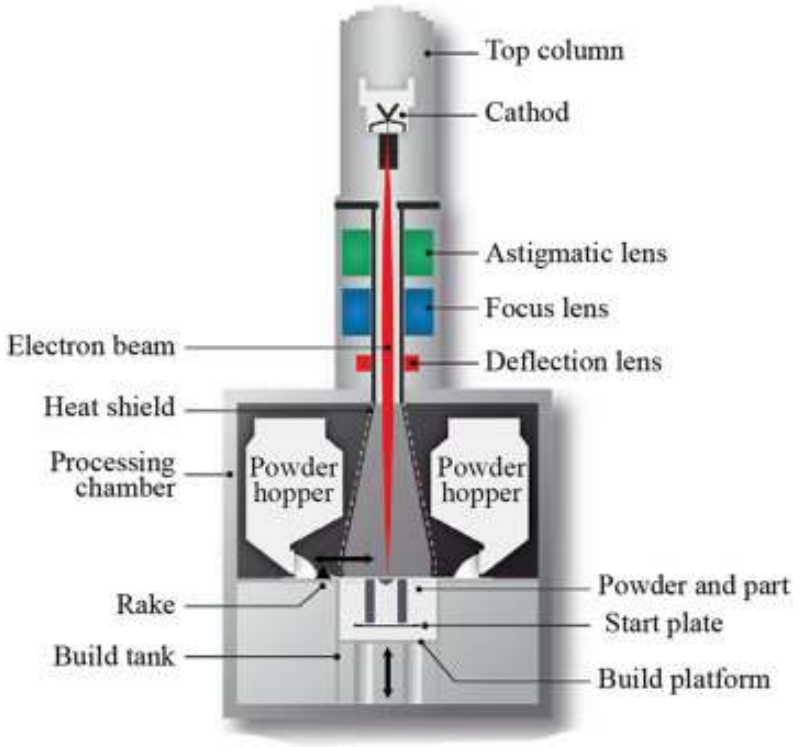

Figure 3. 9 Schematic representation of the electron beam melting system [124]

EBM also offers distinct advantages over other PBF techniques, such as the ability to process materials with high thermal conductivity and high melting points, as the electron beam can supply higher energies than a laser. However, EBM also has its own set of process parameters and considerations, including the need for vacuum, electron beam management, and material characteristics, which need to be carefully controlled to achieve optimal product quality. EBM is faster and generates less thermomechanical stress than laser beam melting. This, therefore, makes it possible to reduce the number of support structures. However, this technique also has drawbacks, such as only conductive materials can be used in this process, which limits the application to metals.

3.4.2.4 Direct Metal Laser Sintering

Direct Metal Laser Sintering (DMLS) is a specific variation of SLM that is used for metals. The process itself is trademarked by EOS GmbH, a leading manufacturer of 3D printers. The term DMLS is often used interchangeably with SLM, but the former specifically refers to processes using EOS machines.

3.4.3 Vat Photopolymerization

In this method, a liquid resin is selectively cured via a light source, such as a UV laser, to solidify and, layer by layer, form the part. Vat photopolymerization is frequently used in applications like prototyping, dentistry, medical equipment, jewelry, and other specialized industries where fine details and high precision are required to produce high-resolution, precise parts with smooth surface finishes. There are different types of vat photopolymerization technologies. Some of the more commonly used of these technologies include:

3.4.3.1 Stereolithography

Stereolithography (SLA) is one of the earliest and most widely used vat photopolymerization methods. It uses a laser beam to selectively cure a liquid resin layer by layer. A laser scans the liquid resin's surface, curing it in the desired areas according to the shape of the 3D object (Figure 3. 10).

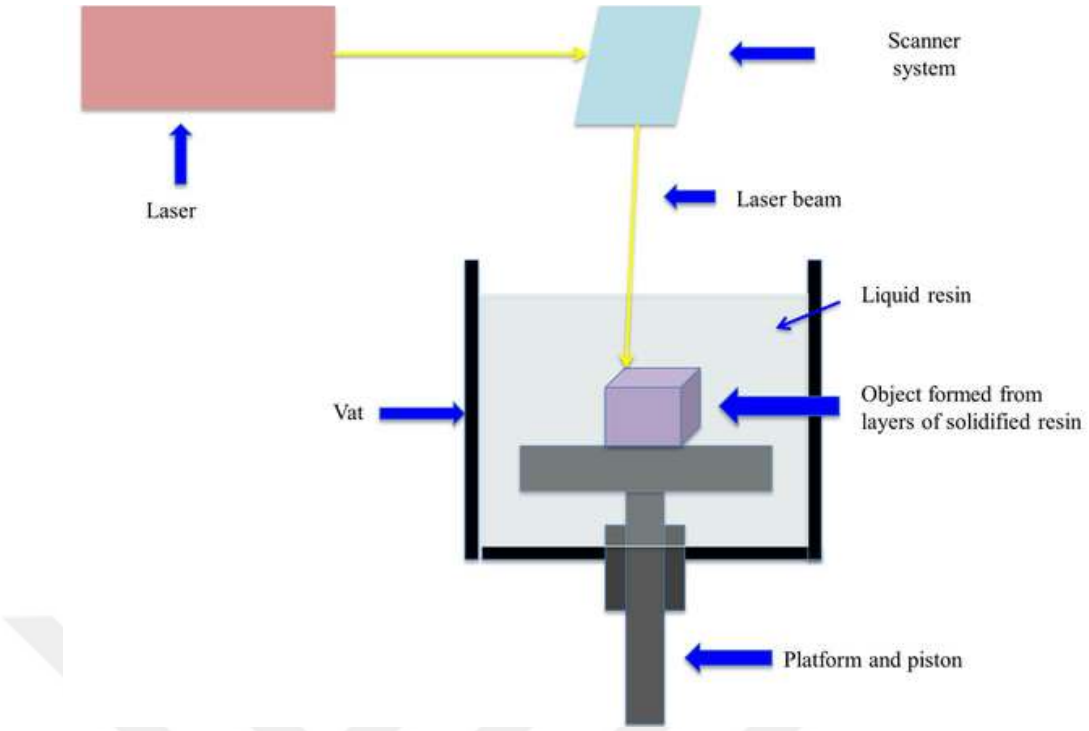

Figure 3. 10 Schematic representation of the stereolithography system [125]

The platform is then lowered, and a new layer of liquid resin is spread on top of the building platform, and the process is repeated until the entire part is completely fabricated. The SLA method is known for its superior surface quality, high precision, and the capacity to create fine features. The basic SLA process involves the following steps:

- Preparation: A liquid photopolymer resin, which is typically a liquid polymer that is light sensitive and can be cured or solidified when exposed to the appropriate wavelength of light, is placed in a vat or tank. The vat is placed on a build bed, and the bed is positioned at the initial layer height.
- Layering: A platform is lowered into the vat, and a thin layer of liquid resin is spread across the top surface of the platform. The layer thickness can generally range from a few microns to tens of microns, depending on the specific SLA machine and application needs.
- Curing: The liquid resin is then selectively exposed to the appropriate wavelength of light using a laser beam, curing or hardening the resin at the desired locations in accordance with the structure of the 3D model. The laser traces the surface of the liquid resin, tracing the cross-sectional form of the object onto the liquid resin, and solidifying it layer by layer.

- Layer by layer building: Once the first layer is cured, the platform is lowered by the layer thickness amount, and a new layer of liquid resin is spread across the solidified layer. The laser then scans and cures the resin in the desired region of the new layer, building the object layer by layer until the full 3D model is finished.
- Post-processing: Following the completion of the printing process, the part is removed from the liquid resin, and any extra resin is cleaned off. To finish the curing process and attain the part's final qualities, it may then be washed and further cured.

3.4.3.2 Digital Light Processing

Digital Light Processing (DLP) is another vat photopolymerization method that uses a digital micromirror device to project UV light onto a liquid resin, curing it layer by layer to form a 3D part. This technique is similar to SLA but uses a different projection method and light source. DLP is preferred for a broad range of applications, including prototyping, dentistry, jewelry, and consumer products thanks to its good surface finishes, high print speeds, and high resolution. However, this method may require post-processing for optimal results. It may also have a slightly lower resolution compared to SLA due to the pixel size of the digital light projector. The difference between DLP and SLA is illustrated in the Figure 3.11.

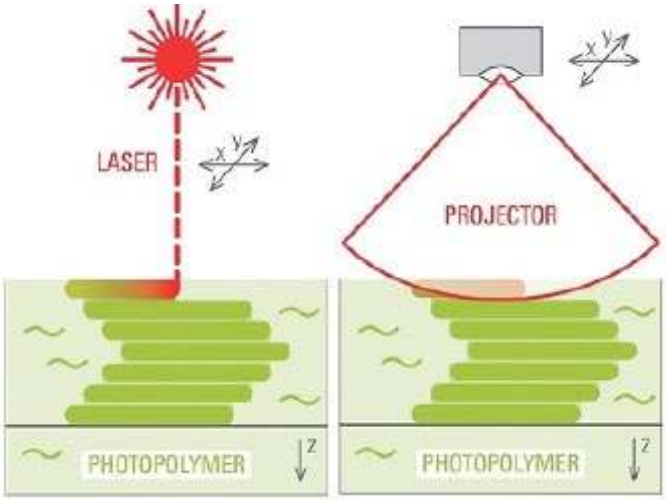

Figure 3.11 Schematic representation of the a) stereolithography, and b) digital light processing systems [126]

3.4.4 Material Jetting

Material jetting is an AM technique that involves selectively depositing or jetting semi-liquid or liquid materials, commonly polymers, onto a build platform to fabricate 3D models layer by layer. The material is deposited in droplets, which are then solidified or cured using various methods such as chemical reactions, heat, or UV light.

Material jetting is similar to inkjet printing, where droplets of ink are carefully deposited onto a substrate to create an image. However, in material jetting, the deposited material is typically a photopolymer resin that can be cured to produce a 3D model. One of the main advantages of the material jetting process is its ability to create highly complex and detailed models with fine detail, good resolution, and smooth surface textures. There are several different methods of material jetting in AM, each with its own specific approach and advantages. Some of the commonly used material jetting methods include:

3.4.4.1 MultiJet Modeling

MultiJet Modeling (MJM) is an AM technology that uses inkjet printheads to jet thin layers of photopolymer material onto a building bed, which is then cured with UV light to produce a 3D model layer by layer. In MJM, the inkjet printheads deposit small droplets of photopolymer material onto the build platform based on a CAD file, and a UV light source selectively cures the material, forming it into the planned geometry. The build platform is then lowered, and a new layer of material is jetted on top, and the process repeats until the component is finished. The working principle of MJM is presented in Figure 3. 12.

MJM provides a variety of material options, including flexible, rigid, and biocompatible materials, making it appropriate for a variety of applications such as prototyping, product development, and producing functional parts. MJM is widely used in industries such as aerospace, healthcare, automotive, and consumer goods, amongst others, due to its ability to manufacture components with fine detail and high precision. However, like other AM technologies, MJM also has its limitations, including the need for post-processing to remove support structures and a comparatively higher price compared to other 3D printing techniques.

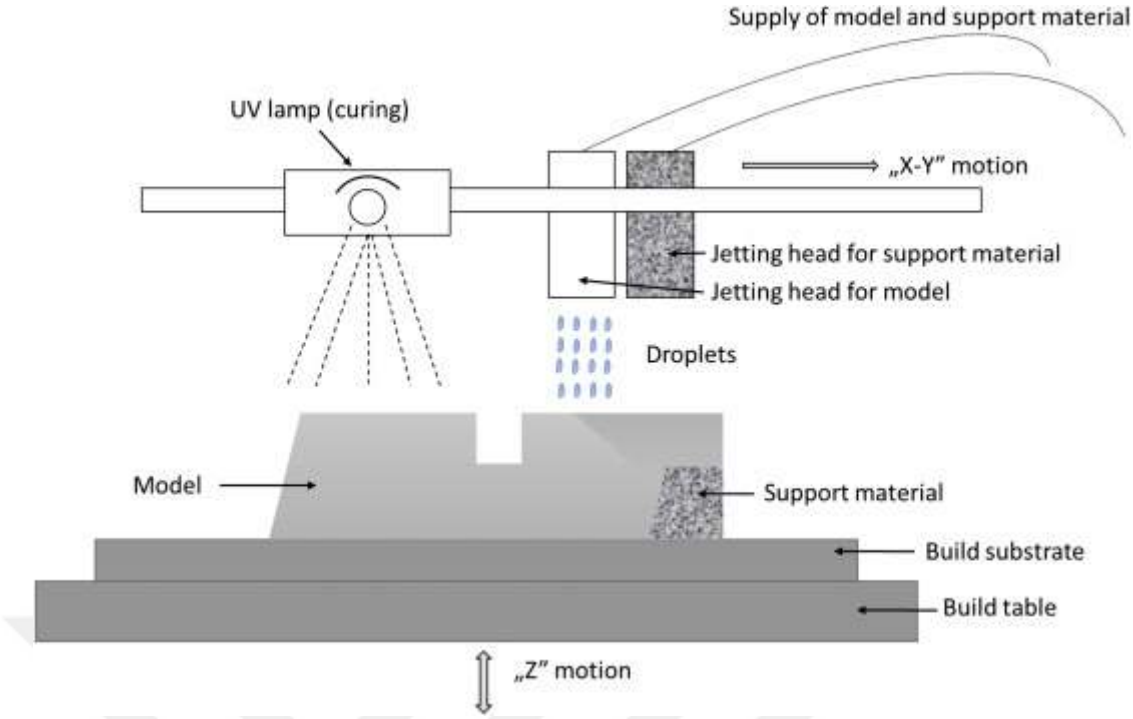

Figure 3. 12 The principle of Multi Jet Modeling [127]

3.4.5 Binder Jetting

Binder Jetting (BJ) is a form of AM or 3D printing process that involves depositing a binder selectively onto a powder bed in order to produce a 3D model layer by layer. The process typically begins with a thin layer of powder spread uniformly on the build platform. A print head then moves across the powder bed, depositing a liquid binder at specific regions in accordance with the CAD data. The binder solidifies the powder particles, bonding them together to form a solid layer. The build platform is then lowered by a defined layer thickness, and the procedure is repeated until the model is finished. The working principle of BJ is presented in Figure 3. 13.

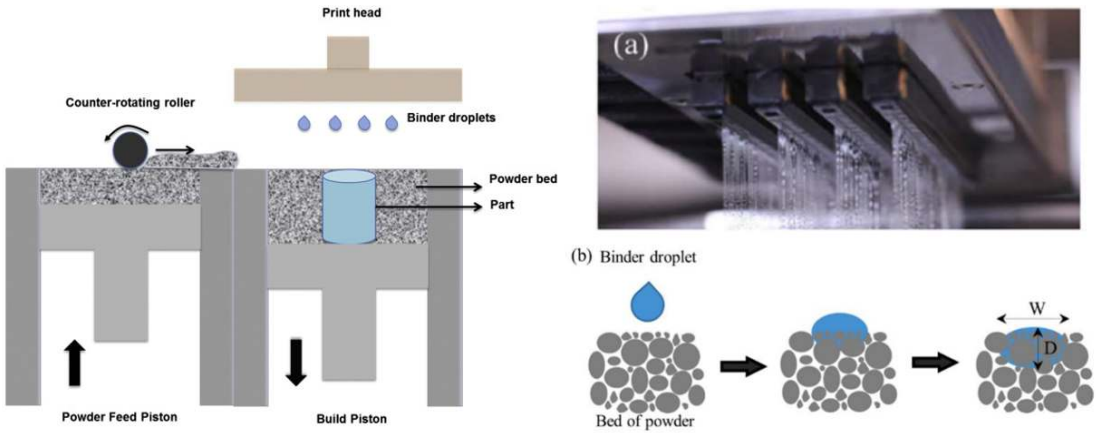

Figure 3. 13 Schematic of binder jet 3D printing process [128], [129]

BJ contains several advantages, including the capacity to create complex shapes, multi-material parts, and large-scale models. It is also compatible with different materials, including polymers, metals, ceramics, and composites, making it appropriate for a variety of applications in industries such as medical, automotive, aerospace, and consumer products.

3.4.6 Comparisons Between Additive Manufacturing Processes

The comparisons between the different AM processes are presented in Table 3. 2. The surface texture and resolution of parts printed by AM technologies can vary significantly. Technologies like DLP, and SLA, and those which use liquid resins and UV curing, can offer high resolution with smooth surface finishes, making them suitable for applications that require intricate detail or fine features. Powder-based technologies like SLS and EBM may have relatively rougher surface textures due to the nature of the powdered materials, while FDM and material jetting processes can have limitations in terms of surface texture and resolution.

Table 3. 2 An overview of common AM process technologies' general strengths and weaknesses [130], [131]

		AM technologies				
		Material extrusion (FDM)	Powder bed fusion (SLS)	Vat photo-polymerization (SLA)	Material jetting (MJM)	Binder jetting (BJ)
Specifications	Printer price	low	high	low	high	high
	Material price	low	high	high	high	high
	Ease of use	very easy	moderate	moderate	easy	moderate
	Porosity	high	low	low	low	high
	Prints resolution	low	moderate	high	moderate	high
	Surface finish	poor	moderate	good	good	good
	Products strength	moderate	very strong	weak	weak	strong
	Generally used by	home users prototyping	advance industries	prototyping	advance industries	advance industries

The cost of AM processes can vary depending on a number of parameters, such as the equipment, materials, and post-processing requirements. In general, processes like FDM and material jetting are considered more cost-effective compared to processes such as DLP and SLA, which may need specialized equipment and materials that are only available for them. Metal-based processes like EBM, DMLS, SLS, and binder jetting can be more expensive due to the expense of metal powders and the requirement for electron beams or high-energy lasers.

CHAPTER 4

MATERIAL AND METHOD

4.1 Introduction

This chapter provides a comprehensive account of the materials, machines, and techniques employed in the production of the research results. Beginning with a detailed overview of the materials' backgrounds and manufacturing methods, this chapter proceeds to outline the methods used for the preparation of the samples and the characterization tests. By detailing the research methodology and providing a transparent account of the materials and techniques used, this chapter aims to facilitate the replication and evaluation of the study's findings.

4.2 Materials

The present study utilized several thermoplastic filament materials, including polylactic acid (PLA), acrylonitrile butadiene styrene (ABS), polycarbonate (PC), thermoplastic polyurethane (TPU), and polyetherimide (PEI). Furthermore, benzoyl peroxide (BPO) and polyvinyl acetate (PVA) have been employed as reinforcement materials. The selection of these materials was based on their physical and chemical properties, which made them suitable for the intended applications in the study. By using these materials, the study aimed to explore their mechanical, thermal, and morphological characteristics, and to investigate their potential for use in various industrial applications.

4.2.1 Polylactic Acid (PLA)

The current thesis utilized Porima PLA® filaments, a product developed and manufactured by Porima Polymer Technologies Co., as the primary material for 3D printing.

Porima PLA® filaments belong to the category of polylactic acid (PLA) filaments and are designed specifically for use in 3D printing applications. PLA was used as a matrix material in the production of composites using a 3D printer. Some of the properties of PLA filament for applications in 3D printers can be given as follows:

- High printing speed
- Low chemical resistance
- Excellent surface quality
- Very low odor
- Renewable natural raw material
- Compatibility with all printers

Table 4. 1 presents a comprehensive overview of the working conditions and some of the properties of the PLA and other filaments on the 3D printer utilized in this study. The table provides detailed information on the properties of the filament, such as its density, glass transition temperature, as well as printing parameters, including printing temperature, and bed temperature.

Table 4. 1 The details of the working conditions and chemical properties of the 3D printer filaments utilized in this thesis [132]–[138]

Printing condition and chemical properties	**Filament types**				
	PLA	ABS	PEI	TPU	PC
Density (g/cm^3)	1.25	1.04	1.27	1.23	1.20
Glass transition temperature (T_g) (°C)	~55	~105	~215	~-40	~145
Extrusion tip temperature (°C)	210	320	400	220	365
Max. build platform temperature (°C)	60	95	190	60	145

4.2.2 Acrylonitrile Butadiene Styrene (ABS)

In this thesis, ABS-M30 FDM® filament, a product developed and manufactured by Stratasys., was used as 3D printing material. ABS filament is a type of thermoplastic material commonly used in 3D printing. ABS is the acronym for acrylonitrile butadiene styrene, a copolymer made up of three main monomers: acrylonitrile, butadiene, and styrene. ABS filament is popular in 3D printing because of its favorable

physical properties. Its versatility and post-processing capabilities make it suitable for a wide range of applications in various industries, including automotive, aerospace, consumer goods, and prototyping. Some of the characteristics of the ABS filament used in 3D printing applications are as follows:

- High-temperature resistance (100°C)
- High impact resistance
- Surface polishing with acetone
- Suitable for outdoor applications
- High warping behavior
- Excellent surface quality
- Emits odor during printing
- Compatibility with all closed cabinet printers

ABS filament is highly valued in 3D printing due to its favorable characteristics. It exhibits commendable mechanical properties, including a balanced blend of strength, toughness, and impact resistance, enabling printed parts to endure moderate loads and impacts without significant deformation [139], [140]. ABS filament maintains dimensional stability, preserving accurate shape and size even under varying temperatures and environmental conditions, with minimal risk of warping [141], [142]. It possesses good interlayer adhesion, resulting in robust and enduring printed parts suitable for functional prototypes, mechanical components, and structurally demanding models. ABS filament demonstrates good chemical resistance to common substances, though it may be susceptible to specific organic solvents, necessitating careful selection of printing environments [143], [144]. Post-processing of ABS prints is easily accomplished through sanding, painting, and acetone vapor smoothing, enhancing their aesthetic appeal. However, it is crucial to note that ABS filament emits noticeable odors due to the release of volatile organic compounds (VOCs) during printing, warranting adequate ventilation or enclosed printing setups to minimize exposure [145]–[147]. ABS filament finds wide-ranging applications in the automotive, electronics, and consumer goods industries due to its amalgamation of mechanical strength, dimensional stability, bonding capability, and post-processing adaptability.

4.2.3 Polycarbonate (PC)

The current thesis utilized PC FDM® filaments, a product developed and manufactured by Stratasys., as the material for 3D printing. PC FDM® filaments can be categorized as polycarbonate (PC) filaments and are designed specifically for use in high-strength 3D printing applications. Some of the characteristics of PC filament for use in 3D printing applications are as follows:

- Good mechanical strength and toughness
- High impact resistance
- High heat resistance with a glass transition temperature
- Good dimensional stability
- High chemical resistance
- High printing temperature
- Good electrical insulation properties

These properties make PC filament suitable for a range of applications, including automotive parts, electrical components, and medical devices [148]. PC filament is a popular material in 3D printing due to its exceptional mechanical properties. It offers high strength, toughness, and impact resistance, making it suitable for durable parts [149]–[151]. PC filament also exhibits good dimensional stability, maintaining accurate shape and size even in varying temperatures. With a high glass transition temperature of around 145°C to 155°C, it can withstand elevated temperatures without significant loss of mechanical properties. Additionally, PC filament provides transparency for applications requiring visual aesthetics or light transmission. It demonstrates good chemical resistance to substances such as oils, greases, and certain acids [152], [153]. However, precautions should be taken with solvents. Overall, PC filament is widely used in automotive, aerospace, electronics, and medical industries where strong, dimensionally stable, heat-resistant, and transparent 3D-printed parts are needed [154], [155].

4.2.4 Thermoplastic Polyurethane (TPU)

The current thesis utilized Porima TPU Flex® filaments, a product developed and manufactured by Porima Polymer Technologies Co., as the primary material for 3D

printing. Porima TPU Flex® filaments are categorized as thermoplastic polyurethane (TPU) filaments and are designed specifically for use in 3D printing applications. TPU is a type of thermoplastic elastomer that combines the properties of rubber and plastic. TPU filament is also known for its high flexibility and the fac that it can be used for printing on the majority of FDM 3D printers. TPU filament is a flexible 3D printing material that is widely used in various applications. Some of the characteristics of TPU filament for use in 3D printing applications are as follows:

- Demonstrates a high elongation of over 500%
- Exhibits ease of printing compared to similar flexible materials
- Possesses high chemical resistance
- Shows excellent layer adhesion
- Displays exceptional fatigue resistance
- Emits very low odor during printing
- Has low moisture absorption
- Maintains flexibility at low temperatures.

4.2.5 Polyetherimide (PEI)

Polyetherimide (PEI), commercially known as ULTEM 1010, was chosen as the other fabrication filament material due to its superior mechanical properties, excellent thermal stability, and chemical resistance [156]. PEI is a high-performance engineering material that has been increasing in importance in various applications. Developed by Stratasys, PEI is considered one of the strongest thermoplastics for FDM. It can be printed at high temperatures and has good layer adhesion, making it a preferred material for printing complex parts with intricate designs. Some characteristics of PEI filament for use in 3D printing applications are as follows:

- Good mechanical properties
- Excellent thermal and chemical stability
- High strength and stiffness
- Good dimensional stability
- Excellent resistance to creep and fatigue
- High glass transition and printing temperature

- High chemical resistance to acids, bases, and solvents
- Good electrical insulation properties

PEI filament possesses certain notable characteristics that make it suitable for diverse applications [157]. It exhibits exceptional heat resistance with a glass transition temperature (Tg) ranging from approximately 215°C to 217°C, ensuring structural integrity under high-temperature conditions [158]. The filament demonstrates excellent mechanical strength, including high tensile strength and impact resistance, enabling it to withstand heavy loads and impacts without significant deformation [159]. Additionally, PEI filament maintains dimensional stability, preserving the accurate shape and size of printed parts despite temperature fluctuations or environmental variations [160], [161]. It offers resistance to various chemicals, including acids, bases, alcohols, and hydrocarbons, rendering it suitable for applications involving exposure to diverse chemical substances [162], [163]. Furthermore, PEI filament provides good electrical insulation properties, making it appropriate for applications requiring electrical components or insulation [164]. Moreover, PEI filament's transparency allows for the creation of visually appealing and light-transmitting parts. Its combination of properties makes it a preferred choice in industries such as aerospace, automotive, electronics, and healthcare, where it is utilized for functional prototypes, jigs and fixtures, structural components, electrical connectors, and medical devices.

4.2.6 Benzoyl Peroxide (BPO)

Benzoyl peroxide (BPO) is an efficient oxidizing agent with a chemical structure comprising two benzoyl groups linked by a peroxide bridge. Its molecular formula is $C_{14}H_{10}O_4$ and it exists in the form of white, crystalline agglomerates. BPO is soluble in organic solvents but insoluble in water [165], [166]. It exhibits thermal sensitivity and has a melting point in the range of 104°C to 106°C [167].

BPO is widely known for its applications in various fields, including medicine, cosmetics, and polymer chemistry. In medicine, BPO is commonly used as a topical medication for the treatment of acne. It functions as an antibacterial agent by releasing oxygen-free radicals that kill the bacteria responsible for acne breakouts. It also acts

as a keratolytic agent, helping to exfoliate the outer layer of the skin and prevent pore blockage. In the field of polymer chemistry, BPO is a widely used initiator in the polymerization of various monomers, including styrene and acrylics. It decomposes at elevated temperatures, generating free radicals that initiate the polymerization reaction. BPO is known to be a strong oxidizing agent and can cause skin irritation and sensitivity, especially at higher concentrations. It is important to follow proper safety precautions when handling and using BPO.

4.3 Methods

4.3.1 Additive Manufacturing Systems Employed in the Study

In this thesis, two FDM 3D printers were utilized, namely a Stratasys Fortus 450mc, and a Creality Sermoon D1. The Stratasys Fortus 450mc printer is a high-end commercial 3D printer, while the Creality Sermoon D1 is a consumer-level 3D printer. Images of the 3D printers used for manufacturing the test specimens are depicted in Figure 4. 1. The Fortus 450mc 3D printer was used to fabricate materials requiring high processing temperatures, such as ABS, PEI, and PC. Although the printer has two nozzles, only one was employed for the production of the samples, while the other could be used solely for support material.

Table 4. 2 3D printers used in the thesis and their features

Parameters	**3D printer**	
	Fortus 450mc	Sermoon D1
Print area (mm)	406 x 356 x 406	280 x 260 x 310
Max. nozzle temp. (°C)	400	250
Max. bed temp. (°C)	190	100
Layer thickness (µm)	127-330	100-400
Accuracy (µm)	±127	±100
Filament diameter (mm)	1.75	1.75
Machine weight (kg)	601	20.5
Machine size (mm)	1295 x 902 x 1984	500 x 500 x 531
Filaments	ABS, ASA, PC, Naylon, ULTEM 1010/9085	PLA, ABS, TPU

The Sermon D1 printer was modified to integrate a second nozzle into the system, with the aim of enabling agent-based production. Table 4. 2 summarizes the characteristics

of the 3D printers utilized in this study. The first nozzle was used to deposit materials such as PLA and TPU, while the second nozzle was utilized to spray the reinforcement material, benzoyl peroxide. The feasibility of the mechanism was assessed through initial trials conducted with the customized dual-nozzle 3D printer.

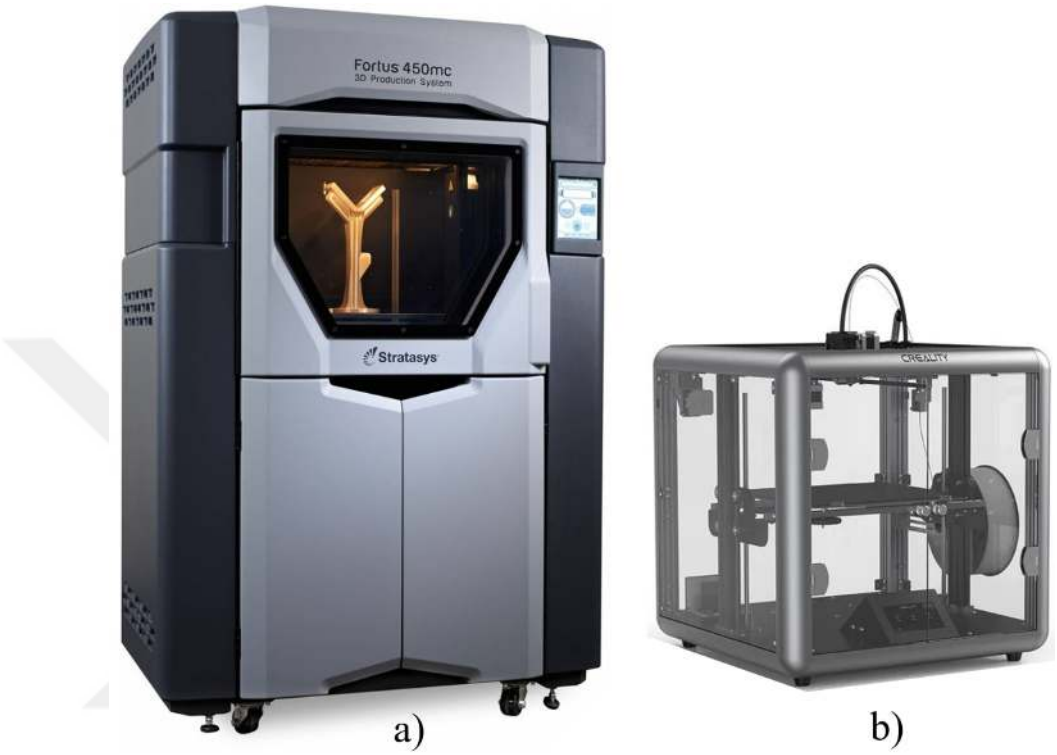

Figure 4. 1 Images of the 3D printers used for manufacturing the test specimens a) Stratasys Fortus 450mc, and b) Creality Sermoon D1

4.4 Characterization and Testing

The chemical composition of the specimens was assessed through Fourier transform infrared (FTIR) spectroscopy, while X-ray diffraction (XRD) analysis was conducted to investigate the samples' crystalline structure. Scanning electron microscopy (SEM) was utilized to examine the fracture surfaces of the 3D printed specimens, preceded by the application of a thin coating of palladium/gold. In addition, a differential scanning calorimetry (DSC) device was used for thermal analysis. Tensile and bending tests were performed using a universal testing device, while the hardness measurements were obtained using a Shore hardness tester. All experiments were carried out under controlled room conditions at consistent temperature and humidity.

CHAPTER 5

DESIGN AND CONSTRUCTION OF EXPERIMENTAL SETUP

5.1 Introduction

This section encompasses the planning, development, and implementation of the robust experimental framework that forms the backbone of the research endeavor. This section aims to provide a comprehensive description of the design and construction aspects of the experimental setup by examining the complicated details of the setup design.

In this thesis, a novel test setup consisting of two nozzles was developed and constructed. This setup represents a new 3D printing system capable of manufacturing agent-based composites. By considering the stress distribution in the target part, the system selectively reinforces specific areas by introducing the agent material through the second nozzle. The resulting structure exhibits varying levels of strength, with composite material applied in regions of high-stress concentration and polymer material used in areas of lower-stress concentration.

5.2 Components and Working Principle for Experimental Setup

This study involved the design of a composite-producing 3D printer equipped with two different nozzles, one for thermoplastic material deposition and the other for spraying reinforcing agent material. This study employed the Creality Sermoon D1 device, commonly found as a 3D printer in the market. Detailed technical specifications of this printer are provided in the preceding section (Table 4. 2).

The Sermoon D1 device (Figure 5. 1) underwent design modifications to incorporate a dual nozzle spray system. This enhancement allows the application of a thin film of liquefied chemical material onto the surface of the printed material, applying specific pressure and flow rates.

After the first nozzle completes each layer, the second nozzle is activated independently to coat designated areas with the chemical agent. This layering process continues until the entire part is produced. Upon completion of production, the parts undergo a curing process, wherein cross-linking occurs through a reaction between the polymer and the peroxide-based chemical.

Figure 5. 1 Picture of the 3D printer device used in the experiments

In this study, a dual-nozzle configuration was implemented on the 3D printer, specifically designed for spraying a reinforcing chemical onto areas of high-stress concentration within the target part. The second needle, which facilitated the spraying process, was incorporated into the system alongside the primary nozzle. The spray system comprised an air atomizing nozzle, compressor, pressure tank, pneumatic fittings, and control unit, ensuring precise and controlled deposition of the reinforcing chemical.

Two distinct spray nozzle samples were selected for the experimental setup. These samples included the Der-mix brand JAGUAR Plus and LP-7 products, both of which are manufactured in Türkiye. These spray nozzles were chosen for their specific characteristics and suitability for the intended application in the study. The JAGUAR Plus model is preferred due to its durable construction, ergonomic design, and efficient atomization of liquid materials. The JAGUAR Plus model has specific features or improvements compared to other spraying nozzles, such as adjustable spray patterns, precise control of fluid flow, and easy maintenance. The JAGUAR Plus spray nozzle is shown in Figure 5. 2. Furthermore, Figure 5. 3 provides the technical drawing of the

components comprising the nozzle, while Table 5. 1 presents the operational properties of the nozzle [168], [169]. These visual and tabular representations offer detailed information about the structure and functionality of the nozzle, facilitating a comprehensive understanding of its design and performance characteristics.

Table 5. 1 The operational properties of the JAGUAR Plus nozzle

Working Pressure	Fluid Pressure	Air Pressure	Needle Diameter	Dimensions (WxLxH)	Weight
3-4 bar	0.2-6 bar	1-8 bar	0.8 mm	45x65x138 mm	526 g

The JAGUAR Plus spray nozzle offers several advantages worth considering. First, it incorporates enhanced graduated adjustment knobs to allow for precise control of liquid, air, and angle settings. This allows for separate and gradual adjustment of the air and angle, enabling fine-tuning of the spray pattern. Secondly, the nozzle boasts an expanded spray range thanks to its improved air cap, enabling coverage over a wider area. Furthermore, its optimized design features a single section for air and liquid inlets, streamlining the flow path and ensuring efficient operation. Finally, the lightweight body of the JAGUAR Plus spray nozzle contributes to its overall ease of use.

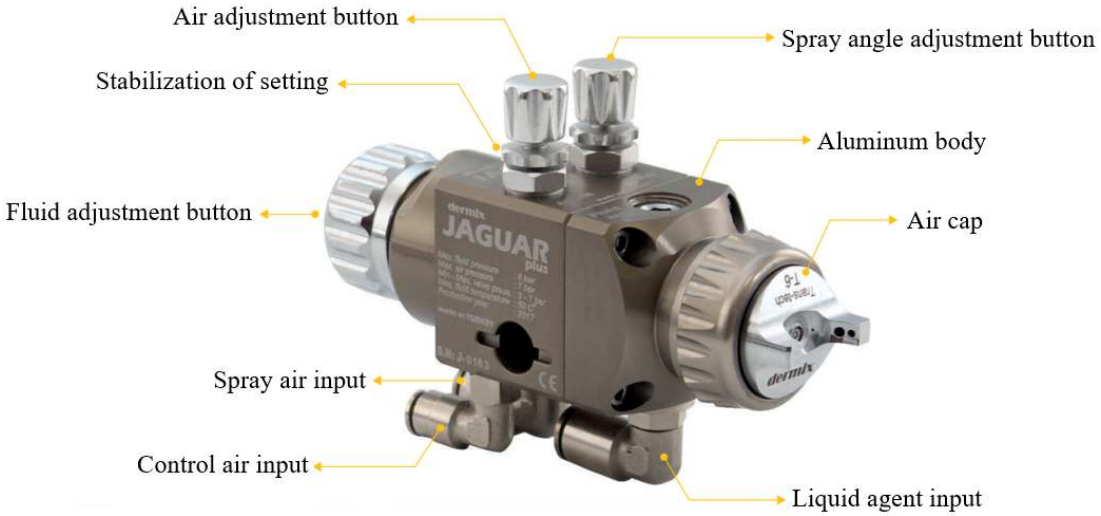

Figure 5. 2 Picture of the JAGUAR Plus spray nozzle

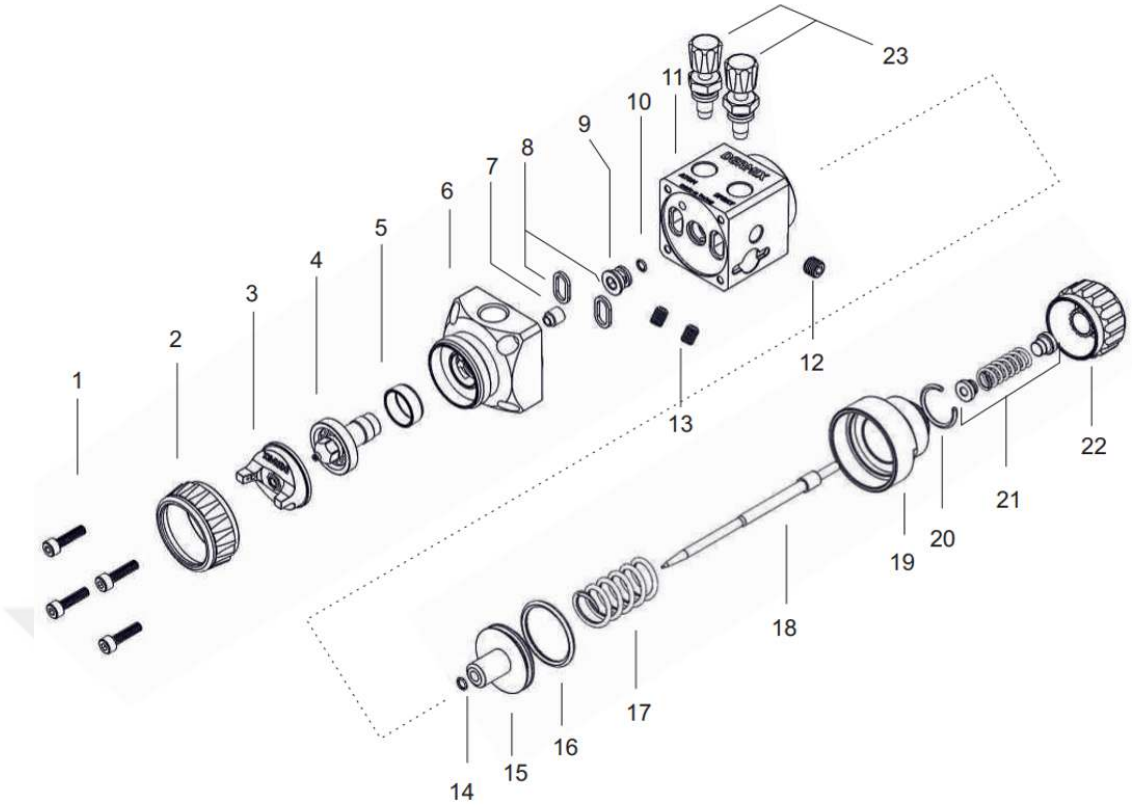

1. Nozzle Screw	9. Needle Seal Spring	17. Piston Spring
2. Air Cap Nut	10. Needle Seal O-Ring	18. Fluid Needle
3. Air Cap	11. Body	19. Spring Holder
4. Fluid Needle	12. Fastening Screw	20. Ball Segment
5. Fluid Needle Seal	13. Air Channel Plug	21. Needle Push Spring
6. Nozzle	14. Piston Inner O-Ring	22. Needle Adjustment Cap
7. Needle Seal Teflon	15. Piston	23. Control Valve
8. Nozzle X-Ring	16. Piston Thread O-Ring	

Figure 5. 3 Technical drawing of the components comprising the JAGUAR plus nozzle

The JAGUAR Plus model is designed for atomizing liquid using air fractionation. By employing this nozzle, the liquid substance is evenly dispersed onto the material surface within an airborne medium. Moreover, in cases where the presence of air may pose a concern or limitation, an LP-7 nozzle was also employed to solely apply the liquid substance.

Figure 5. 4 depicts the LP-7 spray nozzle, showcasing its visual representation. Figure 5. 5 illustrates the technical drawing of the various components constituting the nozzle. This figure serves to present the operational properties inherent to the nozzle [170].

These visual and tabular references serve as resources in providing in-depth insights into the structural intricacies and functional attributes of the nozzle. The LP7 model is specifically designed for the precise dosing of low-pressure liquids within the range of 1-4 bar. It offers the flexibility to accommodate various nozzle thicknesses through the utilization of a replaceable head. This feature allows for the customization of the nozzle according to specific application requirements, ensuring accurate and consistent liquid deposition.

Table 5. 2 The operational properties of the LP-7 nozzle

Working Pressure	Fluid Pressure	Needle Diameter	Dimensions (WxLxH)	Weight
3-4 bar	1-8 bar	0.26-0.84 mm	50x50x135 mm	400 g

Figure 5. 4 Picture of LP-7 spray nozzle

The two nozzles, the Jaguar Plus and LP-7, differ in their spraying characteristics. The Jaguar Plus nozzle sprays in a flat pattern, while the LP-7 nozzle sprays in the form of point or fine lines. The spray patterns of these nozzles are illustrated in Figure 5. 6.

The point spray system of the LP-7 offers a concentrated application of material by delivering a heavy spray to a small area. This system is preferred for applications that demand precise and targeted material application. In contrast, the flat spray system of the Jaguar Plus uniformly sprays a large area. It is suitable for applications that require material deposition on extensive surfaces.

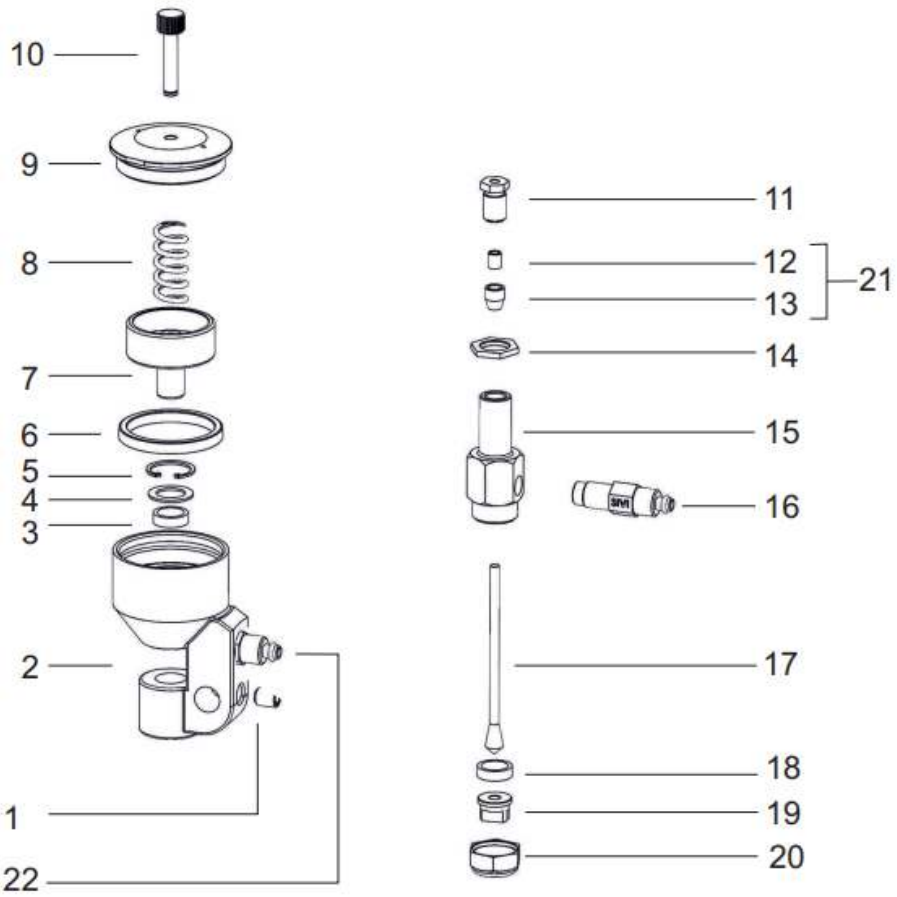

1. Fastening screw	9. Rear cover	17. Fluid needle
2. Body	10. Piston adjustment screw	18. Nozzle seal
3. Bearing felt	11. Connecting screw	19. Flat nozzle
4. Bearing felt washer	12. Inner rod	20. Nozzle nut
5. Bearing felt segment	13. Outer rod	21. Rod assembly
6. Piston seal	14. Fluid inlet body nut	22. Trigger air seat
7. Piston	15. Fluid inlet body	
8. Piston push spring	16. Fluid inlet needle seat	

Figure 5. 5 Technical drawing of the components comprising the JAGUAR plus nozzle

The flat spray system provides more comprehensive coverage, whereas the spot spray system enables more precise and focused material application.

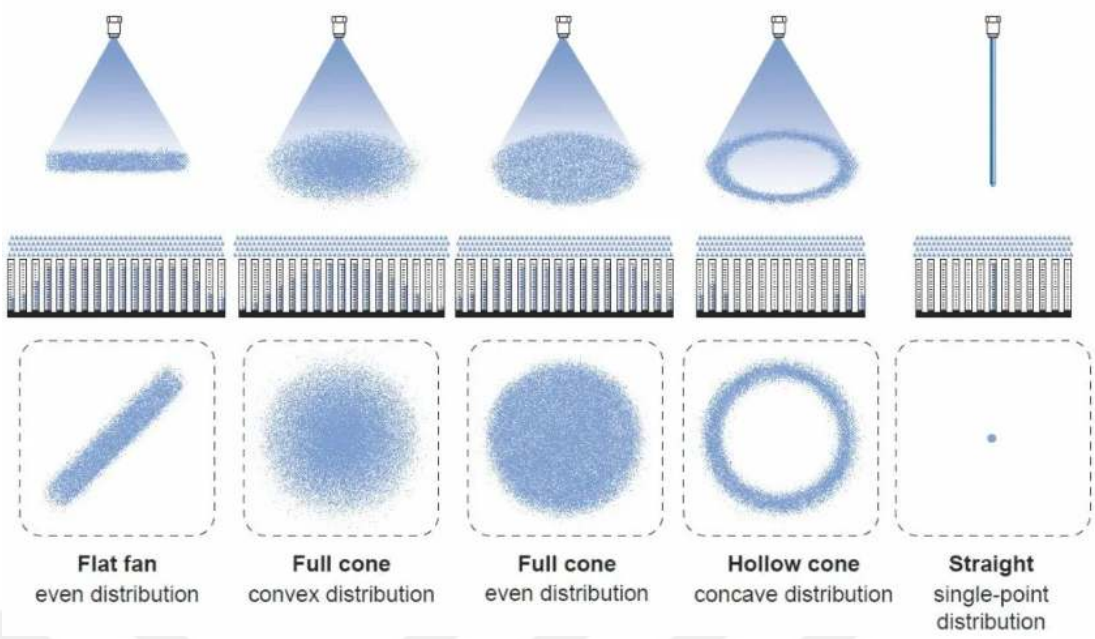

Figure 5. 6 Schematic representation of different spray patterns [171]

In the research conducted, a Dermix brand control unit was used to control the spray system, and the corresponding control system is depicted in Figure 5. 7. The Spray Control Unit operates at 220 V. This control device is employed to regulate the airflow through the solenoid valve. Its key functionalities include adjusting the spray parameters and providing essential controls throughout the spraying operation. This facilitates a more precise and reproducible spraying process. In essence, the presence of a controller governing the spray equipment promotes heightened efficiency, diminished errors, and a safer, well-regulated spraying procedure. The system effectively enhances the performance of automatic spray nozzles, ensuring efficient resource utilization and yielding high-quality outcomes.

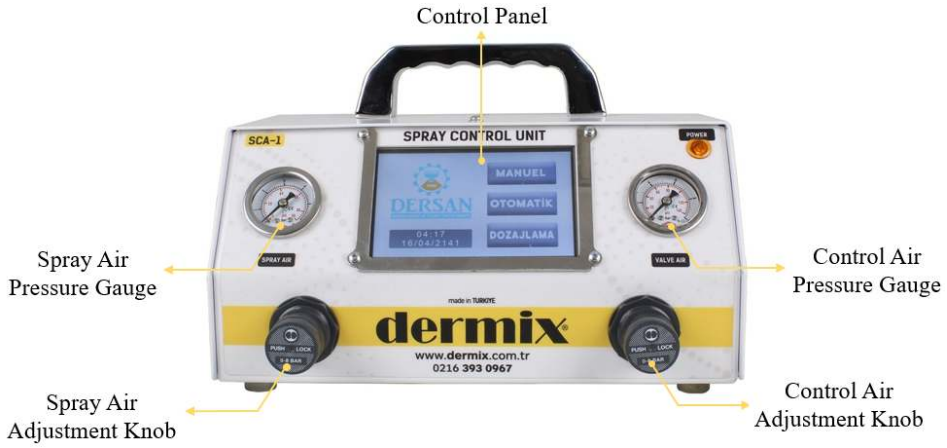

Figure 5. 7 Picture of the Dermix spray control unit

A pressure tank is employed in the spraying system to maintain consistent pressure throughout the spraying process. Figure 5. 8a shows an image of the pressure tank, which was utilized to pressurize the liquefied peroxide material contained within, thereby ensuring a steady flow rate and pressure during spraying. This facilitates precise material deposition and the attainment of desired outcomes. The spray system also incorporated a DALGAKIRAN brand 300 Liter Compressor 8 BAR 3 HEAD 4-HP compressor, as shown in Figure 5. 8b. This compressor supplied compressed air to the pressure tank and spray nozzles. The compressed air serves to atomize the chemical during spraying. The compressor plays a crucial role by enhancing the efficiency of the spraying process and enabling accurate material deposition. The pressure tank and compressor stabilize the spray system, regulate pressure and flow rate, and ensure precise material application. This equipment enhances the overall efficiency of the spraying process and facilitates the attainment of high-quality results.

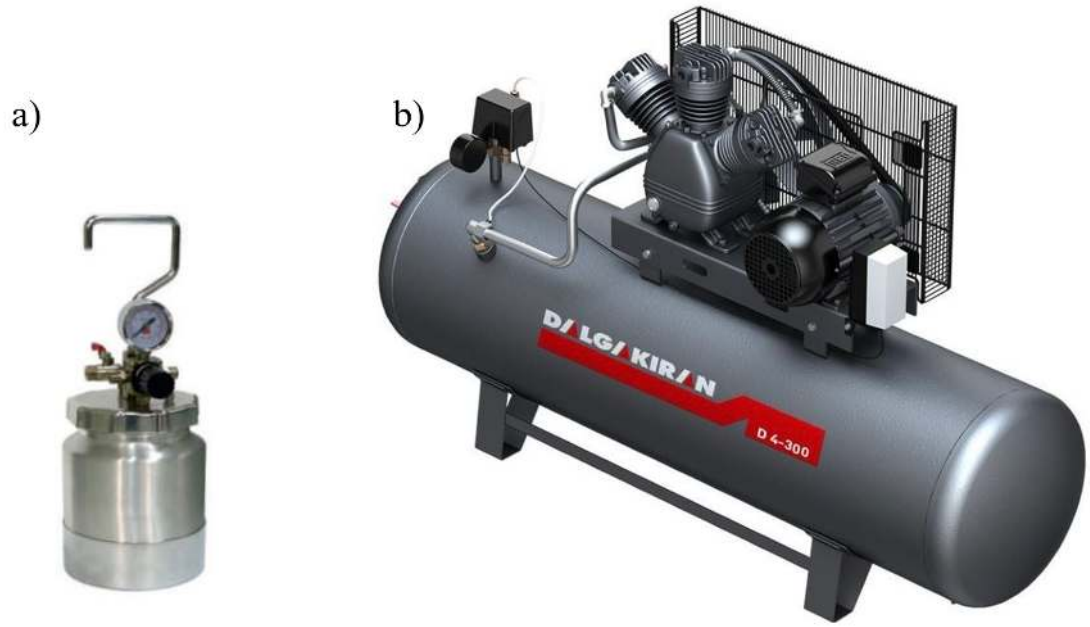

Figure 5. 8 The equipment employed in the spray system: a) pressure tank and b) compressor

The samples, fabricated using a modified 3D printer equipped with a second nozzle (spraying system), were subsequently subjected to a curing process within a curing oven. A Memmert UN110 curing oven was employed in this study. The purpose of the curing oven was to facilitate the cross-linking of the polymer and peroxide materials, thereby completing the polymerization process. The formation of cross-links is essential to the hardening and acquisition of desired mechanical properties in

polymers. Curing ovens enable the formation of these cross-links by subjecting polymer layers or components to controlled heating. Curing ovens are governed by precise heating and cooling cycles, allowing specific temperatures to the maintained for predetermined time intervals. Through this process, the desired physical and mechanical properties of the material are achieved.

5.3 Design of the Experimental Setup

This section of the thesis focuses on the innovative redesign of 3D printers for the production of composites. The objective was to enhance the extruder system of a conventional 3D printer by incorporating a second nozzle, thereby transforming it into a dual-needle printer. However, unlike existing dual-needle printers documented in the literature, the novelty of this design lies in the specific functionality of the second nozzle, which is dedicated to the application of the reinforcement material. In this novel system, the added second nozzle, situated adjacent to the primary nozzle responsible for depositing the matrix material, is responsible for the spraying of the reinforcement material. These two nozzles have the ability to operate independently of each other.

Following the completion of the concept design, the next step involved the identification of suitable nozzles capable of operating at the required pressure and flow rates. Subsequently, the selection of appropriate equipment was conducted, taking into consideration the system dimensions and constraints such as weight and manufacturability. The procurement of the necessary equipment for the spray system was then carried out in accordance with these specifications. This meticulous process ensured that the spray nozzles were adequately supported by the appropriate equipment, enabling their optimal functioning within the designed system. The technical designs of the necessary equipment for operating the Jaguar Plus and LP-7 spray nozzles as the second nozzle are presented in detail in Figure 5. 9. These comprehensive visual representations depict the spraying equipment's working plans, providing insights into their structural components and functional characteristics. This design serves as an essential reference for the implementation and integration of these spray nozzles into the printing system, ensuring their proper functioning in the printing process for enhanced performance and precision.

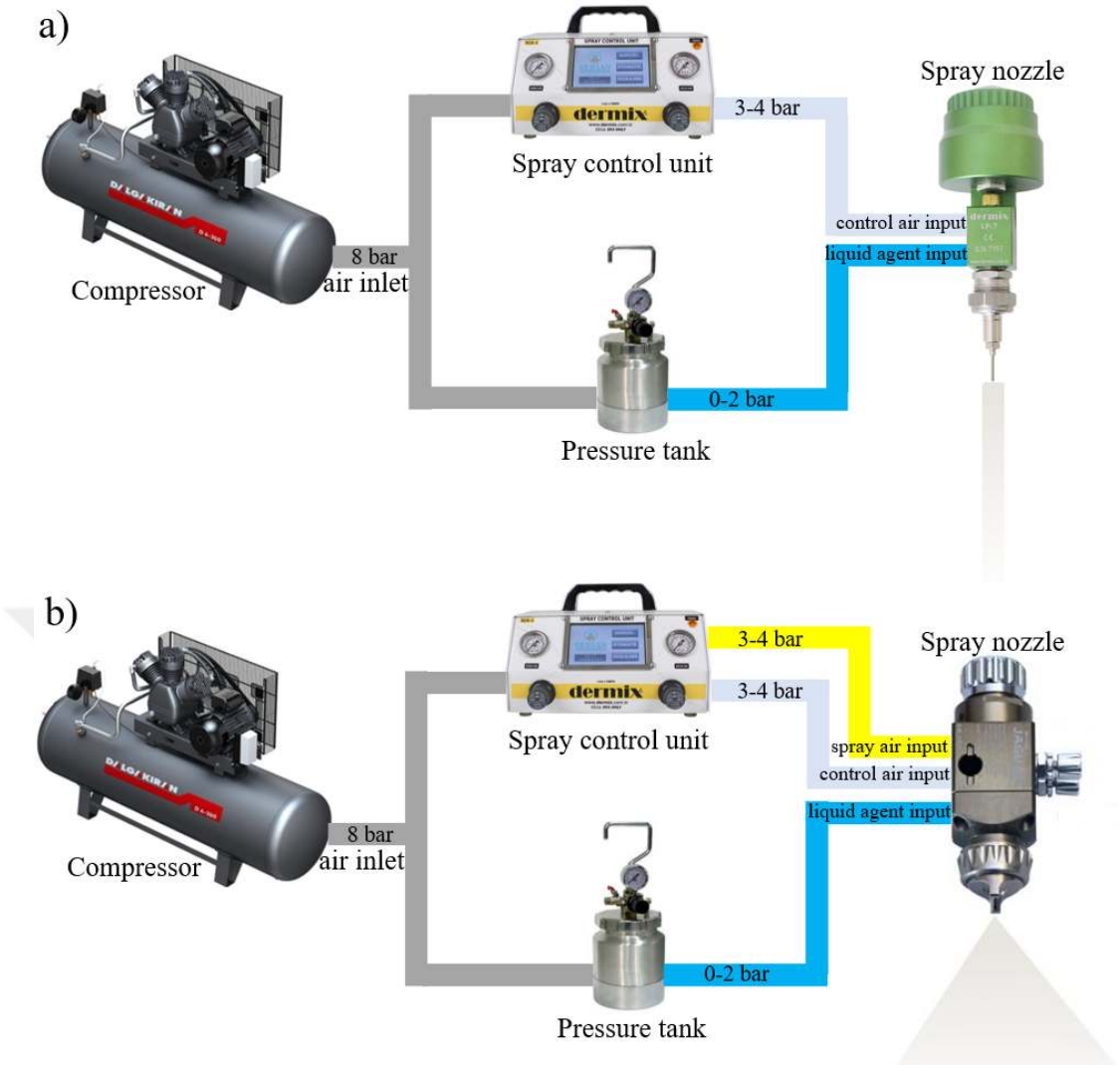

Figure 5. 9 Visualization and operational design of equipment for controlling the spray nozzle as the secondary head a) for the LP-7 nozzle, and b) for the Jaguar Plus nozzle

As depicted in Figure 5. 9, the LP-7 nozzle solely features a control air inlet, whereas the Jaguar Plus nozzle includes a spray air inlet as well. This distinction arises because, unlike the LP-7 nozzle, the Jaguar Plus nozzle employs a mechanism whereby the fluid is atomized through fragmentation, resulting in a flat spraying pattern. The application of spray air pressure supplies the necessary energy to atomize and disperse the liquid material. The liquid is broken into fine droplets by harnessing the force generated by the spray air pressure, facilitating its effective distribution during the spraying process. The utilization of spray air pressure is critical to achieving the desired atomization and ensuring efficient and controlled spraying outcomes.

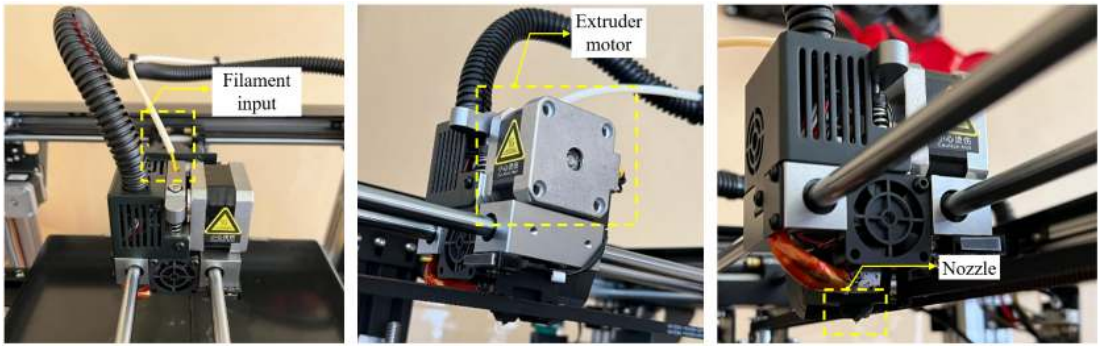

Figure 5. 10 The single-gear direct drive extruder component

A CAD program was utilized to design and incorporate a second nozzle into the extruder component of the printer. This innovative design modification involved attaching an additional nozzle to the existing extruder, allowing the printer to operate with a dual-nozzle system. The printer's extruder part is depicted in Figure 5. 10.

In relation to the second nozzle, a strategic arrangement was envisioned positioned adjacent to the extruder motor. Extensive design investigations were conducted to ensure that this second nozzle would be aligned along the same axis and positioned at the same height as the initial nozzle. This alignment was adopted to establish a harmonized and synchronized configuration between the two nozzles. The Nema 17 stepper motor was employed as the extruder motor in the 3D printer system. Figure 5. 11 depicts both an image of solid and technical drawing of the specific Nema 17 motor [172].

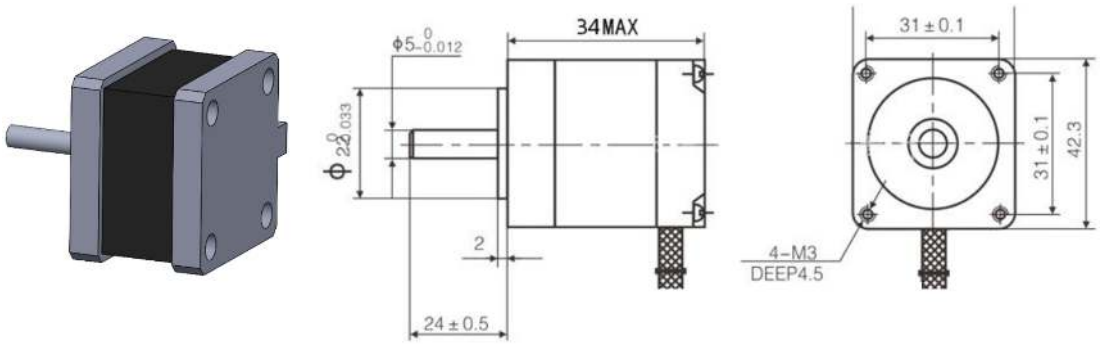

Figure 5. 11 An image of the solid and technical drawing of the Nema 17 motor

Figure 5. 12 showcases the solid model drawings of the holding apparatus designed specifically to accommodate the second nozzles adjacent to the engine. These drawings provide a comprehensive representation of the structural design and

dimensions of the holding apparatus. The purpose of this apparatus is to securely position and support the second nozzle in close proximity to the motor.

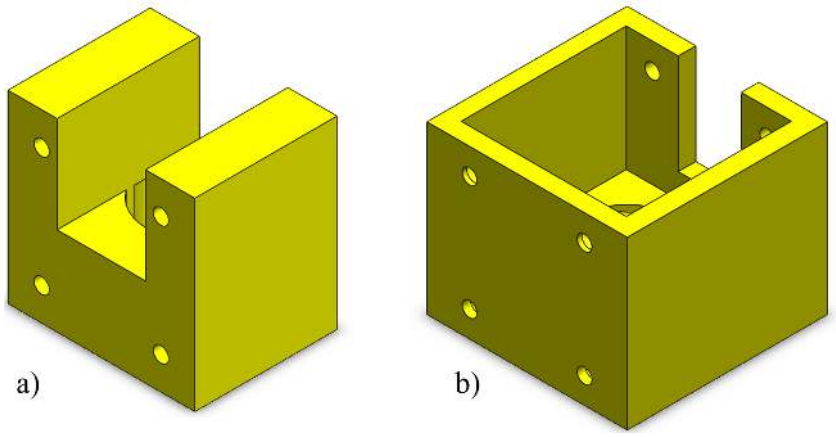

Figure 5. 12 Solid model drawings of the holding apparatus designed for the a) LP-7 nozzle, and b) Jaguar Plus nozzle

Figure 5. 13 and Figure 5. 14 present the assembly drawings depicting the integration of the LP-7 and Jaguar Plus nozzles, respectively, as the second nozzle in the system.

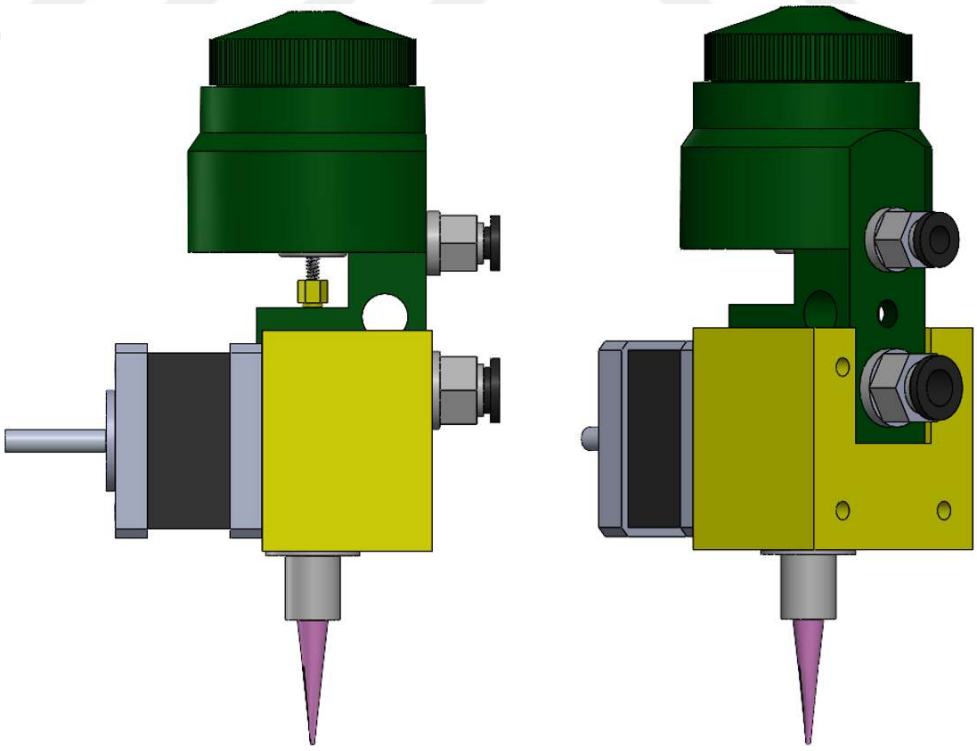

Figure 5. 13 Representation of solid model drawings of the LP-7 second nozzle assembly in the 3D printer extruder from two different angles

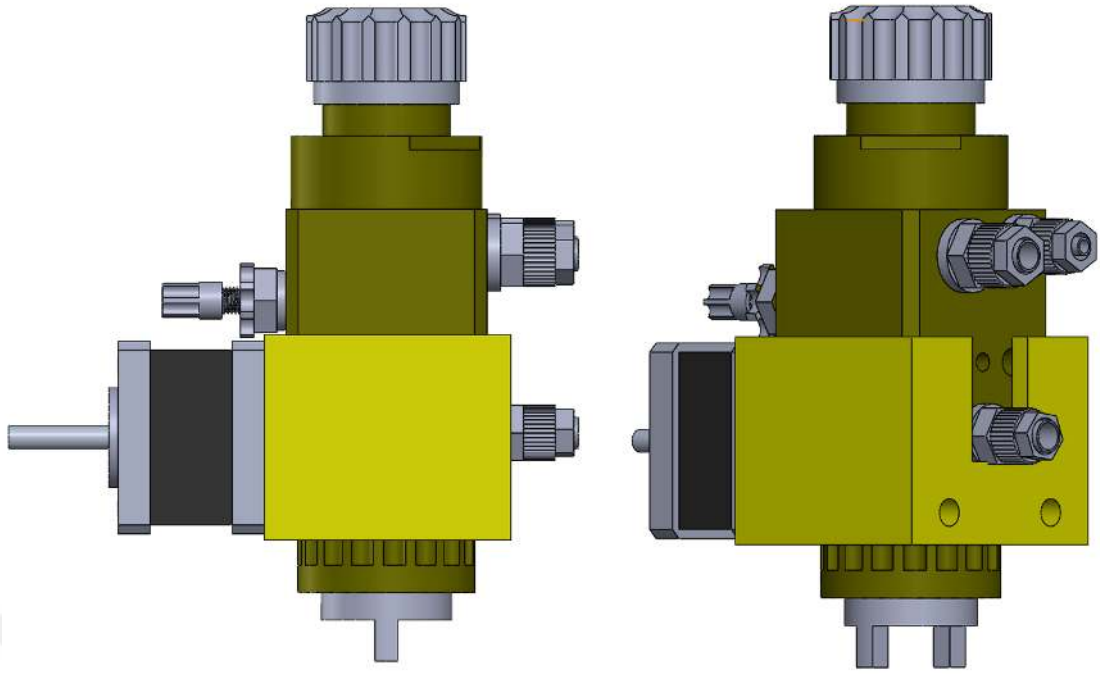

Figure 5. 14 Representation of solid model drawings of the Jaguar Plus second nozzle assembly in the 3D printer extruder from two different angles

The designed apparatus, painted in yellow, is securely affixed to the four corners of the engine using screw connections. Subsequently, the corresponding nozzles are carefully positioned within their respective apparatus. A crucial aspect of the design is to ensure horizontal alignment between each second nozzle and the first nozzle. This meticulous arrangement guarantees proper coordination and synchronization between the nozzles, enabling precise and synchronized material deposition during the printing process. By following this assembly approach, the system achieves the desired configuration, enhancing the overall performance and functionality of the 3D printer.

5.4 Assembly of the Experimental Setup

Figure 5. 15 presents a comprehensive overview of the general assembly view of the 3D printer and the associated spraying system. The image provides a detailed visual representation of the installed system, showcasing each component's precise arrangement and position. The spraying processes described can be effectively implemented by precisely controlling key parameters such as pressure, flow rate, and spraying time and period.

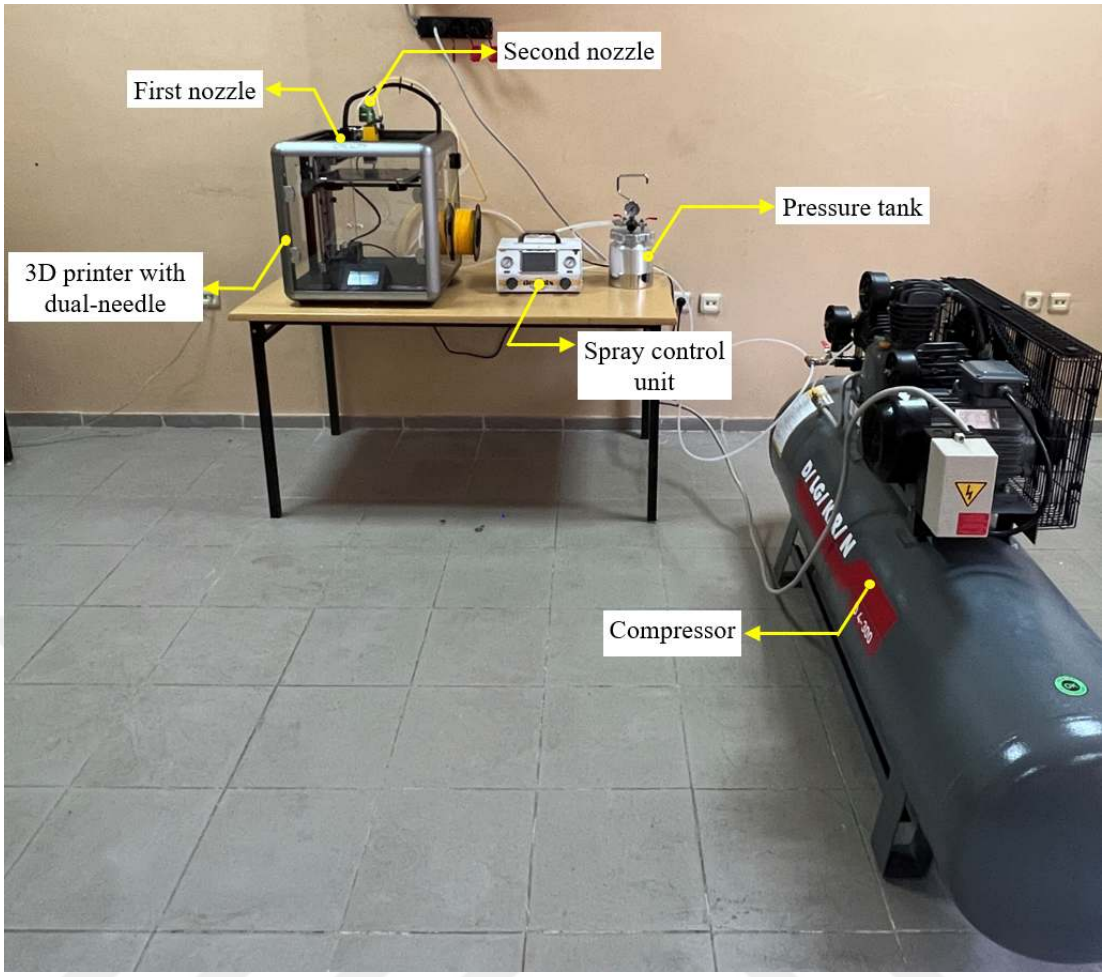

Figure 5. 15 Assembly picture display of the experimental setup

The capacity to manipulate the spray time allows for precise timing and synchronization in accordance with the specific requirements of the application. In this context, an approach was undertaken to reinforce specific regions of the part by selectively spraying an agent solely on those targeted areas. The spraying system initiates with a compressor generating a pressure of 8 bar. This pressurized air is subsequently directed to both the controller unit and the pressure tank. Within the pressure tank, the air pressure is regulated to a range of 0-1 bar, while the controller unit further reduces it to a pressure between 3-4 bar. The air discharged from the controller unit is then directed to the second nozzle, which functions as the spray nozzle. The control unit automatically adjusts pressure, angle, and flow control. Furthermore, the nozzle is equipped with valves that enable manual control over pressure, angle, and flow.

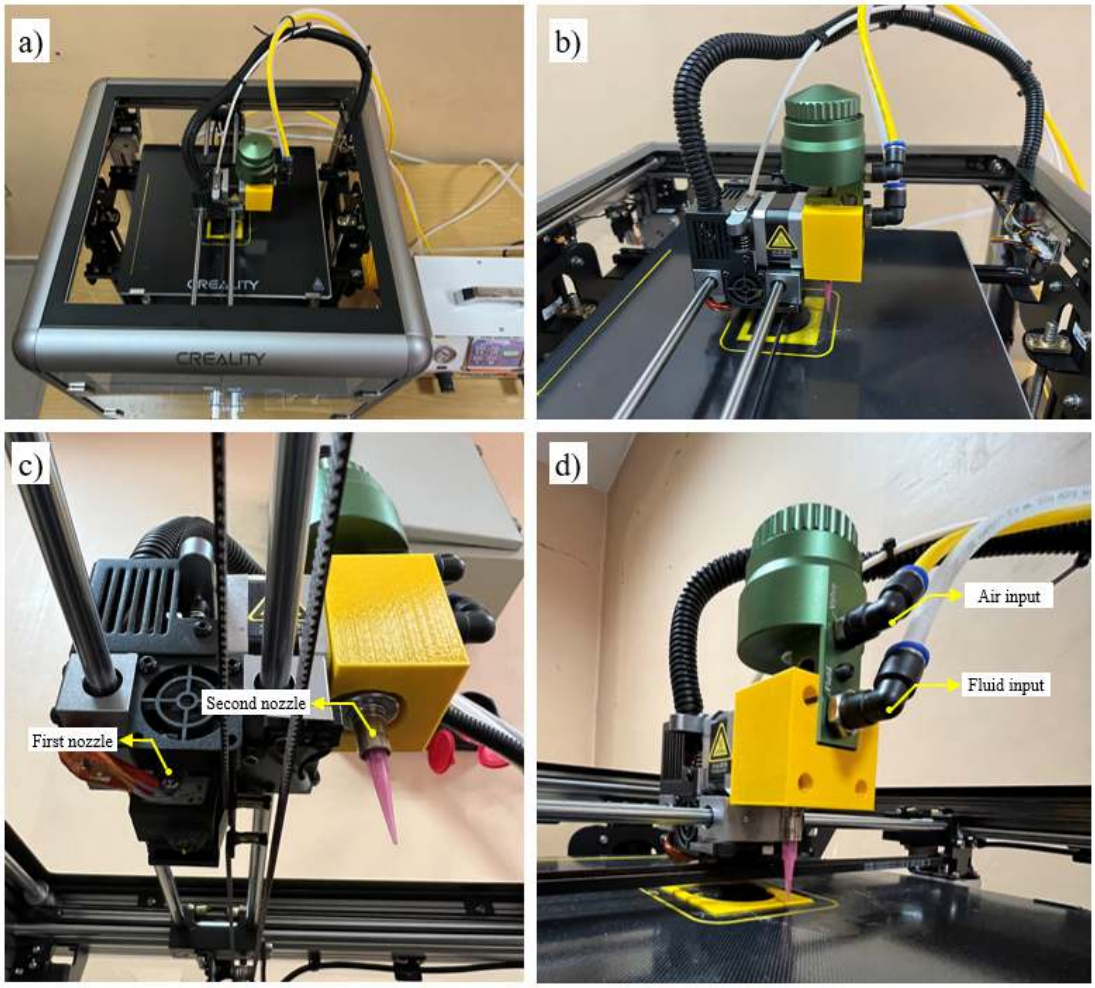

Figure 5. 16 Visual depiction of the dual needle extruder system configuration: integration of the LP-7 nozzle

Figure 5. 16 presents a series of images showcasing the extruder system following the integration of a second nozzle. Figure 5. 16a provides a comprehensive view of the 3D printer, while Figure 5. 16b, c, and d illustrate the extruder configuration with the inclusion of the LP-7 nozzle. Figure 5. 16c shows a detailed view of the first and second nozzles from a distinct perspective, highlighting their alignment along the *x*-axis. This visual representation provides valuable evidence of the accurate alignment of the dual nozzles, ensuring their optimal functioning within the experimental setup. The alignment of the nozzles is crucial to achieving precise and consistent extrusion during the additive manufacturing process. Furthermore, Figure 5. 16 presents a series of images depicting the process of sample production.

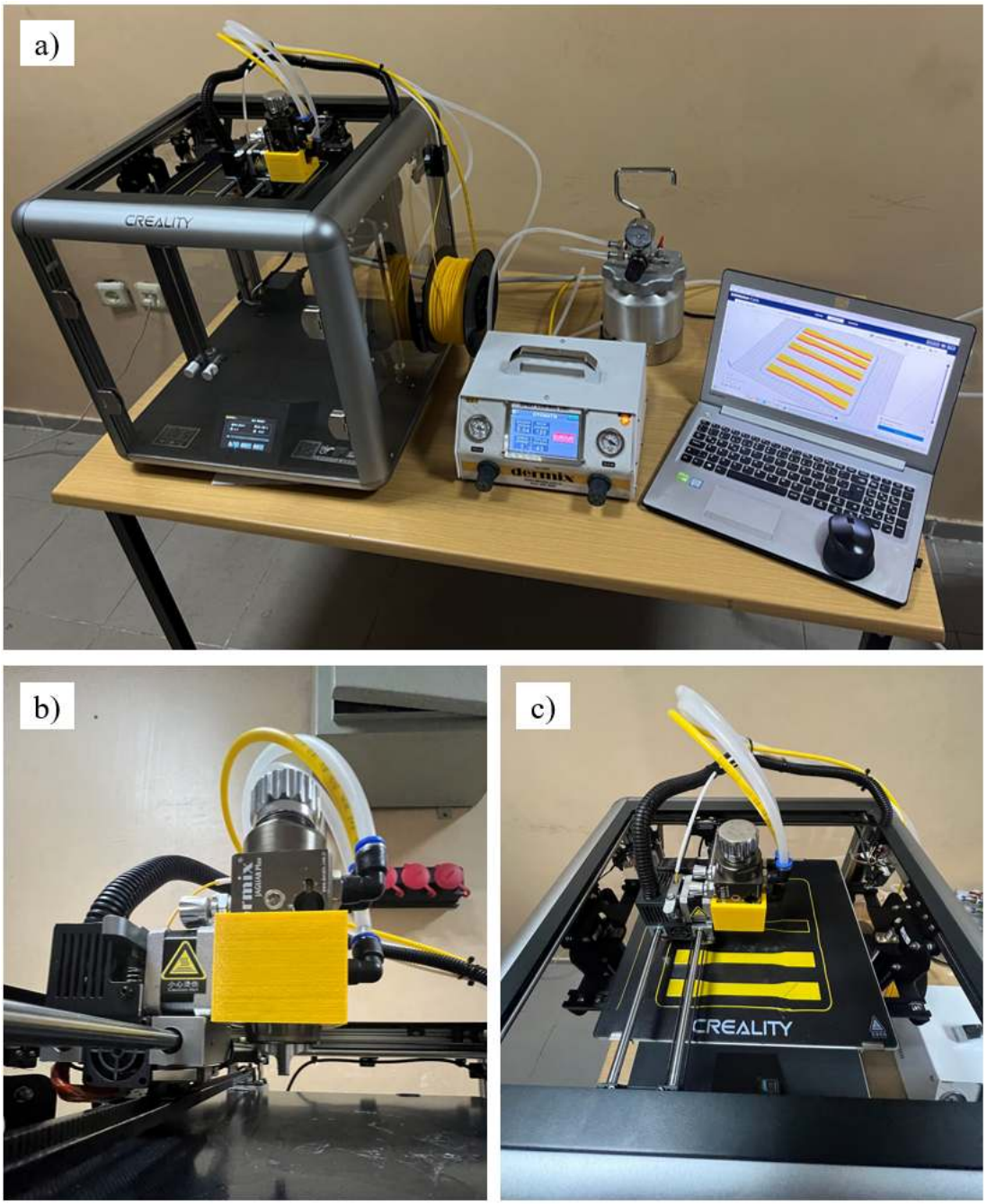

Figure 5. 17 Visual depiction of the dual needle extruder system configuration: integration of the Jaguar Plus nozzle

Figure 5. 17 shows the assembled 3D printer capable of dual-needle (with Jaguar Plus nozzle) operation and agent-based production, indicating the successful completion of assembly and trials. Furthermore, the figure presents the working operation of the nozzles along with images of the produced sample. To facilitate the connection of the second nozzles, their respective connection hoses are merged with the filament connection hose of the first nozzle. Notably, both the first and second nozzles are

aligned along the *x*-axis, as demonstrated in Figure 5. 17. However, on the *z*-axis, the second nozzles are deliberately positioned higher than the first to establish a designated spray area. This arrangement is crucial to enabling precise and controlled application of the agent onto the desired regions of the target object.

Figure 5. 18 illustrates a photograph capturing the process of sample production. The photograph captures the sequential operation of the first and second nozzles during the layering process. As the first nozzle completes its layer, the second nozzle seamlessly activates, dispersing the spray uniformly across the entire layer. The images captured in this figure serve as visual representations, showcasing the successful implementation and operation of the spray system in the experimental setup.

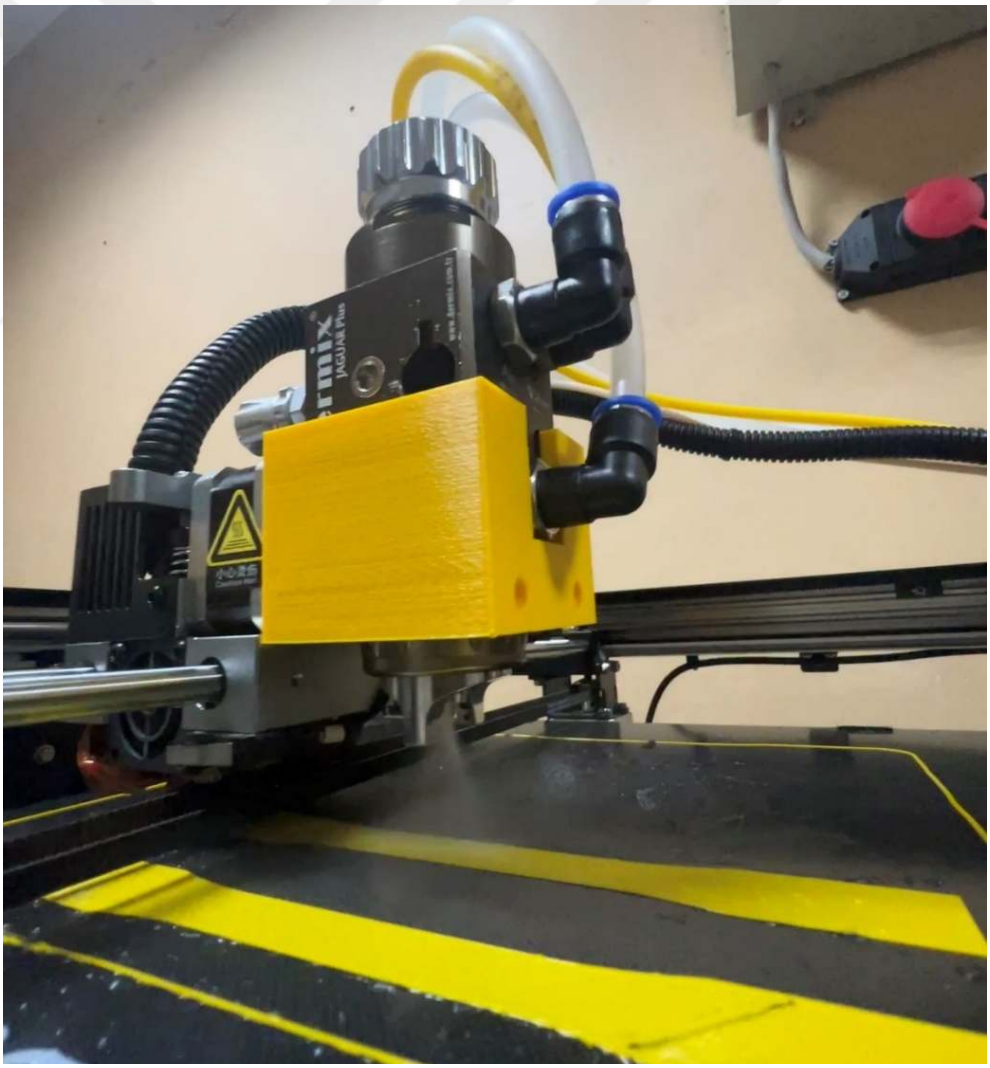

Figure 5. 18 A general picture of the experimental setup

CHAPTER 6

IN-SITU MANUFACTURING OF A NOVEL CROSS-LINKED COMPOSITE MATERIAL FOR FUSED DEPOSITION MODELING IN ADDITIVE MANUFACTURING

6.1 Introduction

This section presents the research findings on the production of in-situ composites through additive manufacturing. The focus was on studying the changes in the mechanical properties of the composite material achieved by applying peroxide spray using a second nozzle integrated into a conventional FDM 3D printer. The study aimed to investigate the manufacturability of in-situ composites and involved characterization and mechanical testing. The results so obtained are discussed and reported in this section.

6.2 Materials

The present study utilized several thermoplastic materials, including polylactic acid (PLA), and thermoplastic polyurethane (TPU). Furthermore, benzoyl peroxide (BPO) and polyvinyl acetate (PVA) were employed as reinforcement materials. PLA and TPU were used as matrix materials in the production of composites using a 3D printer. The chemical structure of PLA and BPO are shown in Figure 6. 1 and Figure 6. 2, respectively. Table 6. 1 provides a detailed summary of the operating parameters of the PLA and TPU filaments used in this study.

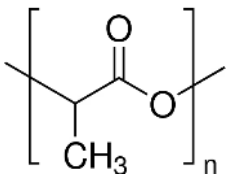

Figure 6. 1 Chemical structure of PLA

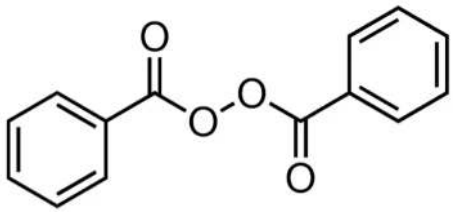

Figure 6. 2 Chemical structure of benzoyl peroxide

Table 6. 1 presents a comprehensive overview of the working condition of the PLA and TPU filaments on the 3D printer utilized in this study. For this study, benzoyl peroxide was employed as an initiator and cross-linking agent in combination with the polymer after being dissolved in acetone.

Table 6. 1 The details of the working conditions and chemical properties of the 3D printer filaments used in this thesis

Printing condition and chemical properties	Filament types	
	PLA	TPU
Layer thickness (µm)	200	
Infill density (%)	100	
Raster angle (°)	45/45	

6.3 Methods

The new experimental setup was used to fabricate PLA and TPU materials. The 3D printer used in this study was modified by adding a second nozzle to the system with the aim of producing composites. The first nozzle was used to deposit materials such as PLA and TPU, while the second was utilized to spray the reinforcement material, benzoyl peroxide. The feasibility of the mechanism was assessed through initial trials conducted with the customized dual-needle 3D printer. Figure 6. 3 shows a schematic image depicting the modified 3D printer process used in this study, wherein a second nozzle has been incorporated. Details of these setups are given in Chapter 5.

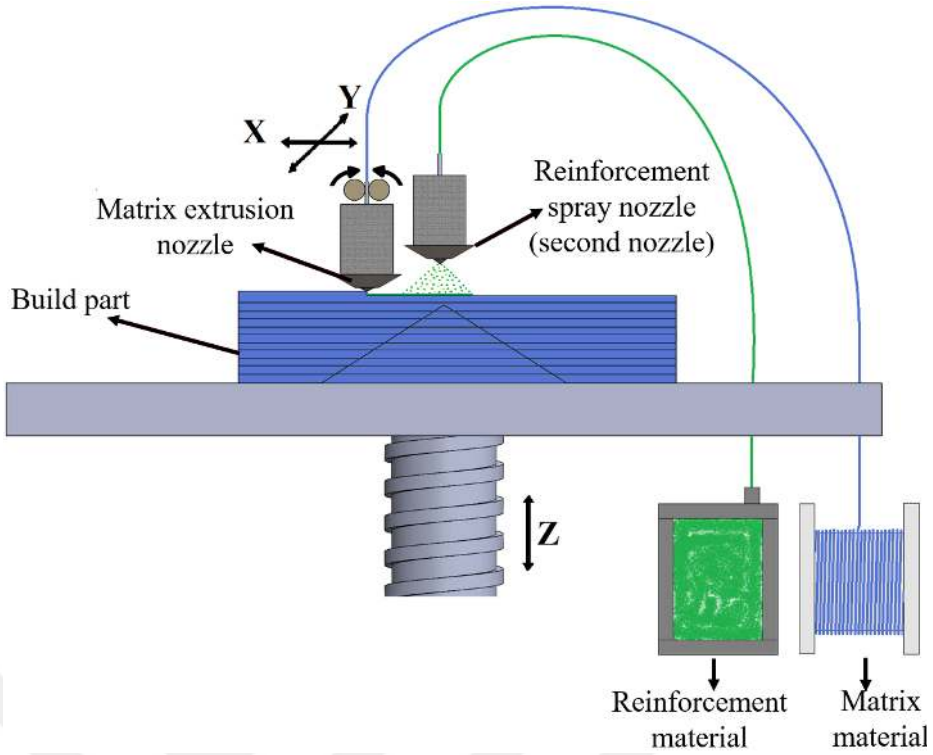

Figure 6. 3 Schematic representation of the composite production process with a 3D printer

6.3.1 Sample Preparation

The experiments were conducted in two stages. In the preliminary stage, various matrix polymer materials and different agents were investigated. The matrix and agent materials that exhibited improved tensile test results in the preliminary tests were selected for the second phase of the study. In the first stage, TPU and PLA filaments were utilized as the matrix material, while benzoyl peroxide and polyvinyl acetate materials were employed as agents. In the second stage, PLA and benzoyl peroxide, which demonstrated enhanced mechanical properties, were chosen as the matrix and agent materials, respectively, and the research focused on these two materials.

The matrix material was a commercially available PLA filament, while the reinforcement material was a commercially available benzoyl peroxide powder. The benzoyl peroxide powder was dissolved and turned into a liquid solution. In the production of PLA samples, a liquid solution of benzoyl peroxide was applied between each layer using a second nozzle. The samples were produced with a layer resolution of 0.28 mm and a printing speed of 50 mm/s. The 3D models were created with a 45° x 45° raster angle. The printing process was performed at a nozzle temperature of

210°C, a build platform temperature of 60°C, and with fan cooling. The Ultimaker Cura program, version 4.8.0, was used for slicing. Figure 6. 4 illustrates the schematic representation of some process parameters used for this study.

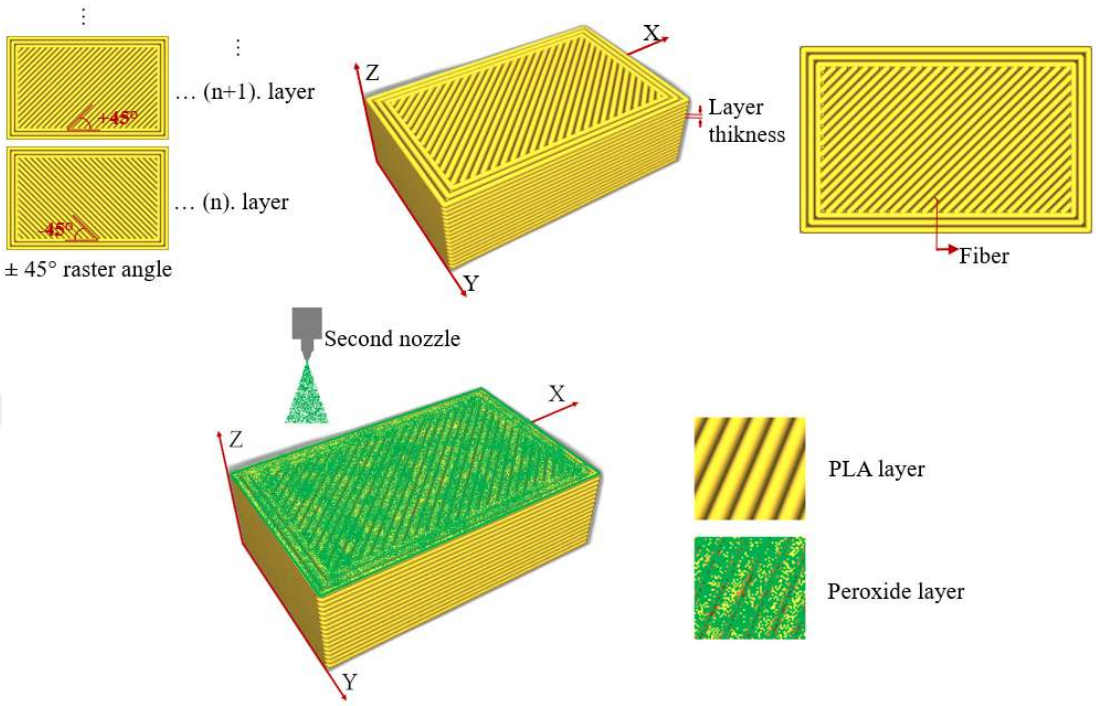

Figure 6. 4 Schematic representation of some process parameters and composite production method

Initially, samples were produced using PLA filament without applying any process on the 3D printer. Subsequently, during the production of PLA samples, liquefied peroxide was deposited as a thin film using a second nozzle between each layer beginning from the first layer; this procedure was continued throughout the entire production.

As illustrated in Figure 6. 5, the samples were generated in the XY orientation, and peroxide was deposited in the XY orientation between each layer. Following production, the curing process was conducted by keeping the samples in the drying oven for 1, 2, and 3 hours to create a cross-linked structure between PLA and peroxide. To precisely assess the mechanical property alteration that may occur in the samples due to the temperature applied during curing and the cross-linking between the polymer and peroxide, the curing process was also performed for the samples produced solely with PLA without the addition of peroxide.

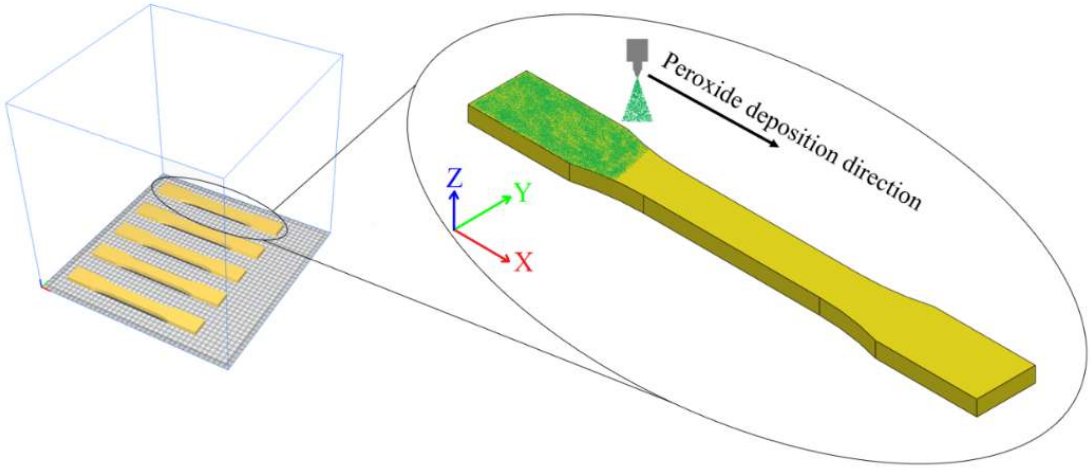

Figure 6. 5 Schematic representation of tensile test specimens and building orientation

6.3.2 Characterization and Testing

The chemical structure of the specimens was analyzed using Fourier transform infrared (FTIR) spectroscopy with a Shimadzu IRTracer-100 spectrometer at room temperature. The fractured surfaces of the 3D-printed specimens were studied using a Jeol 6390LV scanning electron microscope (SEM) to determine the fracture effect on fibers. Prior to SEM analysis, the specimens were coated with a thin layer of palladium/gold. The tensile testing of samples was conducted using a Shimadzu AGX universal testing device (50 kN load capacity). The standard tension tests were carried out in accordance with ASTM D638 with a strain rate (ἑ) of 5 mm/min [173]. Five identical samples were produced for each test condition, and the test values were evaluated by averaging the results of five successive measurements.

6.4 Results and Discussion

This section presents the comprehensive findings from the experimental investigation of the mechanical and morphological characteristics of the newly developed cross-linked PLA composite specimens. The study aimed to assess the impact of cross-linking on the interlayer adhesion and mechanical properties of 3D-printed PLA composite materials. FTIR, SEM, and tensile test results are discussed to evaluate the structural and performance changes induced by the annealing process.

6.4.1 FTIR Spectroscopy Results

This section presents and analyzes the FTIR spectra of the samples in detail. The FTIR spectra provide valuable information regarding the chemical composition and bonding structure of the materials under investigation. A comprehensive understanding of the molecular structure and functional groups was obtained by examining the spectral regions and identifying specific absorption bands. Furthermore, a comparison of the FTIR spectra before and after cross-linking allows any chemical changes or modifications that may have occurred to be assessed.

Figure 6. 6 displays the FTIR spectra encompassing the spectral range of all samples used in the study. The FTIR spectra shown in Figure 6. 6a confirm the chemical structure of PLA, aligning with the reported IR spectra in the literature [174], [175]. The IR spectra of polylactic acid reveal prominent bands associated with the intense C=O stretching vibration at 1757 cm^{-1}, as well as the C-H stretching vibrations of $-CH_3$ at 2996 cm^{-1} and 2945 cm^{-1}. Furthermore, distinctive absorption bands attributed to the ester C-O stretching vibration are apparent at 1080 and 1187 cm^{-1} [176].

Comparison of the IR spectra of PLA samples subjected to three different curing durations reveals the presence of characteristic PLA bands at wavelengths of 1187, 1757, 2996, and 2945 cm^{-1} across all three samples. This indicates that the curing process does not induce any chemical alterations to the PLA samples.

The FTIR spectra of the composite samples obtained at various curing times were examined to assess the formation of chemical bonds between PLA and peroxide molecules. In Figure 6. 6b, the FTIR spectra of the composite sample cured for one hour exhibited the same chemical structure as the PLA samples prior to peroxide application. This suggests that one hour of curing is insufficient to initiate cross-linking, as no structural changes were observed. However, notable differences were observed in the FTIR spectra of the samples cured for two and three hours, indicating the onset of a chemical interaction.

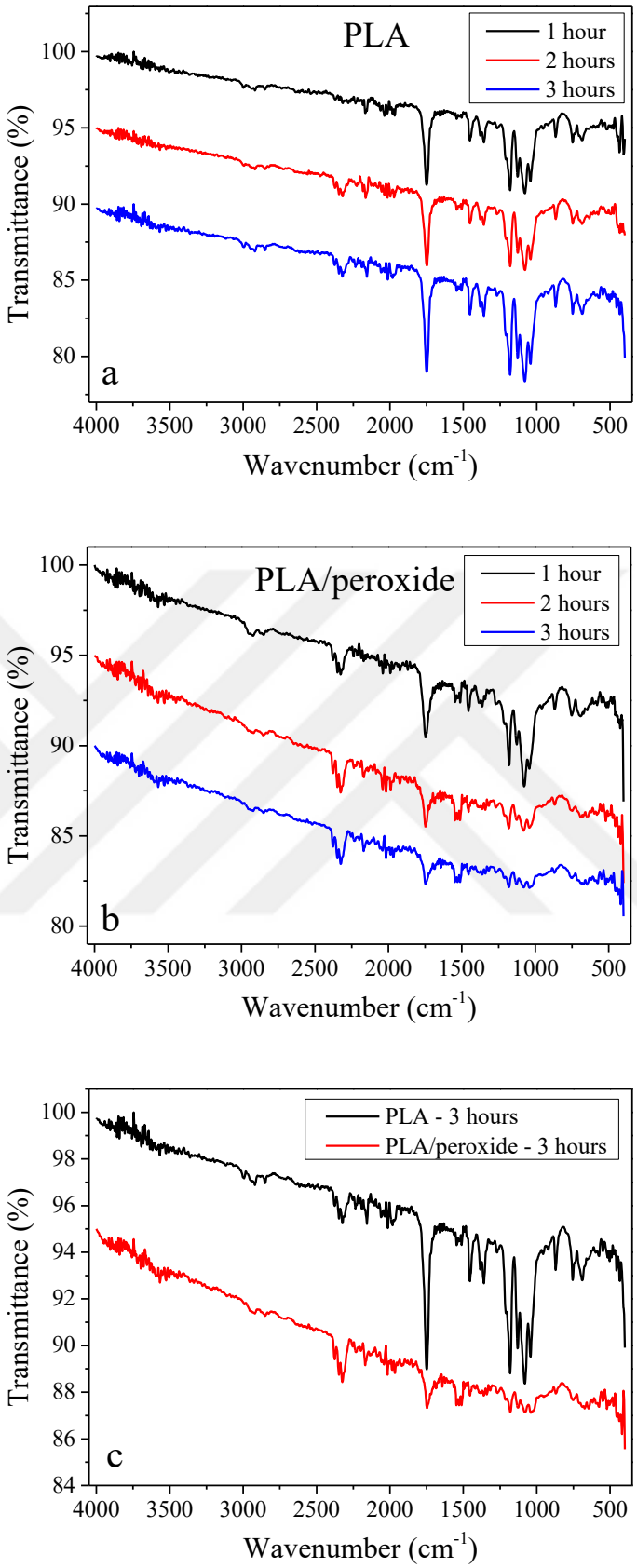

Figure 6.6 FTIR spectra of a) PLA samples, b) PLA/peroxide composite samples, c) PLA and PLA/peroxide samples cured for three hours, d) PLA and PLA/peroxide samples cured for three hours at 1500-500 cm^{-1} (continue)

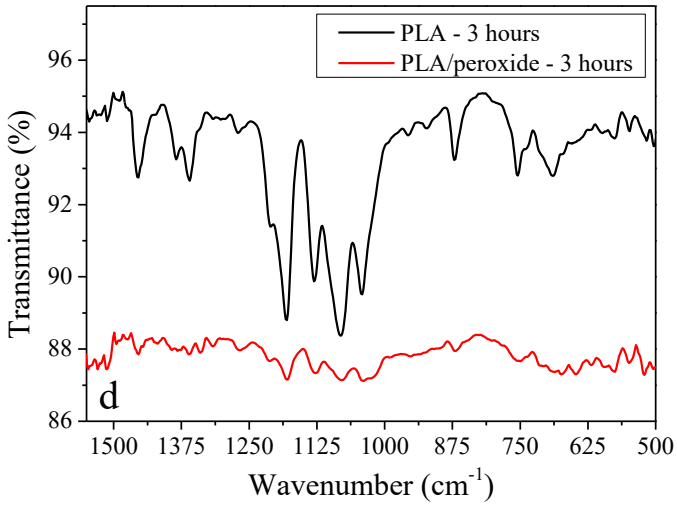

Figure 6. 6 FTIR spectra of a) PLA samples, b) PLA/peroxide composite samples, c) PLA and PLA/peroxide samples cured for three hours, d) PLA and PLA/peroxide samples cured for three hours at 1500-500 cm^{-1}

To further investigate this interaction, Figure 6. 6c and d present detailed spectra. A comparative analysis of the three-hour cured PLA and PLA/peroxide composite samples unveiled noticeable disparities in their chemical structures. Significant attenuation of the C-O-C stretching vibrations band at 1187 cm^{-1} was observed in the peroxide-reinforced PLA composite, particularly when examining the range 1500-500 cm^{-1}.

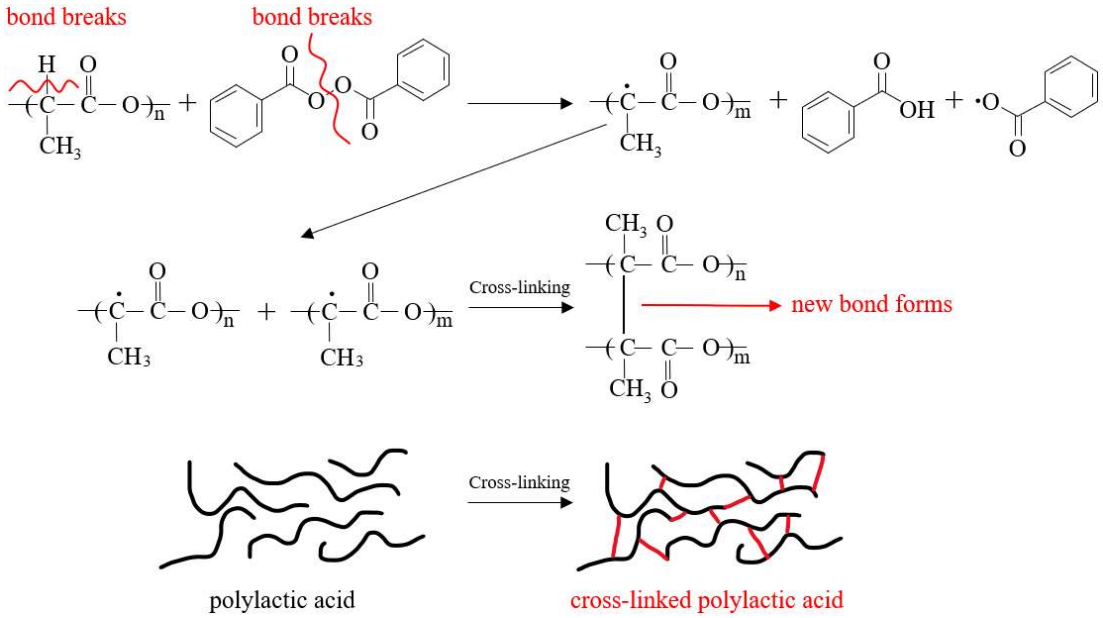

Figure 6. 7 One possibility of bond structure as a result of cross-linking

These spectral changes indicate a chemical alteration in the structure, signifying an interaction between PLA and peroxide. It can be inferred that the PLA bonds in this region engage with the peroxide, thereby initiating the cross-linking process. Figure 6. 7 shows the bond structure of the possible cross-linking reaction after PLA and BPO reaction. To understand how PLA behaves, it is essential to consider the high-temperature mechanism of BPO action (Figure 6. 7). The process initiates with the thermal breakdown of BPO, resulting in the formation of primary radicals. Subsequently, these primary radicals abstract hydrogen from the polymer chain, leading to the generation of polymer radicals. Finally, polymer radicals engage in bimolecular recombination, forming carbon-carbon cross-links [177], [178]. Consequently, the chemical cross-linking structure between PLA molecules could take place as shown in Figure 6. 8.

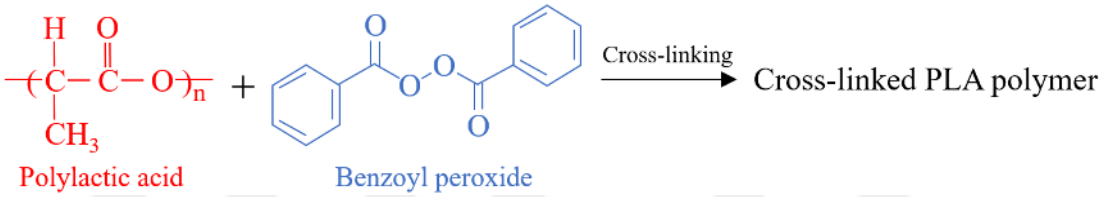

Figure 6. 8 One possible reaction scheme for chemical cross-linking

6.4.2 Microstructural Analysis Results

SEM analysis was conducted on all 3D-printed samples to explore the impact of fracture mechanisms and the influence of peroxide addition. Figure 6. 9 shows the fracture surface observations obtained from various PLA samples fabricated using a 3D printer. Figure 6. 9a depicts SEM analysis images of the fractured surfaces resulting from the tensile testing of PLA samples. Upon examining the surface morphology, two distinct fracture behaviors can be observed. In certain regions of the samples, fiber breakage was observed, while other areas exhibited interface bond fracture as the primary failure mode. These fracture modes are inherent to the three-dimensional structures composed of sequentially layered fibers arranged orthogonally in FDM-based 3D printers. Weak interface bonds have been identified as a prominent factor causing the reduced strength of products manufactured via 3D printing. Moreover, previous studies have reported that the occurrence of fiber fracture errors, in conjunction with interface bond breakage errors, further diminishing the strength of these products [59], [60].

In Figure 6. 9a, the presence of micro-voids within the contour is prominent, with specific voids indicated by yellow lines. Upon examining the interfacial bond rupture region of the PLA sample and the surface of individual fibers, it is evident that the fiber surfaces appear smooth and flat. This smooth surface structure is consistently observed in all PLA samples and across different regions within each sample (see Figure 6. 9b, c, d, e, and f). The observed smooth and flat regions indicate incomplete interfacial bonds with adjacent fibers, resulting in weakened areas in terms of strength. Upon examining the interfaces, particularly in Figure 6. 9f and other figures, it is evident that the interfacial bonding between the consecutive fibers is poor.

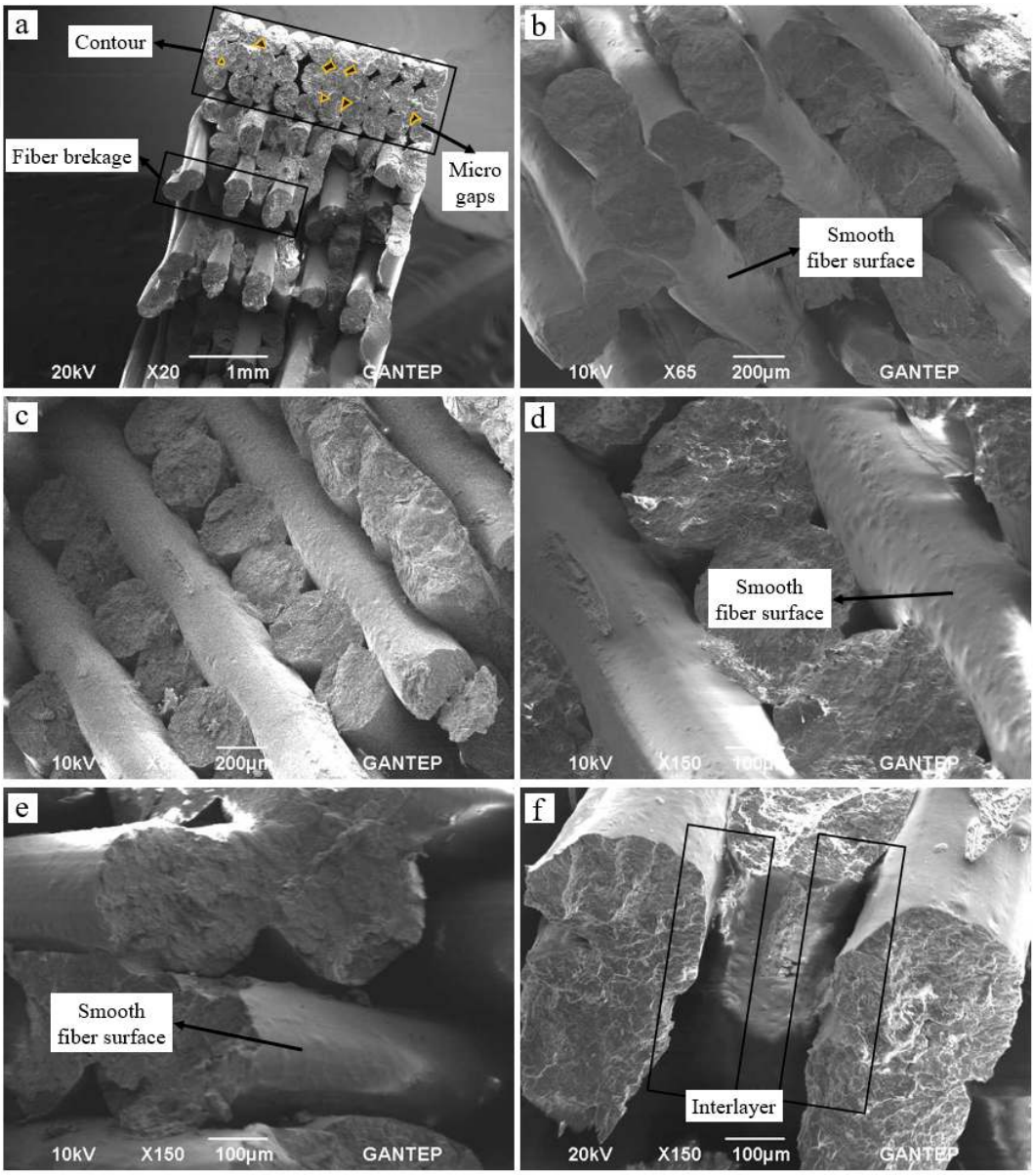

Figure 6. 9 SEM micrographs illustrating the fracture surfaces of PLA samples in general

The SEM analysis results of reinforced PLA composite samples cross-linked with peroxide are depicted in Figure 6. 10. Similar to the PLA samples, two fracture mechanisms are observed in the composite samples. However, comparing the microstructures between PLA and peroxide-reinforced PLA composite reveals significant differences. First, in Figure 6. 10a, micro voids are observed in a typical fashion, but a substantial portion of them appear to be closed. This was attributed to the cross-linking process, which combines peroxide and PLA molecules, resulting in the closure of voids. Furthermore, Figure 6. 10b, representing an enlarged view, demonstrates a more pronounced filling of these micro-voids.

Figure 6. 10c, d, and e illustrate the examination of the interfacial bond region in the peroxide-reinforced composite, revealing poor interfacial bonding with the side layer. However, a relative improvement can be said when comparing the peroxide-reinforced composite samples to the PLA samples. In contrast to the PLA sample, the fiber surfaces exhibited a rough structure. The presence of a rough surface structure on the fibers was consistently observed across all images obtained from various samples and different surface regions within these samples. The observed rough structure on the fiber surfaces is attributed to the cross-linking of peroxide molecules with PLA molecules.

The rough structures observed on the fiber surfaces are believed to be the result of cross-linking between the peroxide and the fibers. This cross-linking process is thought to contribute to the strengthening of the interfacial bond between the peroxide and the fibers, thereby improving their adhesion. Considering the application of peroxide as a thin film on the top surface of each layer, it is expected that the cross-linking process will be more pronounced on the top surface of the fiber rather than the side surface. Therefore, an in-depth investigation of the interfacial bond region, which is expected to be the primary site of action for the reinforcement material, has been conducted (Figure 6. 10e and f). SEM images taken at higher magnification clearly reveal the presence of cross-linked peroxide structures. This observation provides compelling evidence that the adhesion between successive layers is significantly enhanced through cross-linking.

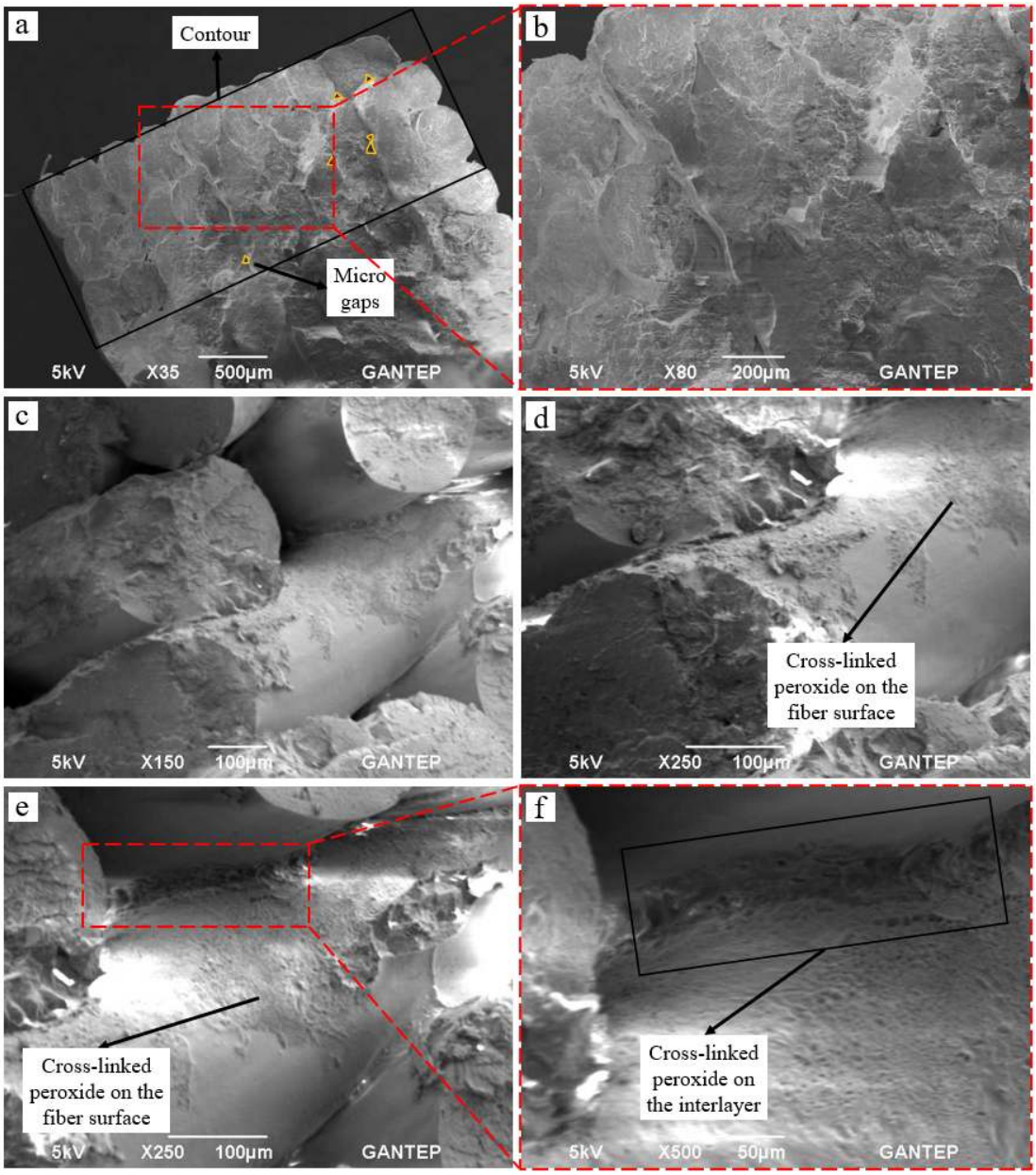

Figure 6. 10 SEM micrographs illustrating the fracture surfaces of peroxide cross-linked PLA composite samples in general

6.4.3 Tensile Test Results

In this section of the thesis, a two-stage experiment was conducted. In the initial stage, TPU and PLA matrix materials were reinforced with benzoyl peroxide (BPO) and polyvinyl acetate (PVA) agents, respectively, and subsequent tensile tests were performed. The tensile test results obtained for these materials are represented in Table 6. 2.

Table 6. 2 Tensile test results obtained from preliminary experiments

	PLA	TPU
	Maximum Tensile Strength (MPa)	Maximum Tensile Strength (MPa)
Without reinforcement	25.5	25.3
Reinforced with PVA	17.8	14.9
Reinforced with BPO	32.5	24.9

When analyzing the results of the experiments using polyvinyl acetate as the agent, it was observed that the tensile strength of the composite materials was lower than that of the respective matrix materials. This suggests that polyvinyl acetate is incapable of forming chemical bonds, specifically cross-linking, with the matrix polymers. The lack of chemical bonding implies that the reinforcement material fails to enhance the mechanical properties of the structure and instead contributes to the formation of voids, resulting in a weakened structure. Consequently, it was concluded that polyvinyl acetate is not a suitable agent material for these matrices, leading to the discontinuation of further investigations involving these materials.

Distinct outcomes were observed after evaluating the samples incorporating benzoyl peroxide as the agent. In the case of the TPU filament, the tensile strength of the specimen without peroxide was slightly higher than that of the TPU/peroxide composite. However, the difference between the two was minimal, with closely aligned results. On the other hand, notable improvements in mechanical properties were achieved for the PLA samples when peroxide was utilized as the agent. Given this considerable enhancement, the decision was made to prioritize PLA/peroxide over TPU/peroxide for further investigations.

The second stage of the study involved the in-situ production of peroxide-reinforced PLA composite samples, with the results of the tensile tests presented in Table 6. 3. Additionally, the tensile test results for PLA samples produced without additives are included in the same table for comparative purposes. Among the PLA filament samples, the lowest measured tensile strength was 23.5 MPa in the two-hour cured sample, while the highest was 25.5 MPa. It was observed that the curing process performed at different holding times did not have a significant impact on the PLA

samples, as the tensile strengths were relatively close to each other. Similarly, no substantial changes were observed in the elongation at the break of the PLA samples.

Table 6. 3 Tensile test results for PLA an PLA/peroxide composite samples

		PLA		PLA/Peroxide Composite	
		Maximum Tensile Strength (MPa)	Elongation at Break (%)	Maximum Tensile Strength (MPa)	Elongation at Break (%)
Curing Time	1 hour	24,1	2,9	19,6	1,7
	2 hours	23,5	2,9	24,8	1,8
	3 hours	25,5	2,7	32,5	2,2

The composite samples exhibited significant changes in strength depending on the peroxide reinforcement and curing time. The lowest measured tensile strength of 19.6 MPa was observed for samples cured for one hour, which is even lower than the tensile strength of unreinforced PLA. This indicates that one hour of curing is insufficient for the peroxide monomers to effectively cross-link with the PLA monomers. FTIR analysis results provided in the previous section confirm the lack of cross-linking in inadequately cured samples. The absence of cross-linking is believed to act as an extraneous component between the two fibers during the bonding of PLA fibers, resulting in the formation of a porosity structure between the polymers and hindering bonding. It is well-established that porosity in 3D-printed samples adversely affects mechanical properties [179], [180].

The tensile strength of peroxide-reinforced PLA samples showed a relative increase when subjected to a curing process of two hours, approaching the levels of PLA samples without the peroxide additive. With longer curing times, it was observed that cross-linking between PLA and peroxide molecules occurred, leading to improved interlayer adhesion. The highest measured tensile strength of 32.5 MPa was achieved with peroxide-reinforced PLA samples cured for three hours. This increase is attributed to the extended curing time and resultant cross-linking between peroxide and PLA polymer molecules. The formation of cross-links between peroxide molecules and PLA repeating units in the three-hour cured samples was confirmed via

the FTIR analysis (Figure 6. 6) and SEM imaging (Figure 6. 10) presented in previous sections.

The stress-strain curves of the PLA and peroxide-reinforced PLA samples with the highest tensile strengths are shown in Figure 6. 11. While the three-hour cured sample exhibited a higher tensile strength than the PLA sample, it showed an approximately 18.5% lower strain at failure. The addition of peroxide resulted in increased brittleness of the sample compared to the PLA. Figure 6. 11b presents the maximum tensile strengths of the samples at different curing times, along with their corresponding standard deviations. The peroxide-reinforced PLA samples cured for three hours, which exhibited the highest stresses, showed lower standard deviations. This indicates that these samples are more stable in terms of mechanical performance.

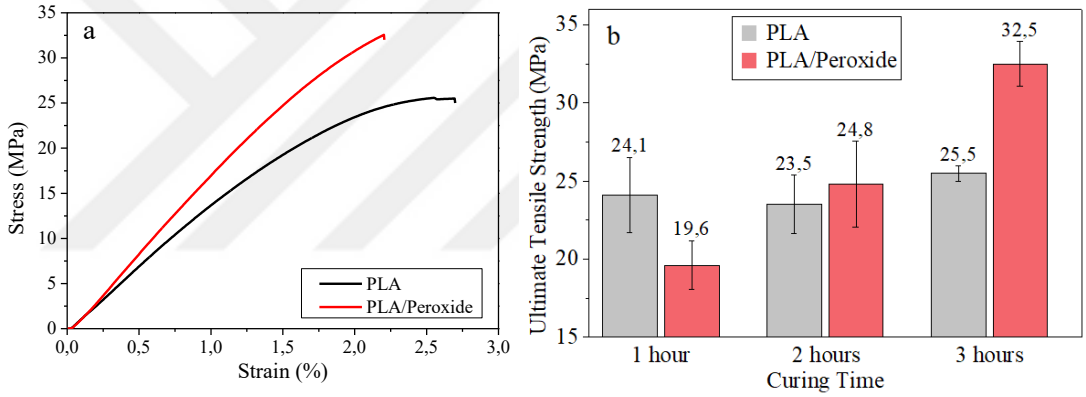

Figure 6. 11 Tensile test results a) stress-strain diagram for the samples with the highest stress, and b) maximum stresses according to curing time

CHAPTER 7

RELATION BETWEEN LAYER ORIENTATION AND MECHANICAL PROPERTIES OF 3D-PRINTED PARTS

7.1 Introduction

This section presents the results of investigations aimed at enhancing the mechanical properties of products produced using FDM 3D printing. The research focused on process parameters to improve the mechanical properties of 3D-printed parts. Initially, the results of the studies conducted to investigate the influence of raster angle on mechanical properties are presented. Subsequently, the results of the study in which the alterations in the mechanical properties of the 3D-printed parts were observed by applying different layer thicknesses are discussed.

7.2 Materials

The current section of the investigation employed three thermoplastic materials, namely polyetherimide (PEI), acrylonitrile butadiene styrene (ABS), and polycarbonate (PC). The selection of these materials was guided by their favorable physical and chemical properties, rendering them well-suited to the intended research objectives. The study aimed to comprehensively examine the mechanical and morphological attributes of these materials and assess their potential for diverse industrial applications. Table 7. 1 presents a comprehensive overview of the working condition of the filaments on the 3D printer used in this study.

7.3 Methods

In this thesis, 3D printers were used namely a Stratasys Fortus 450mc. The Stratasys Fortus 450mc printer is a high-end commercial 3D printer. In order to investigate the effects of 3D printing process parameters on mechanical properties, samples of PC and ABS with varied layer thicknesses and samples of PEI with different raster angles were produced using the Fortus 450mc 3D printer.

Table 7. 1 Details of the working conditions and chemical properties of the 3D printer filaments utilized in this thesis

Printing condition and chemical properties	Filament types		
	PEI	ABS	PC
Layer thickness (µm)	330	**	**
Infill density (%)	100	100	100
Raster angle (°)	*	45/45	45/45

* (0°, 30°, 45°, 60°, 90°) and (0/90°, 30°/-60°, 45°/-45°, 0°/90°/45°/-45°)

** 178 µm, 254 µm and 330 µm

7.3.1 Samples Preparation

Samples of PC, ABS, and PEI were produced using the Fortus 450 mc device, with variations in layer thickness and layer orientation. All samples were produced in the XY (flat) orientation shown in Figure 7. 1. Mechanical properties of PC and ABS samples with layer thicknesses of 178, 254, and 330 µm were analyzed to investigate the effects of layer thickness. Furthermore, the impact of layer orientation on mechanical properties was examined through the production of PEI samples via nine different raster angles. These samples were categorized as single- and multi-oriented. Samples that were built using the same raster angle as the previously deposited layers are referred to as single-oriented samples.

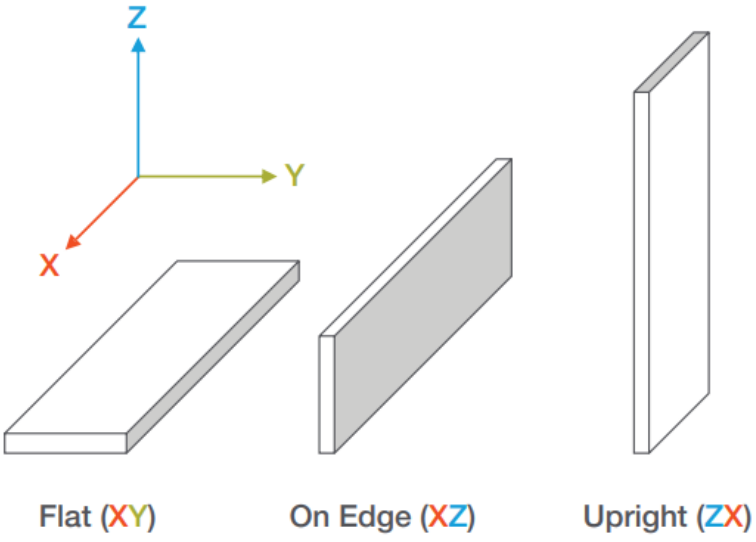

Figure 7. 1 Build orientation of 3D-printed part

Single-oriented samples in 3D printing refer to the specimens that are fabricated with all the fibers aligned in a single direction, along the build direction. These samples are printed with a constant raster angle, which results in unidirectional alignment of the fibers. Single-oriented samples are used to investigate the mechanical properties of the material in the direction of the aligned fibers, which is important in applications where the material is primarily loaded in a single direction. Compared to multi-oriented samples, single-oriented samples have simpler microstructures, which makes it easier to relate the mechanical properties of the material to the microstructure. Multi-oriented samples in 3D printing refer to structures that have been printed with fibers or filaments deposited at different angles in three-dimensional space. By controlling the orientation of the fibers in each layer of the print, the resulting structure can have anisotropic mechanical properties, which means that the strength and stiffness of the material are different in different directions.

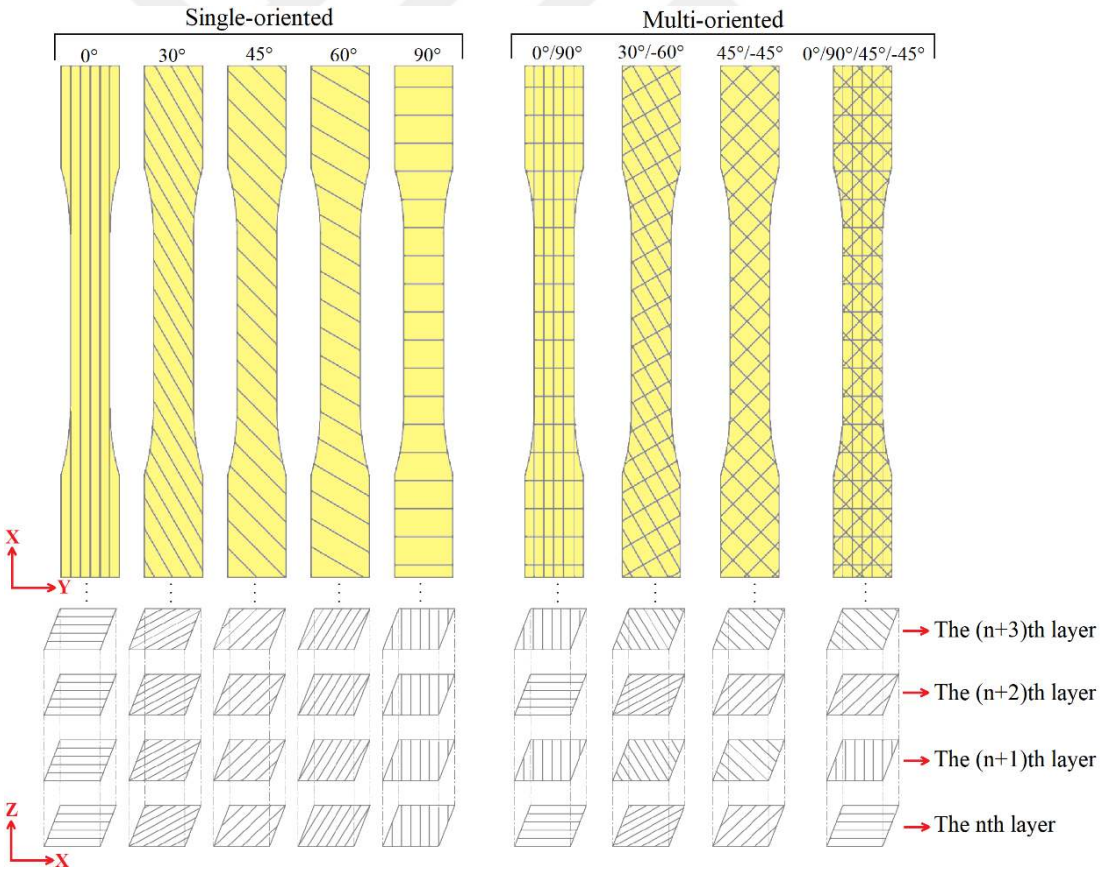

Figure 7. 2 Schematic representation of single- and multi-oriented specimens showing the raster angles

For this study, single-oriented samples were produced with raster angles of 0°, 30°, 45°, 60°, and 90°. Conversely, specimens that were produced using different raster angles from the previously deposited layer are known as multi-oriented samples. In this study, multi-oriented samples were fabricated with raster angles of 0°/90°, 30°/−60°, 45°/−45°, and 0°/90°/45°/−45°. The raster angles of single- and multi-oriented samples are shown in Figure 7. 2. All other parameters such as fill rate, printing velocity, air gap, raster width, and fill pattern were kept constant throughout the fabrication process.

7.3.2 Characterization and Testing

The tensile test of samples was conducted using a Shimadzu AGX universal testing device (50 kN load capacity). The standard tension tests were carried out in accordance with ASTM D638 with a strain rate (ε̇) of 5 mm/min [173]. Five identical samples were produced for each test condition, and the test values were evaluated by averaging the results of five successive measurements. The bending tests for the specimens were accomplished using the same device, following the procedure outlined in ASTM D790-17 [181]. A symmetric three-point bending test on a span of 30 mm was performed at a speed of 1.56 mm/sec. The hardness test experiments were carried out using a portable BAREISS HPE II D-type shore hardness tester, following the ASTM D2240-15 standard [182]. Fifteen different locations were tested for each sample, and their averages were calculated. All tests were performed under room conditions at constant temperature and humidity. The Figure 7. 3 presents the dimensions of the tensile and bending test samples prepared in accordance with the ASTM standards.

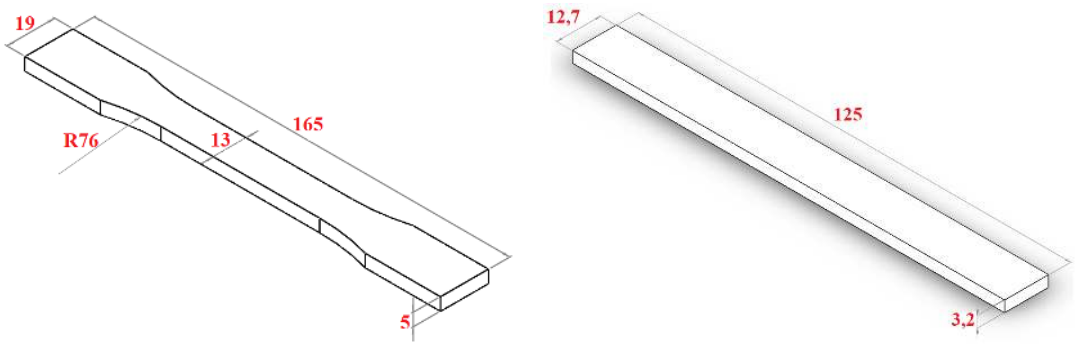

Figure 7. 3 Shape and dimensions of specimens for a) tensile test, and b) bending test

The fractured surfaces of the 3D-printed specimens were observed using a Zeiss Gemini 300 SEM to determine the fracture effect on fibers. Prior to SEM analysis, the specimens were coated with a thin layer of palladium/gold.

7.4 Result and Discussion

Tensile tests of the samples produced with PEI filament in different layer orientations were evaluated. The SEM analysis was then assessed for the tensile fracture surface of the specimens produced with PEI filament, which has different raster angles. Subsequently, additional mechanical properties such as bending strength and hardness were examined. Also, the tensile test results for samples printed with PC filament in various layer thicknesses were assessed. The objective of this investigation was to explore the relationship between layer thickness and the mechanical properties of 3D-printed PC samples.

7.4.1 Layer Orientation

7.4.1.1 Tensile Test Results

The stress-strain graphs for the tensile tests of the PEI specimens fabricated in single-oriented forms are depicted in Figure 7. 4, accompanied by a schematic representation of the test specimen on the same scale. This schematic representation indicates the aligned fibers and the direction of the applied tensile force on the respective sample. In addition, this figure presents the tensile test results for five distinct samples fabricated at each raster angle, along with the tensile fracture images of the specimens.

The tensile test results indicates that the strength of the single-oriented specimens decreased with increasing raster angle. This decrease in strength can be attributed to the relatively weak interfacial bonding between the successive fibers. The specimen fabricated with a 0° raster angle exhibited the highest tensile strength due to the parallel alignment of the direction of the applied tensile force, and that of each deposited individual fiber, as depicted in Figure 7. 4a. In the specimen with a 0° raster angle, the applied tensile force acts on each deposited fiber rather than on the interfacial bonding. However, as the raster angle approaches to 90°, the direction of the applied tensile force intersects with the orientation of the deposited fibers, as shown in Figure 7. 4b, c, and d. Therefore, the tensile force acts on both the deposited materials and the interfacial bonding in samples with a raster angle approaching 90°. The interfacial

bonding between the deposited fibers is insufficient to withstand the applied tensile loading. Consequently, the samples with 30°, 45°, and 60° raster angles exhibit relatively reduced tensile strength due to reduced resistance of the interfacial bond against the applied tensile load.

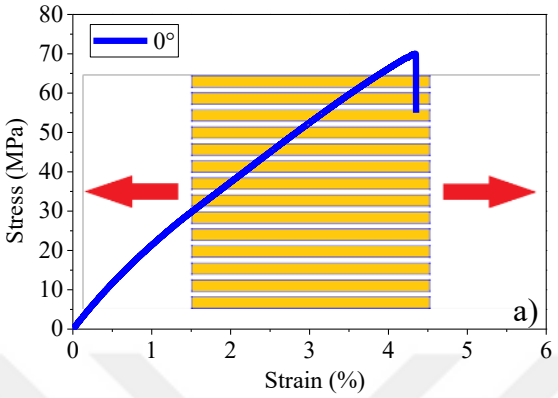

Raster angle	Max. tensile strength (MPa)		Strain (%)	
		Mean		Mean
0°	71.9	72.3	4.6	4.5
	64.3		4.1	
	72.2		4.1	
	74.6		5.0	
	79.8		4.8	

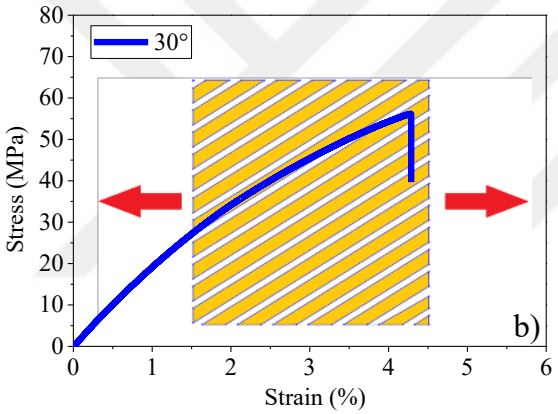

Raster angle	Max. tensile strength (MPa)		Strain (%)	
		Mean		Mean
30°	53.8	56.2	4.0	4.3
	52.8		4.1	
	60.4		4.8	
	52.4		3.7	
	61.7		4.9	

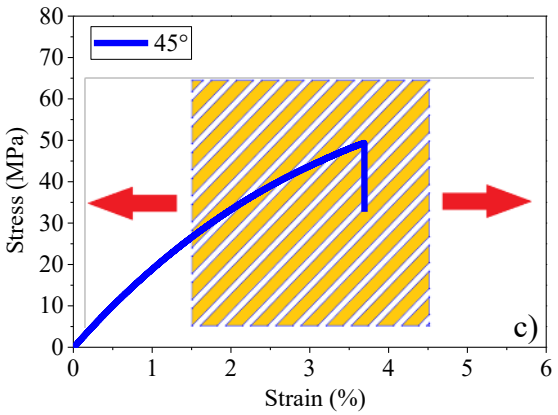

Raster angle	Max. tensile strength (MPa)		Strain (%)	
		Mean		Mean
45°	49.7	49.3	3.9	3.7
	45.8		3.5	
	51.3		4.2	
	45.2		3.5	
	54.6		3.7	

Figure 7.4 The tensile test result, stress-strain graph, and tensile fracture representation of single-oriented specimens printed with raster angles of a) 0°, b) 30°, c) 45°, d) 60°, and e) 90° (continue)

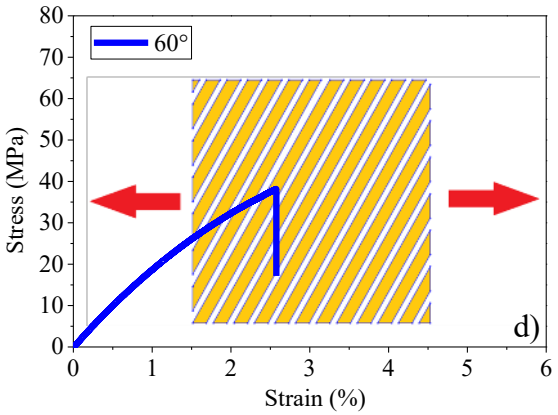

Raster angle	Max. tensile strength (MPa)		Strain (%)	
		Mean		Mean
60°	36.8	38.2	2.4	2.6
	43.5		3.1	
	35.7		2.4	
	38.2		2.6	
	36.8		2.6	

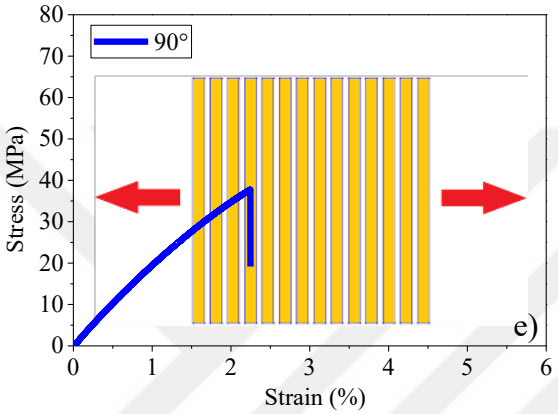

Raster angle	Max. tensile strength (MPa)		Strain (%)	
		Mean		Mean
90°	36.3	37.8	2.2	2.2
	41.6		2.3	
	36.4		2.2	
	37.1		2.2	
	37.5		2.3	

Figure 7. 4 The tensile test result, stress-strain graph, and tensile fracture representation of single-oriented specimens printed with raster angles of a) 0°, b) 30°, c) 45°, d) 60°, and e) 90°

The tensile strengths of PEI samples produced using 30°, 45°, and 60° raster angles were found to lie between those of the 0° and 90° samples. In the specimen with a 90° raster angle, the tensile force acted perpendicular to the direction of each deposited fiber, as demonstrated in Figure 7. 4e. This indicates that the tensile loading was exerted directly on the interfacial bonds. Hence, the tensile characteristics of the sample fabricated using a 90° raster angle were limited by the strength of the interfacial bonding between the deposited fibers. Thus, the sample with the 90° raster angle exhibited the lowest tensile strength of all samples. Figure 7. 4 illustrates that the elongation at break of the specimens was influenced by the raster angle. Specifically, the elongation at break exhibited a similar trend to that of tensile strength, decreasing as the raster angle increased for the single-oriented samples.

The stress-strain curves of the PEI specimens fabricated in multi-oriented forms are shown in Figure 7. 5, along with a schematic representation of the test specimen to scale, depicting the aligned fibers and the direction of the applied tensile force. The figure also displays the tensile test results for five samples produced at each raster angle, as well as the corresponding fracture images.

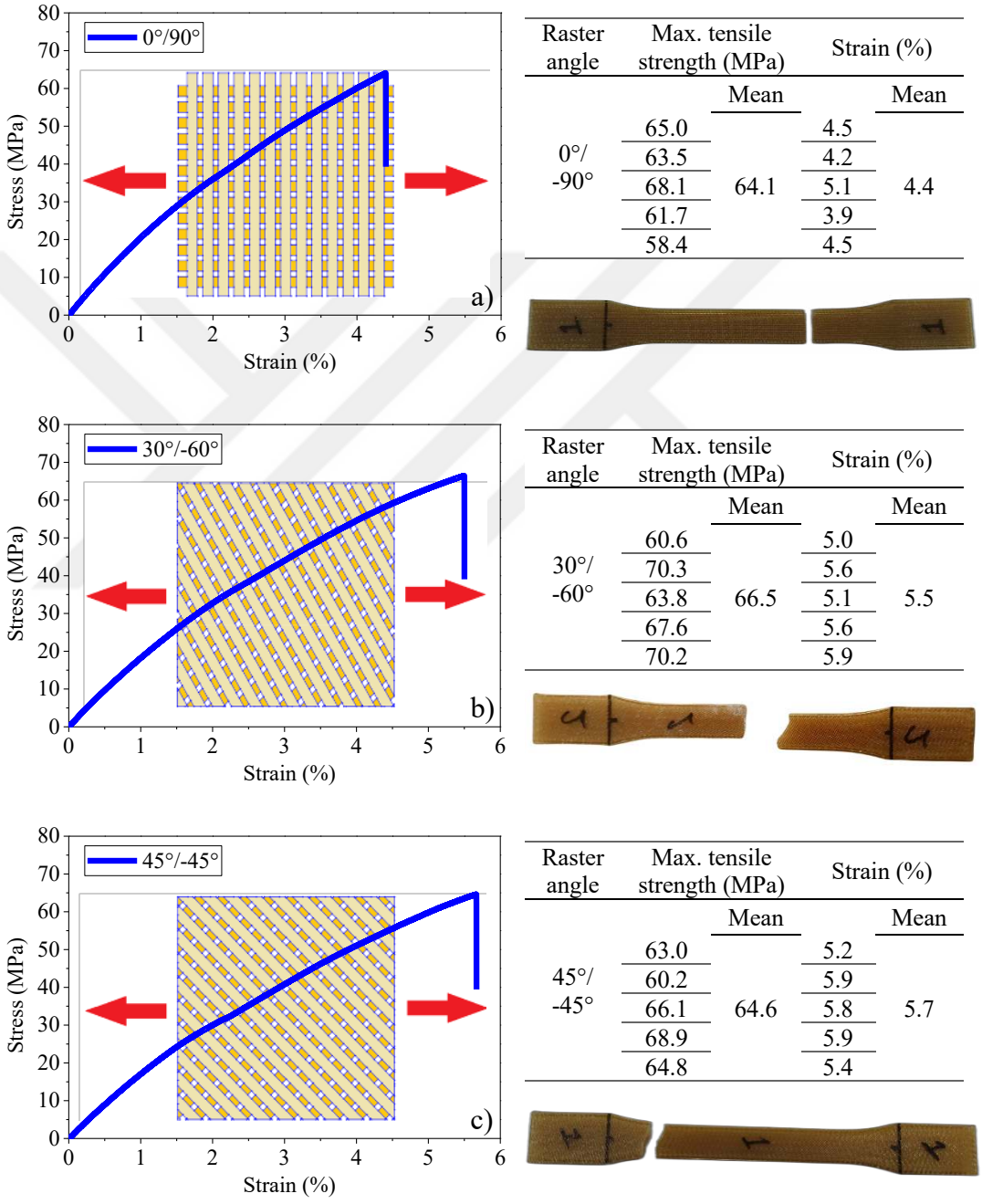

Raster angle	Max. tensile strength (MPa)	Mean	Strain (%)	Mean
0°/ -90°	65.0	64.1	4.5	4.4
	63.5		4.2	
	68.1		5.1	
	61.7		3.9	
	58.4		4.5	

Raster angle	Max. tensile strength (MPa)	Mean	Strain (%)	Mean
30°/ -60°	60.6	66.5	5.0	5.5
	70.3		5.6	
	63.8		5.1	
	67.6		5.6	
	70.2		5.9	

Raster angle	Max. tensile strength (MPa)	Mean	Strain (%)	Mean
45°/ -45°	63.0	64.6	5.2	5.7
	60.2		5.9	
	66.1		5.8	
	68.9		5.9	
	64.8		5.4	

Figure 7.5 The tensile test result, stress-strain graph, and tensile fracture representation of multi-oriented specimens printed with raster angles of a) 0°/90°, b) 30°/-60°, c) 45°/-45°, and d) 0°/90°/45°/-45° (continue)

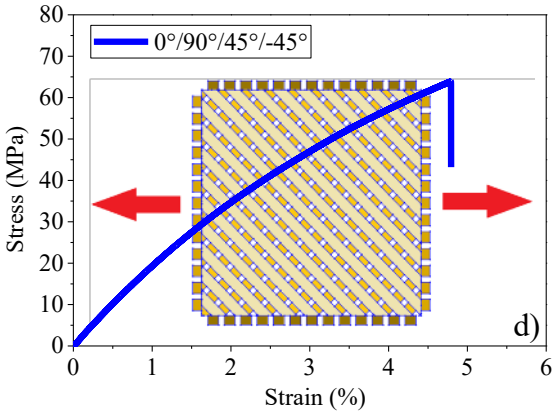

Raster angle	Max. tensile strength (MPa)		Strain (%)	
		Mean		Mean
0°/ -90°/ 45°/ -45°	68.2	63.9	5.5	4.8
	63.9		4.1	
	63.4		4.6	
	62.2		4.5	
	64.6		5.4	

Figure 7. 5 The tensile test result, stress-strain graph, and tensile fracture representation of multi-oriented specimens printed with raster angles of a) 0°/90°, b) 30°/-60°, c) 45°/-45°, and d) 0°/90°/45°/-45°

The experimental results for the multi-oriented samples indicate that there is no significant difference in the tensile strength among specimens produced with different raster angles. Similar strengths were observed among the multi-oriented samples fabricated with four different raster angles. However, when comparing the multi-oriented samples, the samples fabricated with raster angles between 30°/-60° exhibit relatively higher tensile strength, as seen in Figure 7. 5b. In multi-oriented manufacturing, the overlapping of successive layers at right angles provides a beneficial effect in terms of tensile strength by acting as a barrier against the applied tensile force and increasing the overall resistance to fracture. Therefore, the resulting tensile strength can be deemed satisfactory.

Figure 7. 6 also illustrates that elongation at break was dependent on the configuration of the raster angles. As observed in the tensile test, an acceptable enhancement is observed in the elongation at break of multi-oriented samples. The observed improvement in elongation at break for multi-oriented samples can be attributed to the formation of barriers by consecutive orthogonal fibers against the applied tensile force, similar to the results observed for tensile strength. It can be concluded that the multi-oriented samples have reached a standard in terms of maximum tensile strength and elongation at break.

Comparison of the tensile test results for the single- and multi-oriented samples reveals that the latter generally exhibited higher tensile strengths than the single-oriented

models. This can be attributed to the fact that the multi-oriented models have a higher degree of structural complexity, with successive layers of fibers oriented in different directions providing increased resistance to fracture. Additionally, the multi-oriented samples showed less variation in tensile strength with raster angles than the single-oriented samples, indicating a more consistent mechanical performance. Furthermore, the results show that the multi-oriented samples consistently exhibited higher elongation at break compared to all single-oriented samples. Also, the multi-oriented production method achieved a more uniform standard in terms of elongation at break. These findings can be attributed to the perpendicular layer configuration of the multi-oriented samples, which creates a barrier effect that enhances their resistance to fracture under tensile loading.

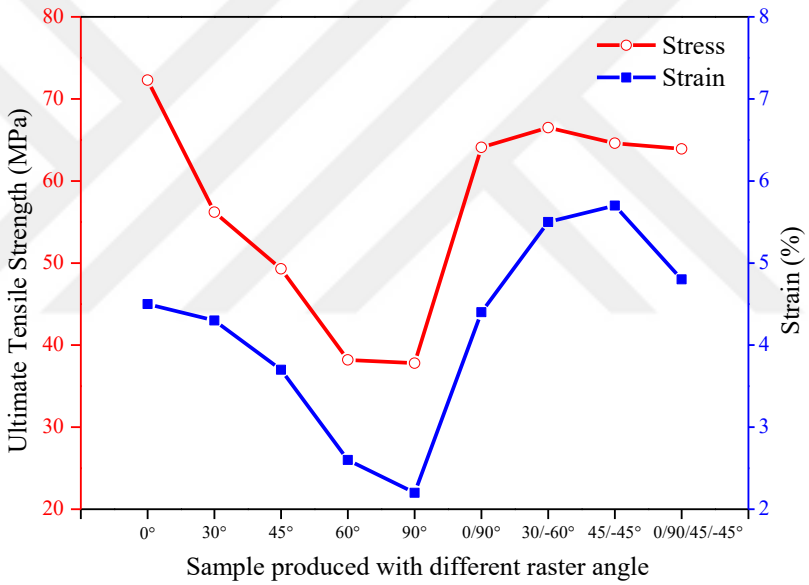

Figure 7. 6 Comparison of tensile test results for singles and multi-oriented samples

On the other hand, the single-oriented samples, with the exception of the sample with a raster angle of 0°, exhibited lower tensile strengths due to the relatively poor interfacial adhesion within their fiber arrangement.

The results of the tensile test indicated a significant correlation between the direction of fiber deposition and the direction of the applied tensile force. The correlation is illustrated in Figure 7. 7, which depicts the relationship between the direction of fiber deposition and the applied tensile force direction. If the deposition direction is aligned with the applied direction of force, the resulting product has higher strength in that

direction. However, if the deposition direction is perpendicular or at an angle to the direction of applied force, the resulting product has lower strength in that direction.

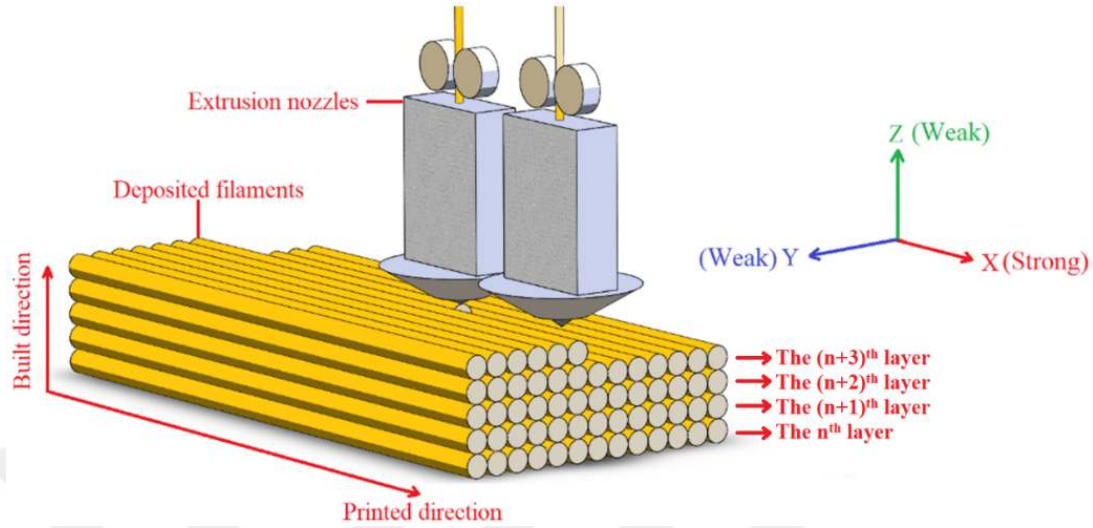

Figure 7. 7 Schematic illustration of the correlation between the direction of fiber deposition and the direction of applied tensile force in the context of 3D printing

7.4.1.2 Fracture Surface

SEM analysis was conducted for all 3D-printed specimens produced with varying raster angles to gain a deeper understanding of the fracture mechanism. Fracture analysis of samples was typically performed to better understand the failure mechanism and properties of the material. By analyzing the fracture surface, information was obtained about the type of failure that occurred in interfacial bonding, the location of the initiation and propagation of the crack, and the overall microstructure of the material.

Figure 7. 8 shows the SEM image capturing the fracture surface of the PEI specimens obtained from the tensile tests and the defects observed on this surface. The SEM micrographs of the tensile specimens displayed two distinct types of failure mode, namely interfacial bond failure, and fiber breakage (rupture of the fiber surface). Interfacial bond failure is a phenomenon in which the bond between two consecutive fibers is not sufficiently strong to withstand the applied load, resulting in tearing or separation between the fibers. Some regions exhibited weak adhesion with noticeable interfacial tearing, while other regions displayed a light fiber-tear failure resembling a porous structure, as observed in the microstructural analysis.

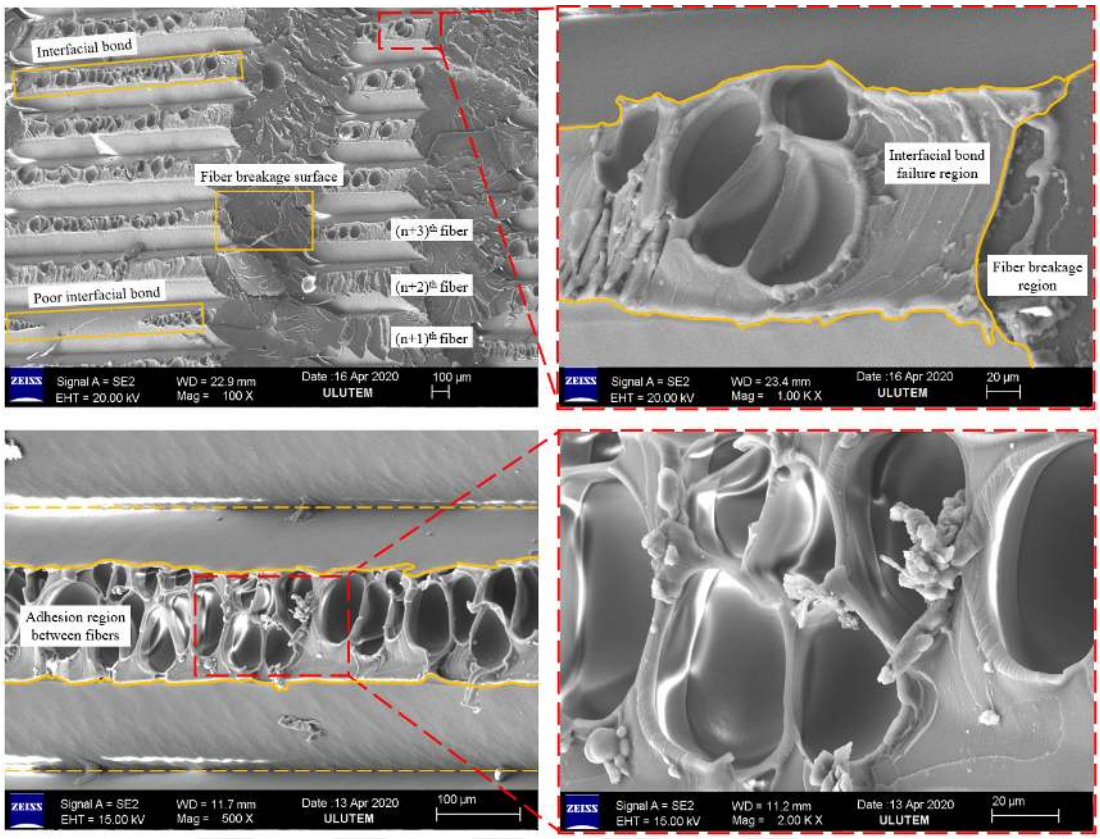

Figure 7. 8 SEM micrographs of failure types

On examination of the fracture surfaces of the single-oriented production samples, as shown in Figure 7. 9a to e, two distinct failure behaviors, namely bond failure and fiber breakage regions, are seen. The fracture surface of the sample printed with a 0° raster angle (Figure 7. 9) exhibits a uniform and smooth appearance, indicative of a brittle fracture. This suggests that the predominant failure mode occurs at the fiber surfaces rather than at the interface, as the tensile force is primarily exerted along the longitudinal direction of the deposited fibers. Consequently, this phenomenon elucidates the rationale behind the sample printed at a 0° raster angle exhibiting the highest tensile strength. Moreover, it can be seen that the fractures occur largely at the interfacial bonds when the raster angle is increased, as seen in Figure 7. 9b, c, d, and e. As the raster angle was increased, the failures tended to occur towards the interface bonds rather than via fiber breakage (rupture of the fiber surface). This observation provides an explanation for the decrease in tensile strength of PEI with increasing raster angle in 3D-printed specimens. The fracture of the PEI specimen fabricated with a 90° raster angle occurred solely at the interfacial bonds, as depicted in Figure 7. 9e. Breaking fibers from the interfacial bonding zone is easier than breakage through

surface rupture. This elucidates why the sample produced with a 90° raster angle exhibited the worst mechanical properties among the unidirectional production samples.

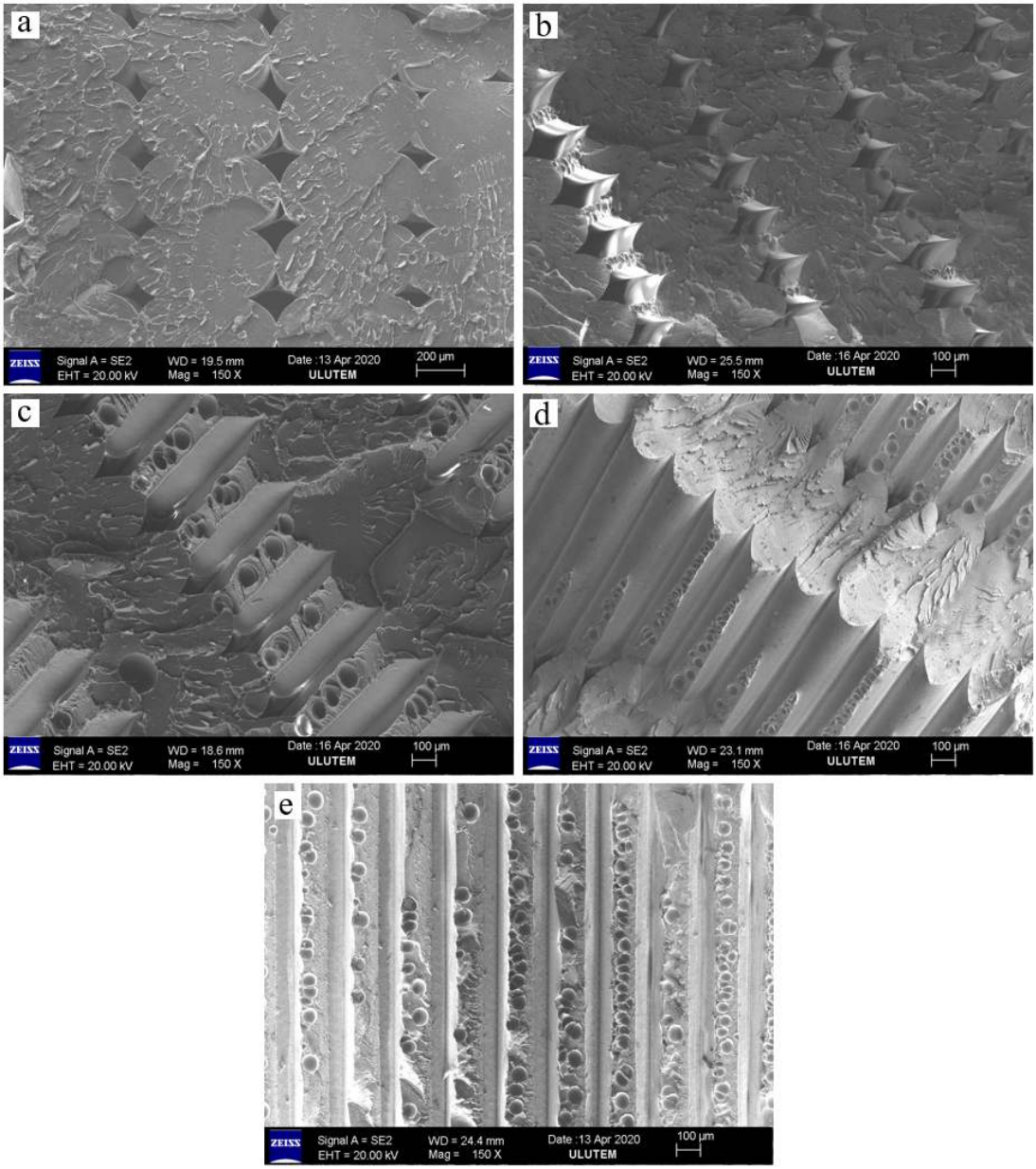

Figure 7. 9 SEM image capturing the fracture surface of single-oriented specimens produced with raster angles of a) 0°, b) 30°, c) 45°, d) 60°, and e) 90°

Figure 7. 10 displays microscopic images capturing the fracture surface of the multi-oriented specimens subsequent to the completion of the tensile test. In multi-oriented specimens (Figure 7. 10a, b, c, and d), while the fibers in one layer are directed to break from the interface, the fibers in the lower and upper layers that are orthogonal to

those in the middle layer create a barrier to breaking from interfacial bonds and force the breaks to occur at the fiber surface. Consequently, this leads to an enhancement in the strength of the multi-oriented production samples and accounts for the observed augmentation in their strengths, attributed to a higher fiber fracture compared to single-oriented samples (except for single-oriented sample produced with the 0° raster angle). However, despite the exertion of the upper and lower layers in inducing surface fractures in the middle layer, the presence of interface breaks in multiple regions is evident. This observation elucidates the underlying reason behind the inability to achieve strengths comparable to those obtained from samples produced with a raster angle of 0°.

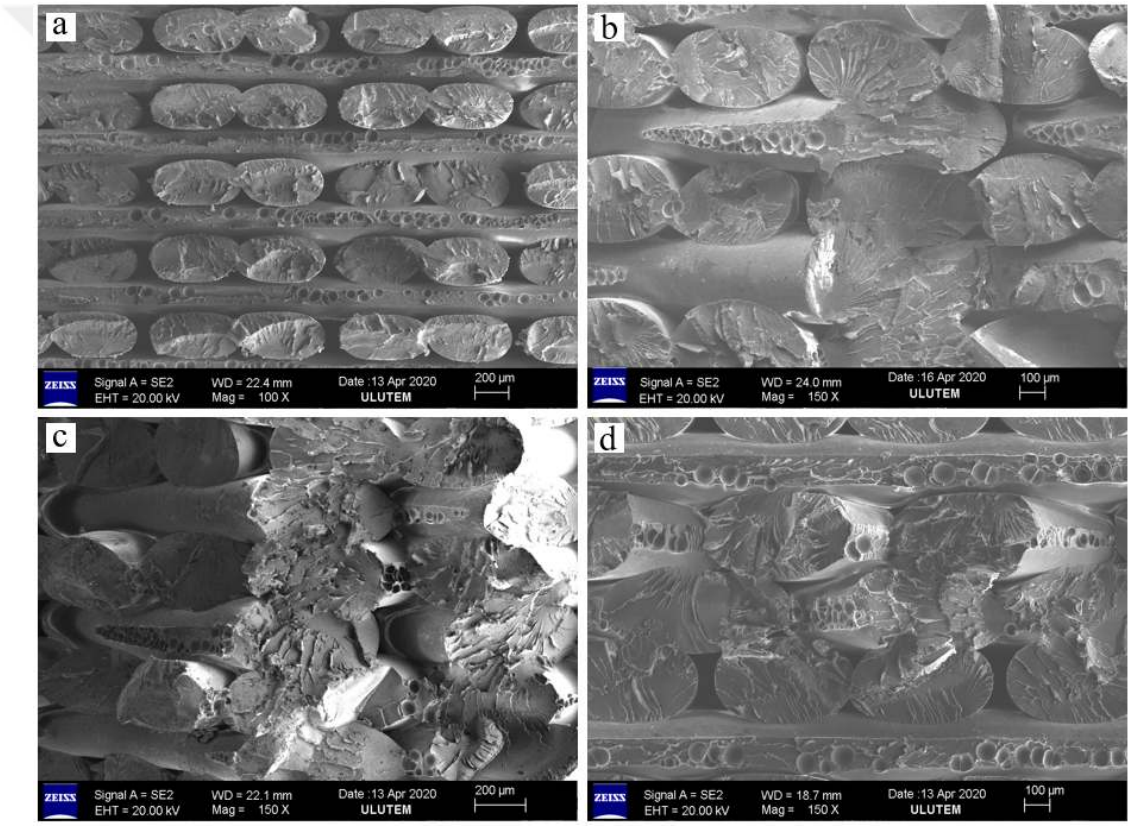

Figure 7. 10 SEM image capturing the fracture surface of multi-oriented specimens produced with raster angles of a) 0°/90°, b) 30°/-60°, c) 45°/-45°, and d) 0°/90°/45°/-45°

The analysis of tensile test results and examination of fracture surfaces provide conclusive evidence that 3D-printed components exhibit enhanced resistance to tensile loading when the direction of filament deposition aligns with the applied tensile load.

Alignment of the load parallel to the fiber orientation leads to increased strength, as the fibers predominantly bear the load, enabling efficient stress transfer along their length and resulting in improved mechanical performance. Furthermore, a notable decrease in the tensile strength of the 3D-printed part was observed when the load directly influenced the interlayer bonds. This observation underscores the significant influence of interfacial phenomena on the strength characteristics of 3D-printed components.

7.4.1.3 Bending Test Results

Figure 7. 11 and Figure 7. 12 illustrate the variations in applied maximum force and displacement during the bending test, respectively, as a function of the raster angle. The observed trend aligns with the findings from the tensile test, wherein the specimen was fabricated with a 0° raster angle, exhibited the highest bending strength. It was established that, in single-oriented examples, the maximum bending force and displacement decreased as the raster angle increased, as depicted in Figure 7. 11 and Figure 7. 12.

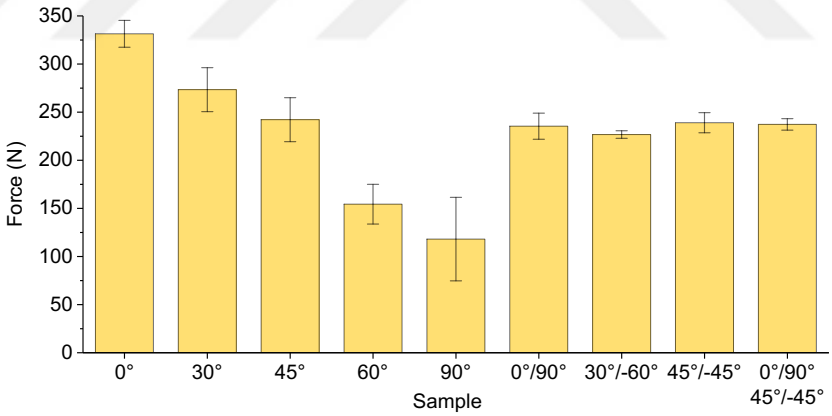

Figure 7. 11 Variation of maximum applied force with respect to raster angle in the bending test of 3D-printed samples

The specimen fabricated using a raster angle of 0° exhibited a higher resistance to bending forces because the applied force could predominantly act on each deposited filament rather than on the interlayer bonding interactions. The filaments demonstrate superior resistance to bending loads in comparison to interlayer bonds. However, as the raster angle of the part increased, the applied bending force increasingly affected the intermediate bonds. These intermediate bonds exhibited a lower resistance to

bending; for this reason, the lowest bending strength was observed in the specimen created with a 90° raster angle.

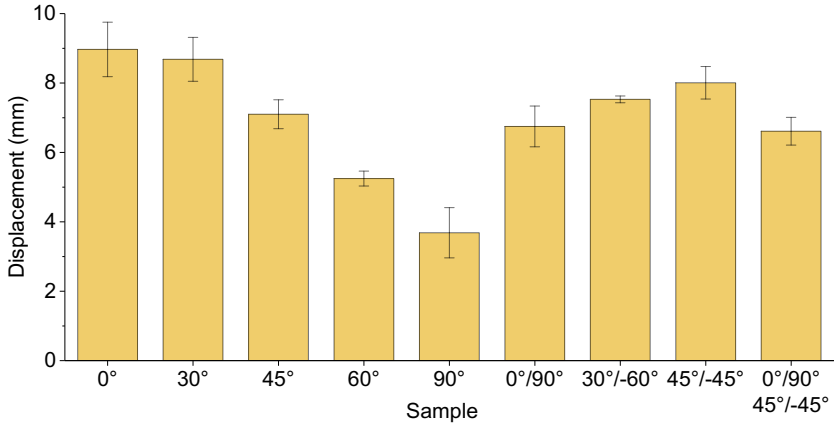

Figure 7. 12 Variation of displacement with respect to raster angle in the bending test of 3D-printed samples

A comparative analysis was conducted between the bending test results of single- and multi-oriented specimens; the bending resistivity of multi-oriented samples was observed to improve slightly compared to the specimens built with 60° and 90° raster angles. However, it was noted that the bending resistivity of the multi-oriented samples remained lower than that of samples fabricated with 0°, 30°, and 45° raster angles. This can be attributed to the load exerted on the outermost layer, which exerts pressure on the underlying interfacial bonding region. The interfacial bonds, subjected to the applied forces during the bending test, represent the more vulnerable regions within the structure. It was observed that crack initiation occurred specifically at these weak points along the direction of raster deposition for all layers [183]. In the case of multi-oriented examples, it was hypothesized that the flexural strengths were comparatively improved due to the alignment of these weak interlayer bonds perpendicular to the deposited filaments in the lower and upper layers. Because these fibers in the lower and upper layers formed a barrier against cracking, the multi-oriented samples saw a slight enhancement to fracture resistance. Although the deposited filaments in the lower and upper layers formed a barrier against fracture, they had low bending resistance to the specimen constructed with a 0° raster angle since the applied force primarily influenced the interfaces.

Furthermore, it was seen that the maximum forces observed in each multi-oriented specimen did not exhibit significant differences because the higher maximum force of a given angle could compensate for a lower one. The standard deviation of maximum force and displacement in the multi-oriented examples was generally lower in magnitude than that of the single-oriented examples. This observation suggests that the PEI samples manufactured through multi-oriented production exhibited greater stability than those produced through single-oriented production. This trend is visually represented by the narrower error bars depicted in the columns in Figure 7. 11 and Figure 7. 12.

Figure 7. 13 presents the images of the fracture surfaces that emerged after subjecting the specimens to the bending test. The findings indicate that failure initiation was predominantly at the interlayer bond interface in the case of single-oriented specimens. Upon close examination of the fracture surfaces, it became evident that failures primarily manifested at the interfaces between adjacent layers rather than within the deposited filaments. Moreover, a notable observation was made regarding the sample fabricated with a raster angle of 0°, which displayed the highest bending strength. Remarkably, this specimen demonstrated outstanding resistance to fracture, as no instances of such failure were observed.

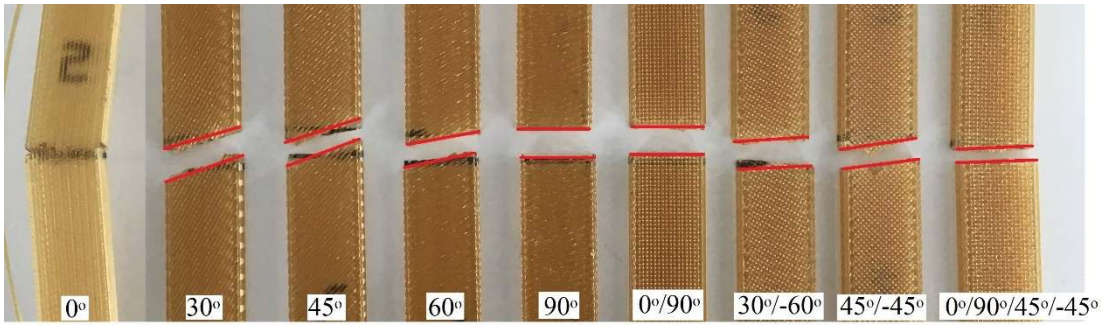

Figure 7. 13 Fracture surface images in PEI specimens with various raster angles following the bending test

As indicated in the materials and methods section, five samples were prepared for each bending test, and none of the PEI specimens printed with a 0° raster angle experienced any breakage. As the raster angle increased in single-oriented samples, a corresponding decrease in the fracture angle was observed. This further confirms that failure predominantly occurs at the interface bonds within the material.

7.4.1.4 Hardness Test Results

Hardness is commonly defined as the intrinsic ability of a material to resist penetration by a rigid indenter, and it is quantified by measuring the indentation depth made by such an indenter on the material's surface. The Shore Test method is widely employed to measure the plastic hardness of materials [184]. Figure 7. 14 illustrates the alteration in hardness resulting from the variation in measurement points, while Table 7. 2 and Table 7. 3 present the average hardnesses of the single- and multi-oriented samples, respectively.

Table 7. 2 Hardness test results for single-oriented specimens

	Single-oriented samples				
Sample raster angle	0°	30°	45°	60°	90°
Shore Hardness	71.0	71.8	73.0	73.3	72.2

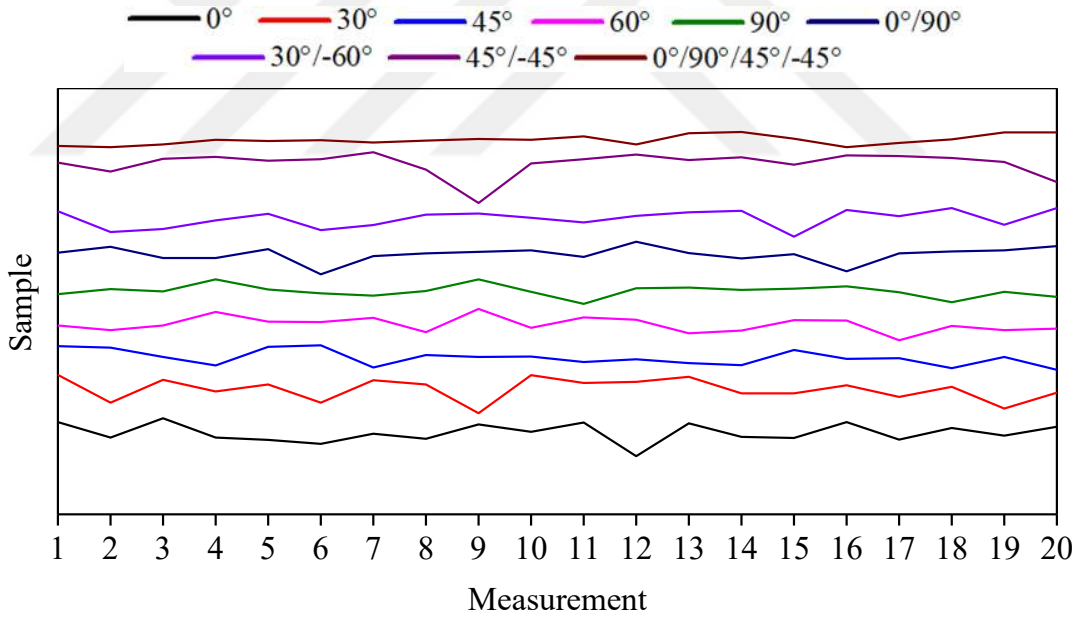

Figure 7. 14 Variation in hardness across multiple measurement points on 3D-printed PEI specimens fabricated with various raster angles

Table 7. 3 Hardness test results for multi-oriented specimens

	Multi-oriented samples			
Sample raster angle	0°/90°	30°/-60°	45°/-45°	0°/90°/45°/-45°
Shore Hardness	72.5	72.1	71.0	72.6

In the course of penetration by the rigid indenter, each layer beneath the surface of the 3D-printed sample is subjected to an indentation force along with an indentation depth. When subjected to this force, the distinct alignment of the preceding layer can induce variations in the hardness measurements due to alterations in the micro gaps within the material caused by the differing layer alignment. If the indenter consistently intersects these micro-gaps during the measurement process, this can also lead to a reduction in hardness. Consequently, variations in hardness were observed among PEI specimens with different raster angles. However, no substantial discernible difference was found with these changes in hardness.

Figure 7. 15 presents a representative SEM image of a multi-oriented sample displaying micro gap formation within the interfacial region. The size and intensity of these micro gaps can vary based on the alignment of fibers within the specimens, potentially resulting in minor disparities in the hardness of the tested sample, as noted in reference [185]. It may be noted in Figure 7. 15 that the hardness fluctuated according to the measured region. Certain measurements obtained from different locations on the sample exhibit a sudden reduction in hardness, which can be attributed at these specific points to the interlayer bonding, as the resistance of the interfacial bonds against the applied indentation force is comparatively lower than that of the bulk filament material. The filament material itself, when not bonded, tends to exhibit higher resistance to indentation.

When analyzing the sample produced with a raster angle sequence of 0°/90°/45°/-45° in Figure 7. 14, the variation in hardness observed appears to be minimal, with a nearly linear trend. In this example, the absence of abrupt drops in hardness can be attributed to the stacking of layers at four distinct angles, resulting in a more complex alignment of fibers. Consequently, asymmetric layer sequences are formed, as opposed to the isotropic repetition of layers. This configuration poses challenges in aligning microgaps across successive layers and is believed to contribute to a relatively lower occurrence of microvoid structures exhibiting the same vertical alignment (sequential microvoid formation). Hence, the hardness graph does not exhibit pronounced fluctuations or sudden drops but rather maintains a relatively constant and closely distributed range of hardnesses across different measurement points. This observation supports the notion that fiber orientation is one of the parameters that influences the

hardness characteristics of the 3D-printed part. No significant variation was detected in the hardnesses when comparing samples with varying layer orientations. However, this study demonstrated the potential to mitigate the reduction in hardness resulting from microgaps within different regions of the products' structures. Consequently, this highlights the feasibility of achieving a more uniform hardness distribution across the materials' surfaces.

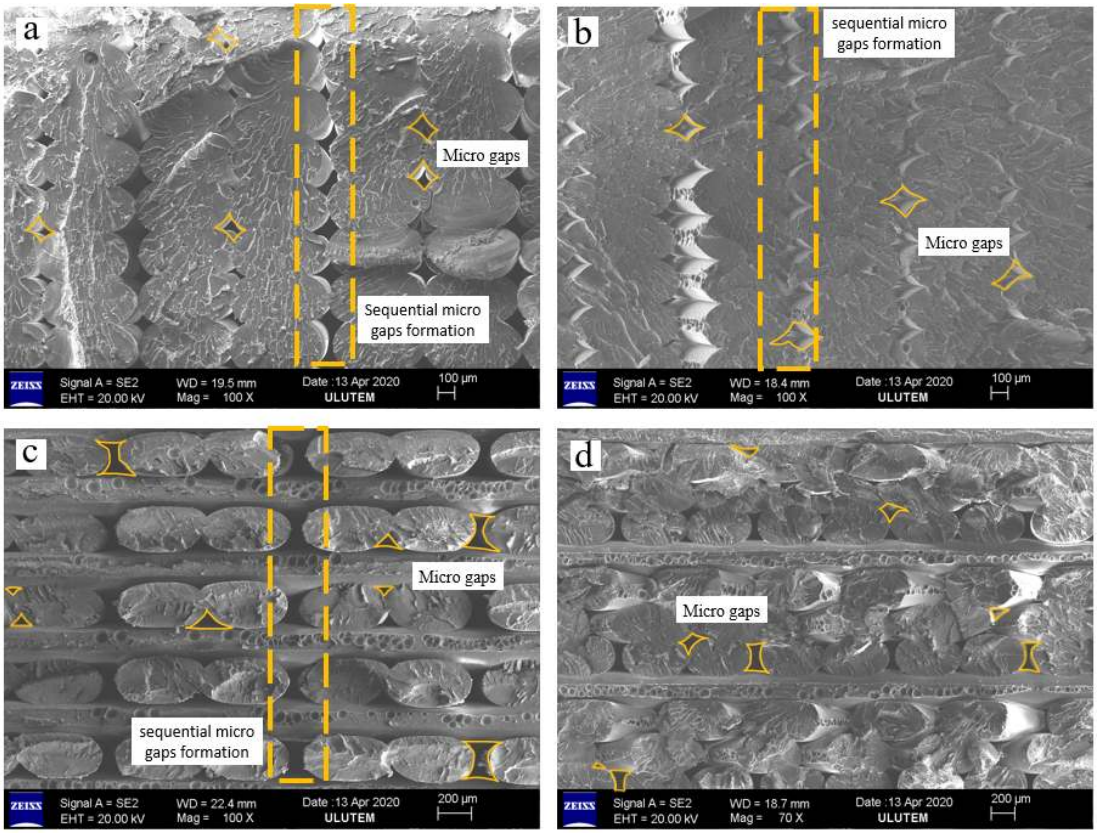

Figure 7. 15 A representative SEM image showing microgaps caused by layer alignments a) 0°, b) 30°, c) 0°/90°/, and d) 0°/90°/45°/-45°

7.4.2 Layer Thickness

The stress-strain graphs obtained from the tensile tests of PC and ABS samples produced in three different layer thicknesses are shown in Figure 7. 16 and Figure 7. 17, respectively. The layer thickness in 3D printing is directly correlated with the required number of layers to construct a part, consequently impacting the printing time. As the layer thickness increases, the manufacturing costs decrease.

Experimental findings demonstrated that increasing the layer thickness from 178 µm to 254 µm resulted in an enhancement in the tensile strength of the PC samples. It can be said that a positive correlation was observed between the strength and layer

thickness. As reported by Sood et al. [186], this can be attributed to the reduction in the number of layers required to achieve a given total thickness as the layer thickness increases. This decrease in layer count leads to minimized distortion effects and, consequently, an enhancement in strength [187]. However, when the layer thickness was increased from 254 µm to 330 µm, there was not much change in the tensile strength of the PC sample. Furthermore, the measured fracture elongation at break for PC samples with varying layer thicknesses exhibited minimal variation, suggesting that the layer thickness had a limited impact on this particular mechanical property.

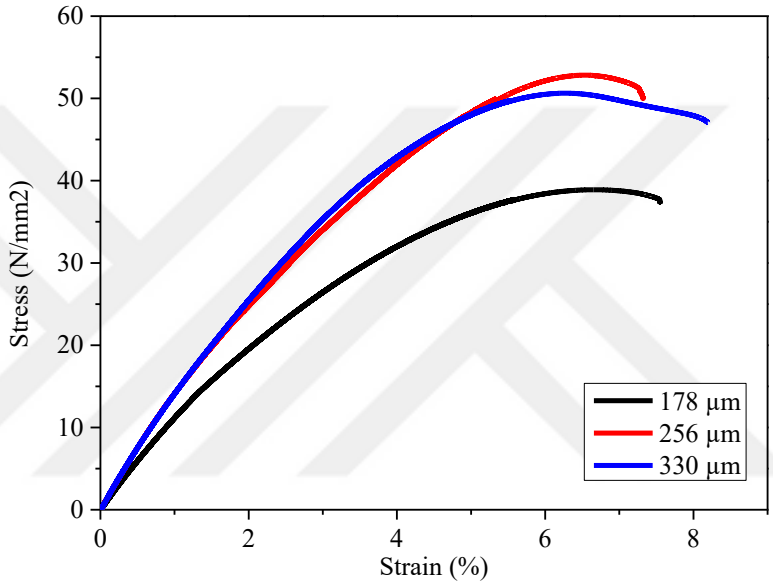

Figure 7. 16 Stress-strain curves of 3D-printed PC with various layer thickness

When the tensile test results for the ABS samples produced in different layer thicknesses are examined, it can be said that a similar result is obtained to that of the PC samples. Primarily, the tensile test values of all ABS samples exhibited a high degree of proximity to one another. Although no substantial disparities were observed among them, the lowest maximum strength was identified in the sample with the lowest layer thickness, mirroring the trend observed in the PC samples. In addition, an increase in strength was observed relative to the layer thickness, indicating that higher layer thicknesses contributed to increased strength. This effect can be stated by considering that with increased layer thickness, fewer layers were needed for the final shape of the product and, therefore, the number of layer bonds was reduced, and the tensile strength of the samples accordingly increased. As stated by Rodriguez et

al.[188], a progressive increase in layer thickness facilitates the flow of semi-melted material within the expanded interfiber spaces, thereby leading to a corresponding enhancement in strength.

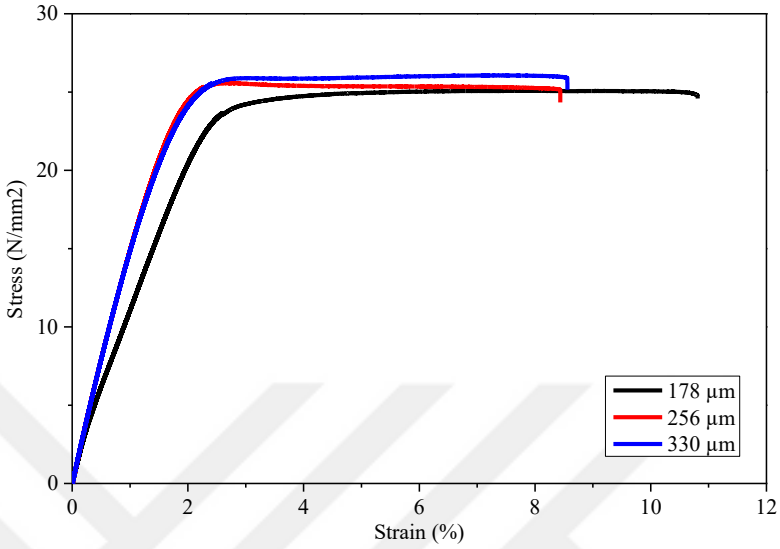

Figure 7. 17 Stress-strain curves of 3D-printed ABS with various layer thickness

CHAPTER 8

RELATION BETWEEN ANNEALING PROCESS AND MECHANICAL PROPERTIES OF 3D-PRINTED PARTS

8.1 Introduction

This section presents the results of investigations aimed at enhancing the mechanical properties of products produced using FDM 3D printing. The results of the study in which the alterations in the mechanical properties of the 3D-printed parts were observed by applying post-process annealing are discussed. The research focused on post-process annealing to improve the mechanical properties of 3D-printed parts. The details of the mechanical and characterization tests conducted are discussed, and the corresponding outcomes are reported.

8.2 Materials

Polyetherimide (PEI) thermoplastic materials were employed in this study, and a comprehensive exposition on the characteristics of PEI can be found in Section 4. PEI is classified as an amorphous polymer, characterized by its non-crystalline molecular structure. The selection of PEI was based on its specific physical and chemical properties, from which it was deemed suitable for the intended research objectives.

8.3 Methods

8.3.1 Material Printing and Annealing Process

The test samples were produced using a Fortus 450mc 3D printer, and comprehensive technical information regarding this printer can be found in Section 5 of this study. This research was conducted in two phases. In the first phase, nine cubic samples were manufactured to determine the range of annealing temperatures. The initial annealing temperature for PEI was selected as 220°C, as primarily based on its proximity to the glass transition temperature of the polymer materials.

Previous studies have demonstrated that the annealing temperature of a polymer should exceed its glass transition temperature to enhance its mechanical properties [189]–[193]. Thus, in this investigation, the annealing process was initiated at 220°C, which is in close proximity to the glass transition temperature of PEI (215°C). Figure 8. 1 displays the DSC curves obtained for the PEI polymer sample. Based on the DSC analysis result, as seen in Figure 8. 1, the glass transition temperature of the PEI material is observed to be approximately 215°.

In the initial phase of this investigation, the specimens were subjected to a series of annealing temperatures ranging from 220 to 300°C, in 10°C intervals, to establish the temperature range for annealing. Subsequently, the focus shifted to temperatures within the range of 220 to 235°C, in 5°C intervals, in the subsequent stage. The annealing process was performed using a MagmaTherm (MT-1200) oven. The specimens were positioned on a flat plate within the oven and subjected to the designated temperatures for a duration of three hours. Subsequently, the specimens were allowed to cool naturally to room temperature whilst remaining in the oven. Figure 8. 2 presents the test specimens used in the study, their dimensional measurements, and in-situ images captured during the tests.

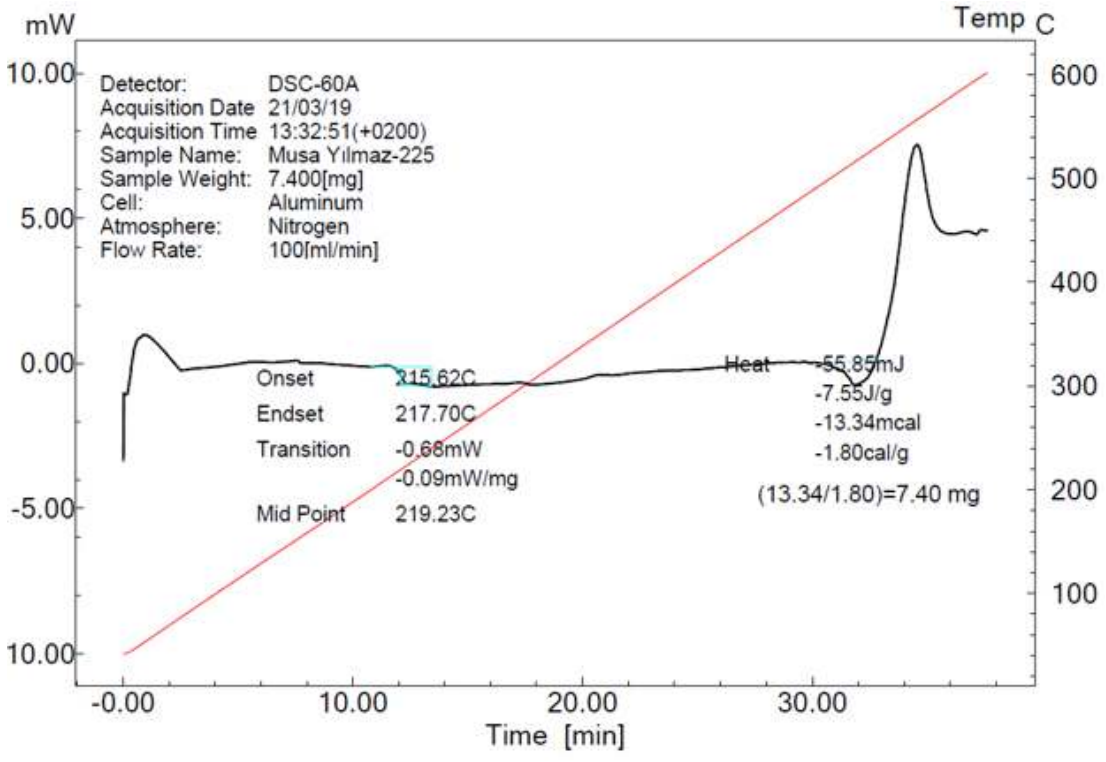

Figure 8. 1 DSC graph for PEI

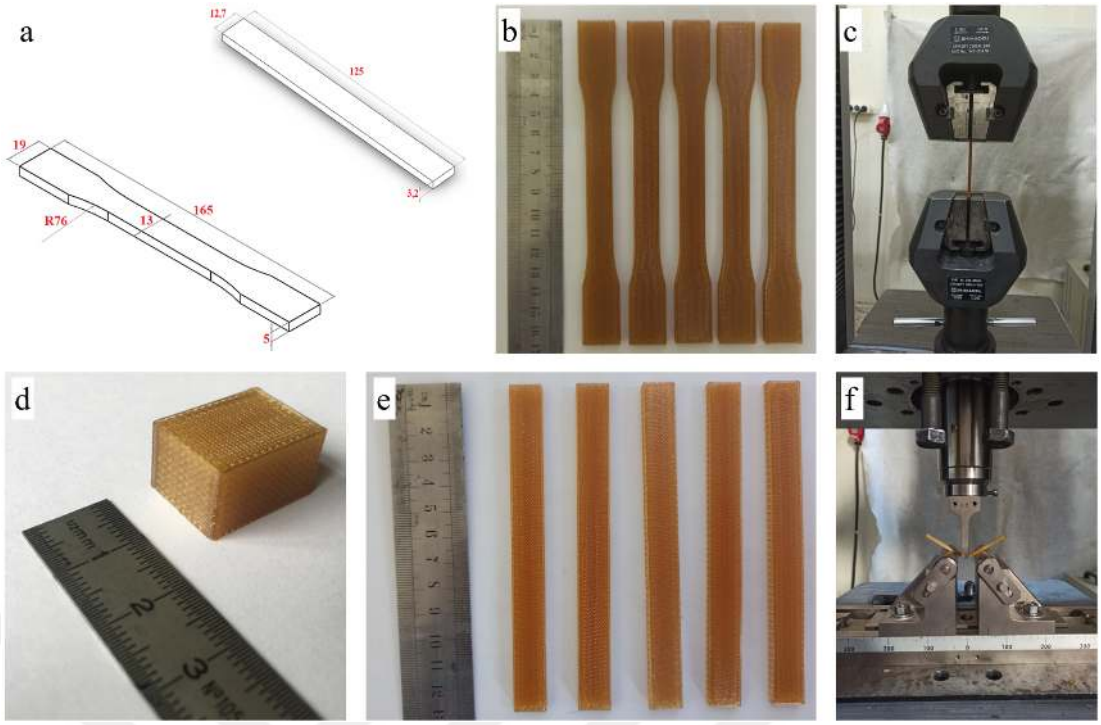

Figure 8. 2 Sample images used in the study: a) sample dimensions conforming to ASTM standard, b) tensile test samples, c) in-situ image captured during tensile test, d) cubic sample employed for preliminary tests, e) bending test samples, and f) in-situ image captured during flexure test

8.3.2 Characterization and Testing

The chemical composition of the specimens was analyzed using Fourier transform infrared (FTIR) spectroscopy, employing a Shimadzu IRTracer-100 spectrometer at ambient temperature. The specimens underwent scanning in the range 4000 to 400 cm^{-1}, with a resolution of 4 cm^{-1}. The spectra were collected in the wavenumber range of 4000 to 400 cm^{-1}, allowing for the identification of various chemical bonds and structural changes induced by the annealing process. By examining the FTIR data, insights into the effects of annealing on the molecular structure and chemical properties of PEI materials can be gained, which is crucial to an understanding of their performance and potential applications in different fields.

X-ray diffraction (XRD) analysis of both annealed and unannealed PEI samples was performed using a RIGAKU Miniflex 600 XRD system using Cu Kα radiation. The scattering angles (2θ) were measured in the range of 10° to 70° at a scanning rate of 0.02° min^{-1}. XRD patterns for the unannealed and annealed PEI samples were obtained

and analyzed to investigate the crystallographic characteristics of the materials. These XRD patterns provide valuable information about the arrangement of atoms, the presence of crystalline phases, and any changes induced by the annealing process. By examining the diffraction patterns, we can gain insights into the structural modifications and crystallinity of the PEI samples, contributing to a deeper understanding of their thermal behavior and potential applications.

Micrographs of the fractured surfaces of the 3D-printed PEI samples were acquired using a Zeiss Sigma 300 scanning electron microscope (SEM). The fracture surfaces of all PEI samples were examined to investigate the impact of fracture on the fibers. Prior to SEM analysis, the specimens were given a thin coating of palladium/gold.

Differential scanning calorimetry (DSC) analysis was conducted on the 3D-printed PEI sample using a SHIMADZU DSC-60 instrument. The DSC measurements involved heating the sample from room temperature to 600°C at a heating rate of 15°C/min under a nitrogen atmosphere. Thermograms were obtained to study the thermal behavior and characteristics of the PEI sample.

The tensile tests on both annealed and unannealed samples were performed using a Shimadzu AGX universal testing device. The tests were conducted in accordance with ASTM D638 [173], following standard tension test procedures. A strain rate ($\dot{\varepsilon}$) of 5 mm/min was applied during the tests. All experiments were conducted under controlled room conditions, maintaining constant temperature and humidity. Five identical samples were prepared for each test condition. Test values were obtained by averaging the results of five consecutive measurements.

The bending tests on both annealed and unannealed PEI samples were conducted using a Shimadzu AGX universal testing device. The testing procedure described in ASTM D790-17 [181] was employed to ensure consistent and standardized testing. A symmetric three-point bending test was performed on a 30 mm span at a constant speed of 1.56 mm/sec. Each bending test was carried out by averaging the results from five individual specimens.

Hardness tests were conducted using a portable BAREISS HPE II D-type shore hardness tester (Bareiss Heinrich Prüfgerätebau GmbH, Oberdischingen, Germany). The measurement of Shore D hardness was performed in accordance with the ASTM D2240-15 [182] standard. Fifteen measurements were taken from different locations on each 10 mm thick sample, with a spacing of 6 mm between each measurement region; the average hardnesses were calculated based on these readings. All Shore hardness tests were conducted at room temperature.

8.4 Results and Discussion

This section presents the comprehensive findings from the experimental investigation of the mechanical and morphological characteristics of the annealed and unannealed PEI specimens. The study aimed to assess the impact of annealing temperatures on the interlayer adhesion, mechanical properties, and fracture behavior of 3D-printed PEI materials.

8.4.1 FTIR Spectroscopy Results

FTIR analysis was conducted to investigate the chemical structure and bonding characteristics of the annealed and unannealed PEI specimens. FTIR spectroscopy is a powerful technique that provides valuable information about the molecular vibrations and functional groups present in the polymer. Figure 8. 3 shows the FTIR spectra of both unannealed PEI specimens and those subjected to annealing at various temperatures (230°C, 270°C, and 300°C). These spectra were acquired during preliminary experiments to determine the appropriate annealing temperature range. The FTIR spectra provide insights into the molecular vibrations and chemical bonds present in the PEI polymer, allowing for the analysis of structural changes induced by the annealing process. The unannealed PEI specimen exhibits distinctive absorption features attributed to the imide group, including peaks at 1234 cm^{-1} (corresponding to aromatic ether C-O-C), and 1355 and 743 cm^{-1} (associated with C-N stretching and bending), and 1780 and 1720 cm^{-1} (characteristic of imide carbonyl symmetric and asymmetric stretches) [194]. Notably, these characteristic imide group absorptions remain unchanged in samples annealed up to 270°C. Nevertheless, upon subjecting the PEI sample to higher annealing temperatures, observable indications of chemical degradation became evident. The presence of peaks corresponding to aromatic ether (C-O-C) and the characteristic C-N stretching and bending modes of imide carbonyl

symmetric and asymmetric vibrations at 400 cm^{-1} and 1800 cm^{-1} were no longer apparent (Figure 8. 3). Hence, it can be inferred that chemical degradation takes place within the intermolecular bonds of the PEI polymer annealed in the temperature range of 270°C to 300°C. Based on the analysis conducted on the heat-treated samples during the initial phase, temperature ranges were determined where no distortion occurs above the glass transition temperature.

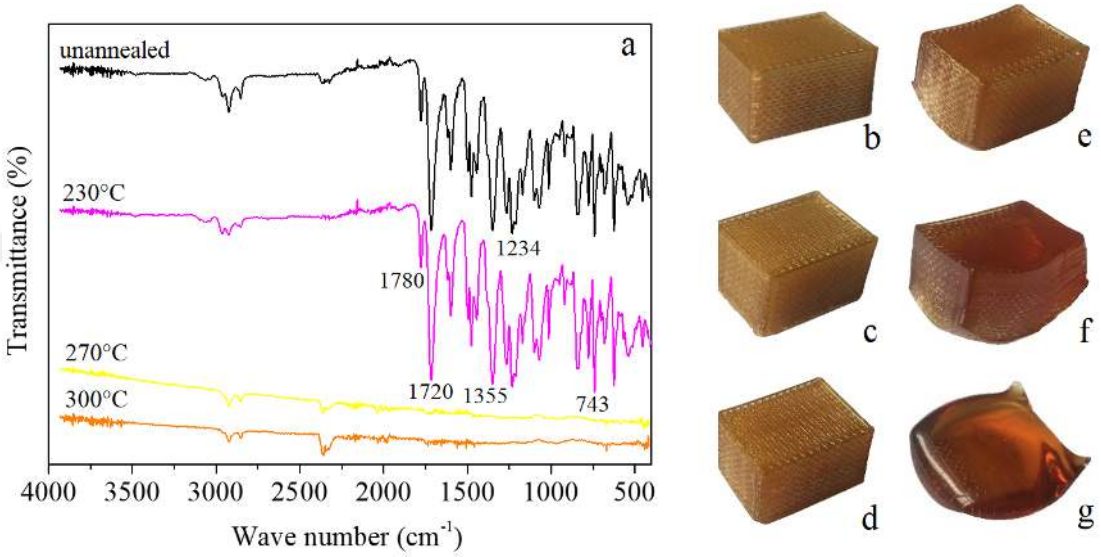

Figure 8. 3 a) FTIR spectra of unannealed and annealed PEI samples at 230°C, 270°C, and 300°C, b) the physical appearance of specimens when unannealed, and the physical appearance of specimens when annealed at c) 235°C, d) 240°C, e) 270°C, f) 280°C, and g) 300°C

Additionally, the variations in physical appearance between the unannealed and annealed (at 235°C, 240°C, 270°C, 280°C, and 300°C) PEI specimens are presented in Figure 8. 3. These visual observations complement the FTIR analysis and provide a comprehensive overview of the morphological changes associated with the annealing process. Significant physical degradation, including profile distortion and color alteration, was observed in the PEI material following the annealing process at elevated temperatures. The heat treatment conducted in the initial stage revealed notable alterations in the profile and color of the PEI specimens that was attributed to thermal effects, and were particularly evident above a temperature threshold of 235°C. Annealing the PEI material at 300°C resulted in the complete melting of the sample, leading to a dramatic transformation in its physical form.

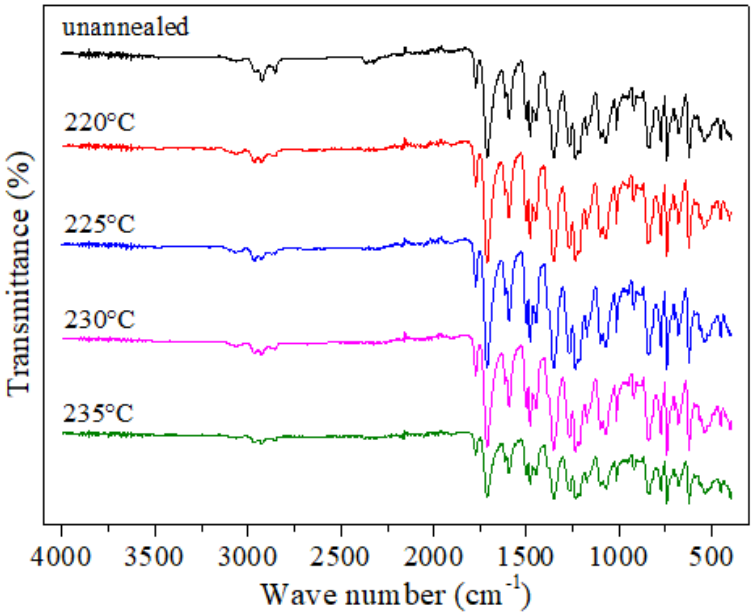

Figure 8. 4 FTIR spectra of unannealed PEI, and annealed PEI samples at 220°C, 225°C, 230°C, and 235°C

Previous research has established that the annealing temperature of a polymer should exceed its glass transition temperature to enhance the resulting mechanical properties, as reported in references [189]–[193]. Based on the aforementioned considerations, the lower and upper boundaries of the annealing temperature range were established to be 220°C and 235°C, respectively. Subsequent heat treatments were conducted within this range, specifically at temperatures of 220°C, 225°C, 230°C, and 235°C, using the oven as the thermal environment. Figure 8. 4 presents the FTIR spectra obtained for the PEI samples in the second phase of the study. The primary objective of the initial stage of experimentation was to establish the boundaries of the annealing temperature range.

PEI samples subjected to annealing temperatures of 220°C, 225°C, 230°C, and 235°C exhibited characteristic infrared (IR) patterns that closely resembled those of the unannealed PEI sample. This observation suggests that the annealed PEI samples retained the fundamental structure of the PEI polymer. Nevertheless, the intensity of the FTIR peaks for the PEI samples annealed at 235°C exhibited a noticeable reduction compared to both the unannealed sample and the specimens annealed at 220°C, 225°C, and 230°C. The FTIR spectra of the specimens exhibit significant absorbance peaks

(corresponding to characteristic imide group absorptions) at approximately 743 cm^{-1}, 1234 cm^{-1}, 1355 cm^{-1}, 1720 cm^{-1}, and 1780 cm^{-1}, as reported in reference [194].

8.4.2 XRD Results

XRD analysis was conducted to investigate the structural characteristics of the annealed and unannealed PEI samples. XRD is a powerful technique that provides valuable insights into the crystalline structure, and crystallinity, of materials. The XRD results offer essential information about the impact of annealing on the structural properties of the PEI material, shedding light on its changes in crystallinity.

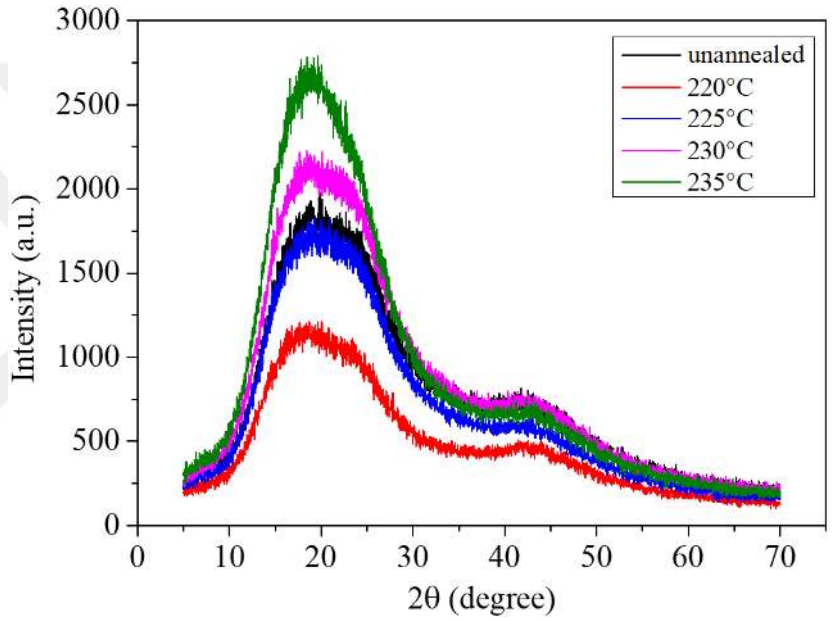

Figure 8. 5 XRD pattern obtained from the X-ray diffraction analysis of unannealed and annealed PEI samples

Figure 8. 5 illustrates the XRD patterns obtained for both the unannealed and annealed PEI samples, covering a 2θ range of 5° to 70°. The XRD spectra reveal that all 3D-printed PEI specimens exhibit a predominantly amorphous structure. The observed X-ray diffraction curves exhibit broad bands without any notable or discernible peaks within the scanned region. This absence of distinct crystalline peaks further confirms the amorphous nature of the PEI material in its printed form. XRD profiles of the PEI samples exhibited a prominent broad peak centered at 2θ = 19.3° [195], [196], along with a relatively weak peak at approximately 41.9°. Notably, no distinct crystalline peaks were observed in the XRD spectra, indicating the predominantly amorphous

nature of the samples. However, it was observed that the intensity of the peak at 19.3° varied with the application of different annealing treatments to the PEI specimens. This observation suggests that the annealing process has an impact on the structural arrangement or ordering within the PEI material, potentially influencing its physical and mechanical properties. The XRD analysis revealed distinct variations in the patterns of the annealed PEI samples, highlighting different trends among the specimens. Specifically, the XRD profiles of samples annealed at 220°C and 225°C exhibited lower measured intensities and humps compared to the unannealed sample. In contrast, samples annealed at 230°C and 235°C displayed higher intensities and humps. These observations suggest that the annealing process may have been influenced by the crystal forms and internal structures of the PEI material. These findings provide insights into the effects of annealing operations on the structural properties of PEI [197].

8.4.3 Microstructural Analysis Results

In this section, the results of microstructure analysis on the fracture surfaces of 3D-printed PEI samples are presented. The examination was carried out using an SEM to obtain detailed micrographs. The aim is to obtain information about the fracture behavior, interfacial bonding of fibers, and general morphology of the PEI material under different annealing conditions by examining the microstructure.

The microstructural features and 3D-printed configurations of the PEI specimens, encompassing both transverse and longitudinal cross-sections of the fibers, are visually represented in Figure 8. 6. This figure provides a comprehensive view of the overall morphology and structural characteristics of the PEI specimens, offering insights into the arrangement and orientation of the fibers within the printed structures. In the sample fabricated using a raster angle of 0°/90°, as illustrated in Figure 8. 6a, the successive layers exhibit a distinct arrangement, with transverse fibers (0°) predominating in the lower layer and longitudinal fibers (90°) prevailing in the uppe. This observation highlights the systematic alignment of the fibers in relation to the printing direction, showcasing the characteristic fiber orientations in each layer of the printed structure. SEM micrographs present the fracture surfaces of the specimens following the tensile test, revealing the morphology of the fractured samples. Figure 8. 6c exhibits the SEM images depicting two distinct modes of failure observed in the

tensile samples: interfacial bond failure, and fiber breakage. These observations provide valuable insights into the fracture behavior and failure mechanisms of the tested samples. The tensile force exerted on the longitudinally deposited fibers resulted in fractures primarily occurring at the surfaces of these fibers. In contrast, when the tensile force was applied to the transversely deposited fibers, fracturing took place exclusively at the interface. This behavior signifies a clear correlation between the orientation of the fibers and the location of fracture initiation points.

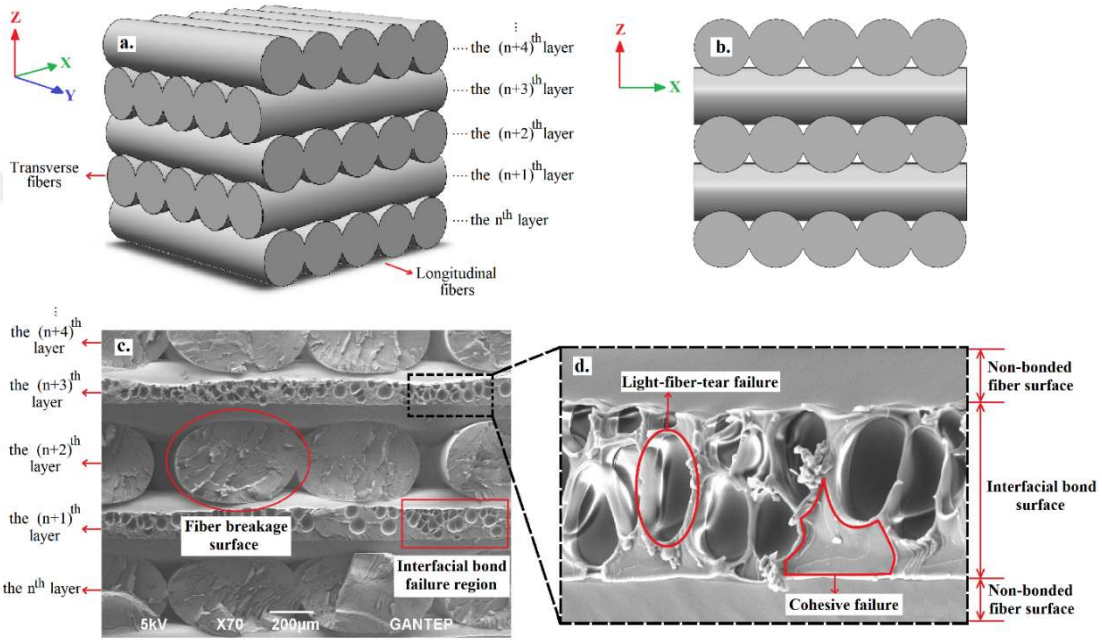

Figure 8. 6 Structure of 3D-printed PEI model: a) schematic drawing of perspective view, b) schematic drawing of front view, c) general micrograph of the tensile fracture surface obtained via SEM analysis, d) general micrograph of the interfacial surface

The fracture surface of the longitudinally oriented fibers exhibited a uniform and smooth appearance, characteristic of brittle fracture behavior. In contrast, the interfacial bond failure region displayed two distinct modes of failure: cohesive failure, and light-fiber-tear failure, as illustrated in Figure 8. 6d [198], [199]. Light-fiber-tear failure manifested as a thin cavity layer near the fiber surface, and occurs within the interfacial bond region. This failure mode is particularly prominent in the transverse tensile strength of the 3D-printed product, where peel stress predominates and initiates crack propagation along the bond line. Interfacial bond failure occurs when the

adherend exhibits its weakest strength, and is contingent upon the adhesive strength between two adjoining filaments.

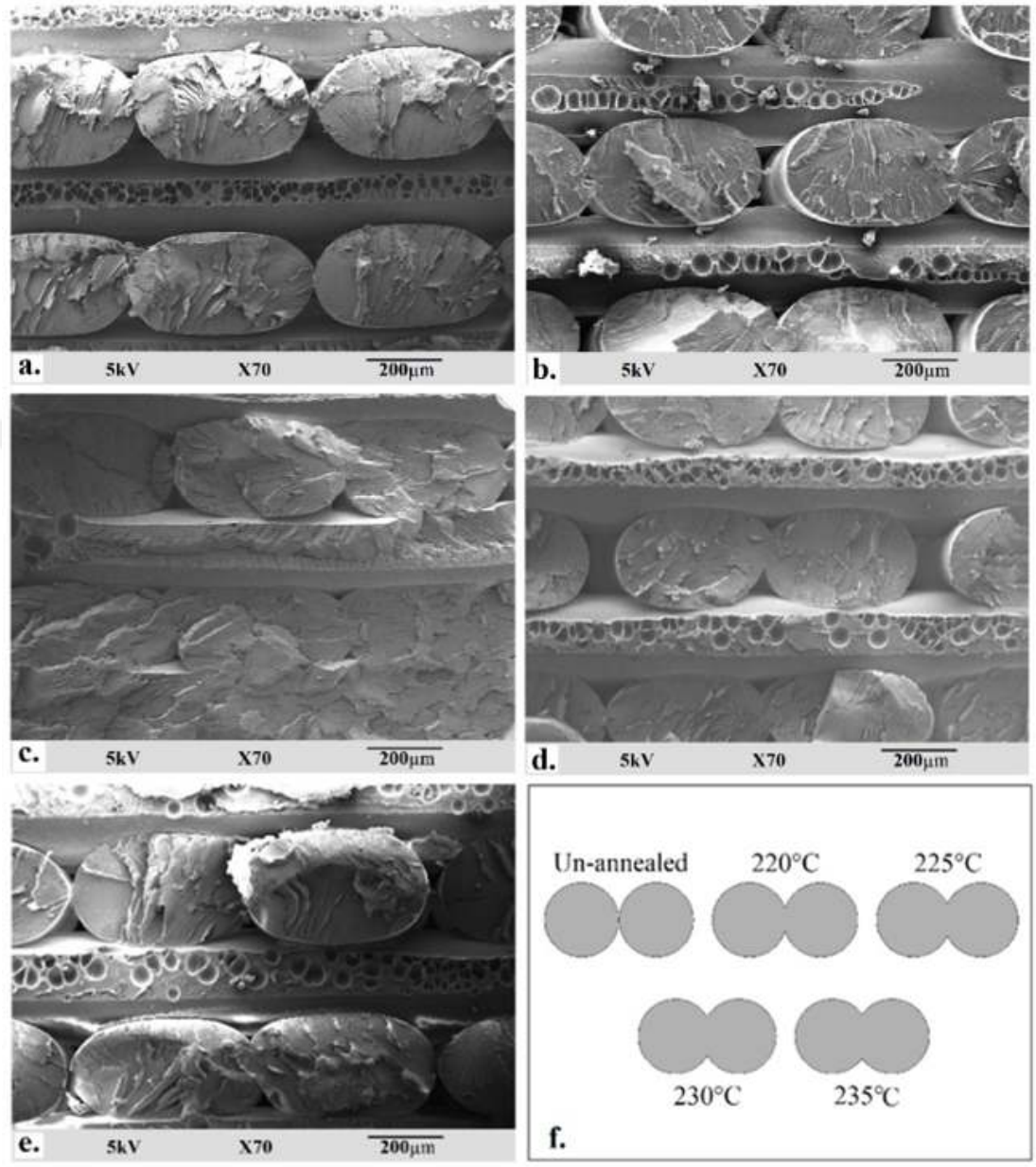

Figure 8. 7 SEM image of a 3D-printed PEI specimen: a) unannealed, b) annealed at 220°C, c) annealed at 225°C, d) annealed at 230°C, e) annealed at 235°C, and f) schematic representation of the change in bond formation between filaments with the annealing process

The SEM micrograph captured for the investigation of fracture surfaces resulting from the tensile test is presented in Figure 8. 7. An identical fracture mechanism was consistently observed in both the annealed and unannealed samples. In the longitudinal

direction fibers, fracture occurred through fiber breakage, whereas in the transverse direction fibers, interfacial bond failure was observed. Figure 8. 7f demonstrate that as the annealing temperature increases, there is a convergence of filaments and an increase in the interfacial bond area, suggesting an enhancement in the strength of the interfacial bond. Notably, the unannealed sample exhibited the lowest interfacial bond area, while the sample annealed at 235°C displayed the highest interfacial bond area (Figure 8. 7a and e). Consequently, the increase in annealing temperature leads to an increase in the interfacial bond surface area and a strengthening of the interfacial bonds, as facilitated by the diffusion of PEI molecules.

8.4.4 Tensile Test Results

The tensile test results for the unannealed and annealed 3D-printed PEI specimens are presented in Figure 8. 8. The unannealed sample exhibited a tensile strength of 68.12 MPa, representing the maximum stress the material could withstand under tensile loading before failure occurred. A gradual increase in the tensile strength of the samples was observed as the annealing temperature was increased up to 225°C. However, when the annealing process was applied at temperatures above 225°C, a slight decrease in the tensile stress value of the PEI material was observed. The tensile strengths of all annealed samples were found to be higher than that of the unannealed specimen. The maximum increase in tensile strength was observed to be 75.11 MPa, corresponding to an approximate 10.3% increase, in the sample annealed at 225°C compared to the unannealed specimen. These findings indicate that the annealing process at temperatures up to 225°C enhances the tensile strength of the material. However, beyond this annealing temperature, there is a slight decline in the tensile strength, suggesting a potential limit to the beneficial effects of annealing on the material's mechanical properties. The observed increase in tensile strength can be attributed to the enhanced interlayer diffusion of PEI molecules occurring during the annealing process. This promotes improved molecular bonding and interconnectivity within the material, resulting in enhanced mechanical properties, including increased tensile strength.

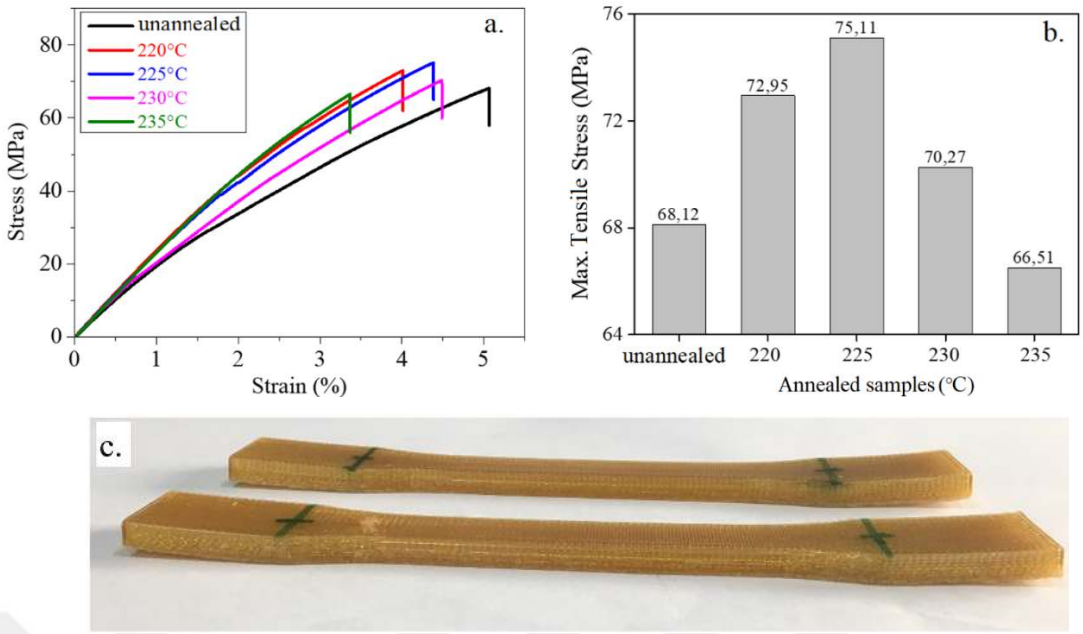

Figure 8. 8 Tensile test results for PEI specimens; a) stress-strain graph, and b) comparison of ultimate tensile stress

The SEM images depicted in Figure 8. 7 illustrate that the bonding zone between interfaces expands with increasing annealing temperature, indicating an anticipated increase in strength as the annealing temperature is increased. However, it is important to note that while the increase in annealing temperature positively influences the bonding surface area, it also introduces adverse effects in the form of thermal distortion.

The annealing process is postulated to enhance the crystallinity of the polymer through the restructuring of chains within the amorphous region, as indicated by previous studies [200], [201]. Increased crystallinity was found to correlate with improved tensile strength; however, it is noted that when performing high-temperature annealing operations due to the potential occurrence of undesired thermal effects, such as thermal distortion and residual stress, this can have a detrimental impact on tensile strength [202]–[204]. The results of the XRD analysis (Figure 8. 5) indicate distinctions in the extent of the crystallinity of the samples annealed at 220°C and 225°C compared to those annealed at 230°C and 235°C. Consequently, the decrease in tensile stress is considered, in part, to be due to variations in the crystallinity index.

The observed trend suggests that the tensile strength exhibits an upward trend with increasing annealing temperature beyond the glass transition point. However, it is noteworthy that samples subjected to annealing temperatures exceeding 225°C display noticeable thermal distortions. The samples annealed at 220°C and 225°C exhibit no discernible signs of thermal distortion, whereas the samples annealed at 230°C and 235°C display noticeable distortions attributed to the elevated annealing temperatures. Figure 8. 8c visually illustrates the observed distortions in these samples. At elevated annealing temperatures, the samples can exhibit significant deformation due to their own weight, as documented in previous research [92]. The post-process annealing of 3D-printed samples can result in thermal distortion, leading to the presence of residual stress and residual distortion, as reported in previous studies [205]. The tensile strength of the samples annealed at 230°C and 235°C was observed to decrease during the test, which can be attributed to the presence of residual stresses and residual distortions caused by the annealing process. While the interfacial bonds of the annealed samples exhibited increased strength, it is hypothesized that the decrease in tensile strength of the specimens can be attributed to the presence of residual stresses resulting from the annealing process [206], [207].

The fracture strain of 3D-printed PEI polymer specimens, as illustrated in Figure 8. 9, was found to be influenced by the annealing process. However, unlike the tensile strength values, the fracture strain does not consistently increase with increasing annealing temperature. The fracture strains of the unannealed sample and samples annealed at 220°C, 225°C, 230°C, and 235°C were measured to be 5.07, 4.49, 4.38, 4.01, and 3.37, respectively. The tensile test results indicate a slight decrease in fracture strain when samples undergo heat treatment. This behavior can be attributed to the increased stiffness observed with higher annealing temperatures. This observation aligns with the findings of Harris et al. [200], who reported a reduction in elongation at break during the annealing process. However, the fracture strain remained relatively unchanged among the annealed specimens. The tensile test results for samples subjected to annealing temperatures of 220°C, 225°C, and 230°C revealed increased stress levels and decreased levels of fracture strain, indicating a transition toward brittle behavior. The annealed specimens exhibit reduced ductility, indicating that heat-treatment operations lead to a decrease in ductility.

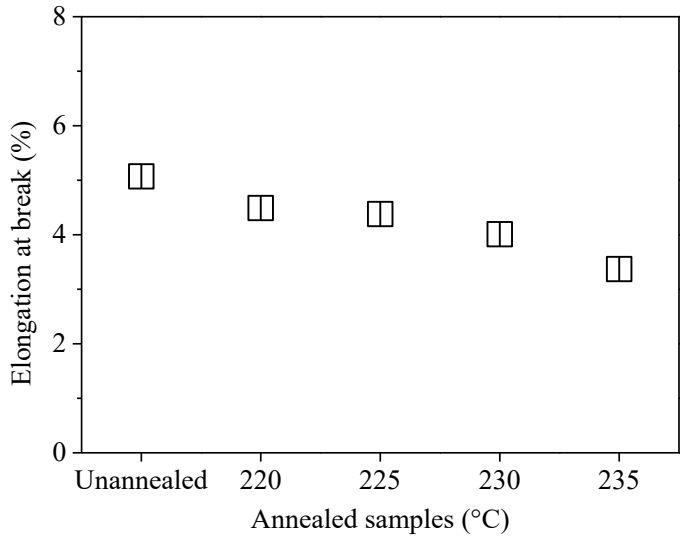

Figure 8. 9 Elongation at break of for 3D-printed PEI polymer specimens

8.4.5 Bending Test Results

The bending test results, presented in Figure 8. 10 demonstrate that the flexural strength and maximum bending force of the annealed samples surpass those of the unannealed sample, indicating improved mechanical properties. It can be stated that the bending test results exhibit a similar trend to the tensile test results, indicating a consistent relationship between the mechanical properties evaluated in both tests. The flexural strength of the PEI specimens demonstrates a slight increase up to an annealing temperature of 225°C, after which it exhibits a gradual decline. The sample annealed at 225°C exhibits the highest increment in maximum bending strength.

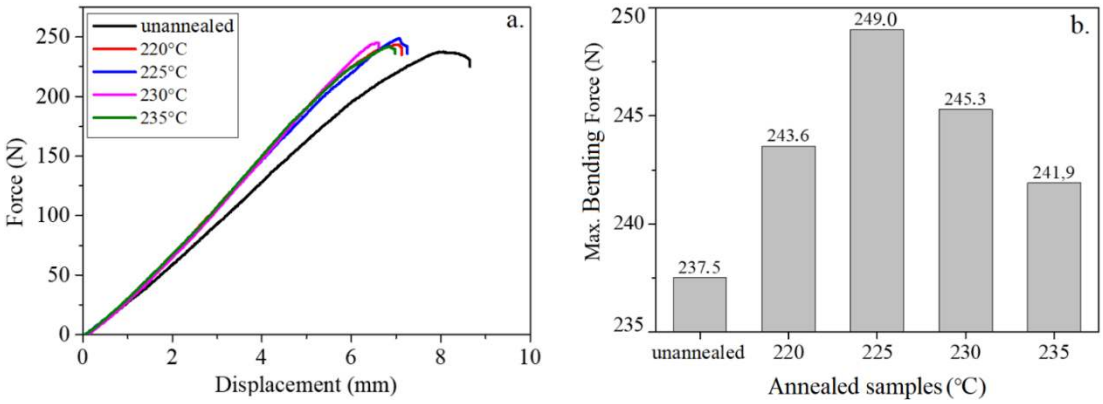

Figure 8. 10 Bending test results for PEI specimens; a) maximum force and displacement graph, and b) maximum force comparison

The application of heat treatment to PEI specimens above the glass transition temperature promotes the diffusion of PEI molecules between layers, leading to enhanced interlayer bonding and, consequently, improved mechanical properties. Multiple research studies have provided supporting evidence for this observation [189]–[193]. However, with an increase in annealing temperature beyond 225°C, the samples exhibit thermal distortions, and the PEI material exhibits heightened brittleness. Consequently, the bending strength shows a decreasing trend above 225°C.

8.4.6 Hardness Test Results

Figure 8. 11 displays the results of the D-type Shore hardness test conducted on both unannealed and annealed PEI samples. Shore hardness, a commonly employed technique for assessing the hardness of plastics [184], quantifies the resistance of a polymer material to the penetration of a rigid indenter into its surface layers. This property is determined by measuring the depth of indentation made by the indenter in the polymer material being tested. The hardness of all annealed samples exhibited an increase in comparison to the unannealed sample. The highest level of hardness was observed in the sample annealed at 235°C, exhibiting a significant increase of approximately 12.3% compared to the unannealed sample. With increasing annealing temperature, the hardness of the PEI samples displayed a rising trend. Nevertheless, beyond an annealing temperature of 225°C, the rate of at which hardness increased began to level off.

The augmentation in specimen hardness can be attributed to two underlying factors. Firstly, the annealing process led to a reduction in the size of the microvoids present within the microstructure of the 3D-printed component, as evidenced by previous studies [208]. The dimensions and intensity of these microvoids are anticipated to exhibit a variability that corresponds to the annealing temperature applied to the specimens, potentially resulting in changes to the hardness characteristics of the tested samples.

During the penetration of the rigid indenter, the layers beneath the surface of the specimens, which are fabricated using FDM with a 3D printer, are subjected to the applied indentation force, resulting in a specific indentation depth. In instances where the indenter frequently encounters microvoids, the hardness tends to decrease as the

indenter encounters diminished resistance. Another contributing factor is the strengthening of interfacial bonds through the heat-treatment process. The lower hardnesses observed in the printed parts can likely be attributed to insufficient bonding between the layers during the 3D-printing process. The annealing process enhances interfacial bonding and facilitates greater diffusion, leading to an increased resistance being encountered by the indenter during hardness measurement. As a result, the observed hardnesses appear to increase. Furthermore, the tensile test results provide additional evidence of increased brittleness, as indicated by the decrease in fracture strain. This decrease in fracture strain aligns with the observed increase in hardness, supporting the notion of increased hardness being associated with enhanced brittleness.

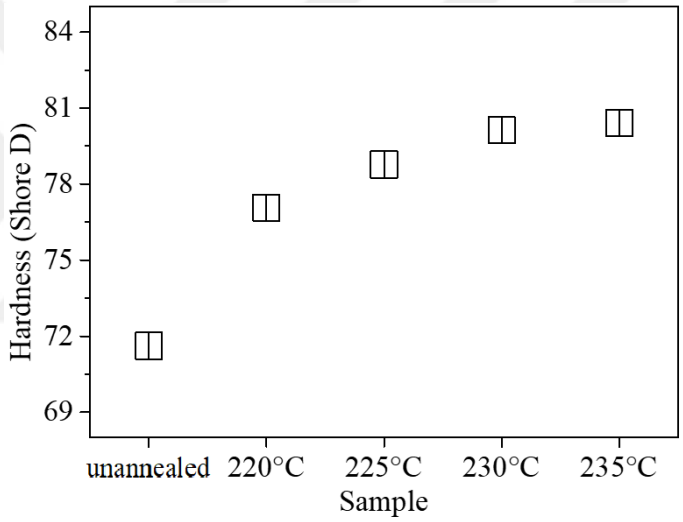

Figure 8. 11 Hardness test results for PEI samples

The mechanical behavior of the 3D-printed PEI parts was assessed through a series of consecutive mechanical tests. The most favorable mechanical properties were observed in the specimens annealed at 225°C in comparison to the unannealed samples. However, a degradation in mechanical performance was observed when annealing was conducted above 225°C. Specifically, the maximum tensile strength recorded for the sample annealed at 235°C was found to be 66.51 MPa, which was lower than that of the unannealed sample. While tensile and bending test results exhibited this trend, the hardness of the specimens increased with higher annealing temperatures.

CHAPTER 9

CONCLUSIONS

This study was conducted with the primary objective of enhancing the mechanical properties of parts produced using the Fused Deposition Modeling (FDM) technique, followed by the development of a new additive manufacturing device. The aim of the research was to investigate the impact of process parameters and post-processing techniques on the strength of the parts, while also focusing on introducing an innovative approach to enable the production of composite materials within the existing 3D printing systems. To achieve this goal, studies were conducted on process parameters and post-processing techniques, alongside the redesign of the extruder system of the 3D printer and the incorporation of an additional nozzle to transform it into a dual-needle 3D printer. Notably, in this approach, the second nozzle was specifically designed to spray reinforcement material instead of polymer material, enabling the independent operation of each nozzle. The conclusions are presented according to three main categories:

The Conclusions Related to the Production of a New Composite Material using a New Developed Dual-Needle and Agent-Based 3D Printer can be summarized as follows:

A novel composite material has been successfully produced through additive manufacturing using the low-cost poly(lactic acid) (PLA) filament commonly used in 3D printers. Peroxide material was added as a reinforcing agent to the PLA filament. The extruder design of the 3D printer was modified, and a second nozzle was added to facilitate the deposition of a thin film of peroxide material onto each layer of the PLA filament during printing. This study marks the first attempt to utilize a 3D printer capable of producing composites through in-situ cross-linking of polymer and peroxide, which represents a significant development in both the scientific and industrial domains.

The study successfully achieved the in-situ application of peroxide to each layer during additive manufacturing, a novel approach not previously explored in the literature. Unlike post-processing methods that only involve surface application after the product is obtained, this study introduced an innovative method by enabling cross-linking within each layer. Fourier-transform infrared spectroscopy (FTIR) analysis of the fabricated samples confirmed the occurrence of a chemical interaction between PLA and peroxide, indicating modification of the polymer chain structure through the introduction of new structural units by the peroxide. Consequently, the development of new composite material was achieved through cross-linking. Scanning electron microscopy (SEM) analysis of the developed composite samples revealed improved interfacial bonding between adjacent fibers, enhancing the interfacial bond strength. The tensile strength of the composite samples, fabricated using the widely used PLA filament with its inherent limitations in strength, was increased by approximately 27.5%. This study successfully demonstrated the production of novel composite material through additive manufacturing by enabling cross-linking between PLA polymer and peroxide material. The results demonstrate the successful operation of the newly developed device, which effectively facilitates the production of composite materials. The redesign of the extruder system and the addition of the second nozzle enabled precise deposition of the reinforcement material, yielding the desired outcomes. The device's performance was evaluated through testing and experimentation. Furthermore, the integration of the second nozzle affords greater flexibility in material combinations, thereby establishing a potential platform for the production of diverse composite materials. This advancement holds promise for expanding the range of future applications.

The Conclusions Related to the Effect of Different Alignments on Mechanical Properties can be summarized as follows:

In 3D manufacturing, the orientation of the deposited fiber in relation to applied tensile force plays a crucial role in determining the mechanical characteristics of the resulting product. Aligning the fibers with the anticipated forces is particularly crucial in applications like aerospace, automotive, and biomedical engineering, where tailored mechanical properties are desirable. For instance, aerospace components experiencing both compressive and tensile loads benefit from fibers aligned with the force direction,

while biomedical implants can be designed with fibers matching the mechanical properties of surrounding tissues. Thus, the relationship between applied force direction and fiber deposition direction during the manufacturing processes is important in terms of enhancing the mechanical properties of the end product. The findings suggest that raster angle orientation directly influences mechanical strength. Notably, poor interlayer bonding between deposited fibers is a result of the raster angle. It can be seen that if the direction of the applied tensile force and the direction of the fibers are the same, fiber breakage failure occurs; on the other hand, if the directions are different, interfacial bond failure, which is weaker in strength, is observed. Tensile tests on single-oriented samples revealed significant changes in the stress/strain diagram based on the raster angle. However, the analysis showed that higher tensile stresses were mostly achieved in multi-oriented production and did not show significant changes in raster angle. Consistent results were obtained from tensile and bending tests, indicating that samples produced with a 0° raster angle exhibited the best mechanical properties. The elongation at break varied depending on the layer configuration (single- or multi-oriented), while the tensile and bending test results for multi-oriented samples remained similar irrespective of the raster angle.

The Conclusions Related to the Effect of Post-processing on Mechanical Properties can be summarized as follows:

The aim of the investigation was to understand the impact of annealing on the properties of polyetherimide (PEI/ULTEM 1010), a high-strength material commonly used in 3D printing. Through experimentation, it was determined that annealing the 3D-printed PEI polymer at a temperature of 225°C yielded the most effective results. At temperatures higher than 225°C, a number of adverse effects, such as thermal degradation, were observed. The annealing process addressed the reduction in crystallinity caused by rapid cooling during 3D part production and improved interfacial bond formation. Consequently, the interlayer mechanical properties of the 3D-printed PEI polymer were enhanced. Higher annealing temperatures resulted in lower tensile stresses and bending forces. Tensile test results indicated that the maximum tensile stress in the annealed sample at 235°C was lower than that in the unannealed sample. The hardness test results demonstrated an increase in material hardness with higher annealing temperatures. These findings confirm that slightly

elevating the temperature above the glass transition temperature and slow cooling in the oven contribute to enhanced interlayer adhesion and the formation of a more stable and crystalline structure in PEI materials. Overall, this study showcases the efficiency of post-processing annealing for 3D-printed PEI polymers and contributes to the scientific understanding of crystallinity and mechanical property changes induced by heat treatment.

RECOMMENDATIONS FOR FUTURE WORK

The findings of this research open up several possibilities for future exploration and improvement in the field of additive manufacturing. The developed composite material and the agent-based production method show great promise, and future studies could potentially focus on refining and expanding these approaches to enhance the strength and functionality of produced parts. Moreover, the use of alternative reinforcement peroxides or other additives and alternative polymer filament could be explored to improve the properties of the composite material further. Also, research could focus on transforming the 3D printer into a production system, incorporating advanced capabilities for autonomous decision making during production. This can be achieved by integrating Finite Element Method analysis and automation into the system. By leveraging FEM analysis, the 3D system could evaluate the structural integrity and performance of the printed parts in real time. Based on the analysis results, the system could autonomously adjust various spray production parameters, such as spraying pressure, angle, volume, and material composition, to optimize the quality and functionality of printed objects.

REFERENCES

[1] S.-C. Park, 'The Fourth Industrial Revolution and implications for innovative cluster policies', *Ai Soc.*, vol. 33, pp. 433–445, 2018.

[2] E. Abele, J. Metternich, M. Tisch, E. Abele, J. Metternich, and M. Tisch, 'Challenges for future production/manufacturing', *Learn. Factories Concepts, Guidel. Best-Practice Examples*, pp. 1–21, 2019.

[3] A. Reiman, J. Kaivo-oja, E. Parviainen, E.-P. Takala, and T. Lauraeus, 'Human factors and ergonomics in manufacturing in the industry 4.0 context–A scoping review', *Technol. Soc.*, vol. 65, p. 101572, 2021.

[4] M. Bortolini, E. Ferrari, M. Gamberi, F. Pilati, and M. Faccio, 'Assembly system design in the Industry 4.0 era: a general framework', *Ifac-Papersonline*, vol. 50, no. 1, pp. 5700–5705, 2017.

[5] L. Wang and G. Wang, 'Big data in cyber-physical systems, digital manufacturing and industry 4.0', *Int. J. Eng. Manuf.*, vol. 6, no. 4, pp. 1–8, 2016.

[6] A. Khan and K. Turowski, 'A survey of current challenges in manufacturing industry and preparation for industry 4.0', in *Proceedings of the First International Scientific Conference "Intelligent Information Technologies for Industry"(IITI'16) Volume 1*, 2016, pp. 15–26.

[7] L. Banjanović-Mehmedović and F. Mehmedović, 'Intelligent manufacturing systems driven by artificial intelligence in industry 4.0', in *Handbook of Research on Integrating Industry 4.0 in Business and Manufacturing*, IGI global, 2020, pp. 31–52.

[8] S. K. Jagatheesaperumal, M. Rahouti, K. Ahmad, A. Al-Fuqaha, and M. Guizani, 'The duo of artificial intelligence and big data for industry 4.0: Applications, techniques, challenges, and future research directions', *IEEE Internet Things J.*, vol. 9, no. 15, pp. 12861–12885, 2021.

[9] F. Tao, Q. Qi, L. Wang, and A. Y. C. Nee, 'Digital twins and cyber–physical systems toward smart manufacturing and industry 4.0: Correlation and comparison', *Engineering*, vol. 5, no. 4, pp. 653–661, 2019.

[10] N. Araújo, V. Pacheco, and L. Costa, ‘Smart Additive Manufacturing: The Path to the Digital Value Chain’, *Technologies*, vol. 9, no. 4, p. 88, 2021.

[11] R. Ashima, A. Haleem, S. Bahl, M. Javaid, S. K. Mahla, and S. Singh, ‘Automation and manufacturing of smart materials in Additive Manufacturing technologies using Internet of Things towards the adoption of Industry 4.0’, *Mater. Today Proc.*, vol. 45, pp. 5081–5088, 2021.

[12] G. Li, Y. Hou, and A. Wu, ‘Fourth Industrial Revolution: technological drivers, impacts and coping methods’, *Chinese Geogr. Sci.*, vol. 27, pp. 626–637, 2017.

[13] R. C. Santos and J. L. Martinho, ‘An Industry 4.0 maturity model proposal’, *J. Manuf. Technol. Manag.*, 2020.

[14] U. Krishnan, ‘The Industry 4.0 and its associated technologies’, *J. Emerg. Technol.*, vol. 1, no. 1, pp. 1–10, 2021.

[15] P. Verma, V. Kumar, T. Daim, N. K. Sharma, and A. Mittal, ‘Identifying and prioritizing impediments of industry 4.0 to sustainable digital manufacturing: A mixed method approach’, *J. Clean. Prod.*, vol. 356, p. 131639, 2022.

[16] M. L. Nunes, A. C. Pereira, and A. C. Alves, ‘Smart products development approaches for Industry 4.0’, *Procedia Manuf.*, vol. 13, pp. 1215–1222, 2017.

[17] R. Y. Zhong, X. Xu, E. Klotz, and S. T. Newman, ‘Intelligent manufacturing in the context of industry 4.0: a review’, *Engineering*, vol. 3, no. 5, pp. 616–630, 2017.

[18] J. Mo, R. R. Dehoff, W. H. Peter, T. J. Toops, J. B. Green Jr, and F.-Y. Zhang, ‘Additive manufacturing of liquid/gas diffusion layers for low-cost and high-efficiency hydrogen production’, *Int. J. Hydrogen Energy*, vol. 41, no. 4, pp. 3128–3135, 2016.

[19] M. Dean and J. Spoehr, ‘The fourth industrial revolution and the future of manufacturing work in Australia: challenges and opportunities’, *Labour Ind. a J. Soc. Econ. relations Work*, vol. 28, no. 3, pp. 166–181, 2018.

[20] B. A. Praveena, N. Lokesh, A. Buradi, N. Santhosh, B. L. Praveena, and R. Vignesh, ‘A comprehensive review of emerging additive manufacturing (3D printing technology): Methods, materials, applications, challenges, trends and future potential’, *Mater. Today Proc.*, vol. 52, pp. 1309–1313, 2022.

[21] I. G. Ian Gibson, ‘Additive manufacturing technologies 3D printing, rapid prototyping, and direct digital manufacturing’. Springer, 2015.

[22] C. K. Chua and K. F. Leong, *3D Printing and additive manufacturing: Principles and applications (with companion media pack)-of rapid prototyping*. World Scientific Publishing Company, 2014.

[23] D. Gu, X. Shi, R. Poprawe, D. L. Bourell, R. Setchi, and J. Zhu, 'Material-structure-performance integrated laser-metal additive manufacturing', *Science (80-.).*, vol. 372, no. 6545, p. eabg1487, 2021.

[24] A. Raj, G. Dwivedi, A. Sharma, A. B. L. de Sousa Jabbour, and S. Rajak, 'Barriers to the adoption of industry 4.0 technologies in the manufacturing sector: An inter-country comparative perspective', *Int. J. Prod. Econ.*, vol. 224, p. 107546, 2020.

[25] J. F. Arinez, Q. Chang, R. X. Gao, C. Xu, and J. Zhang, 'Artificial intelligence in advanced manufacturing: Current status and future outlook', *J. Manuf. Sci. Eng.*, vol. 142, no. 11, 2020.

[26] S. M. E. Sepasgozar, A. Shi, L. Yang, S. Shirowzhan, and D. J. Edwards, 'Additive manufacturing applications for industry 4.0: A systematic critical review', *Buildings*, vol. 10, no. 12, p. 231, 2020.

[27] J. Butt, 'Exploring the interrelationship between additive manufacturing and Industry 4.0', *Designs*, vol. 4, no. 2, p. 13, 2020.

[28] Scopus, 'The annual trend in the publications and patents related to additive manufacturing in recent years'. https://www.scopus.com/

[29] S. Ouassil, A. El Magri, H. R. Vanaei, and S. Vaudreuil, 'Investigating the effect of printing conditions and annealing on the porosity and tensile behavior of 3D-printed polyetherimide material in Z-direction', *J. Appl. Polym. Sci.*, p. e53353.

[30] M. Javaid, A. Haleem, R. P. Singh, R. Suman, and S. Rab, 'Role of additive manufacturing applications towards environmental sustainability', *Adv. Ind. Eng. Polym. Res.*, vol. 4, no. 4, pp. 312–322, 2021.

[31] X. Qian *et al.*, 'A critical review and commentary on recent progress of additive manufacturing and its impact on membrane technology', *J. Memb. Sci.*, vol. 645, p. 120041, 2022.

[32] S. A. M. Tofail, E. P. Koumoulos, A. Bandyopadhyay, S. Bose, L. O'Donoghue, and C. Charitidis, 'Additive manufacturing: scientific and technological challenges, market uptake and opportunities', *Mater. today*, vol. 21, no. 1, pp. 22–37, 2018.

[33] C. Holt, L. Edwards, L. Keyte, F. Moghaddam, and B. Townsend, ‘Construction 3D printing’, in *3D Concrete Printing Technology*, Elsevier, 2019, pp. 349–370.

[34] V. Kumar, B. R. Isanaka, S. Gupta, and V. Kushvaha, ‘Future Trends and Technologies in Additive and Substractive Manufacturing’, *Addit. Subtractive Manuf. Compos.*, pp. 227–247, 2021.

[35] A. Du Plessis *et al.*, ‘Properties and applications of additively manufactured metallic cellular materials: A review’, *Prog. Mater. Sci.*, vol. 125, p. 100918, 2022.

[36] I. Campbell, D. Bourell, and I. Gibson, ‘Additive manufacturing: rapid prototyping comes of age’, *Rapid Prototyp. J.*, vol. 18, no. 4, pp. 255–258, 2012.

[37] Y. Zhang, S. Jedeck, L. Yang, and L. Bai, ‘Modeling and analysis of the on-demand spare parts supply using additive manufacturing’, *Rapid Prototyp. J.*, vol. 25, no. 3, pp. 473–487, 2019.

[38] S. Ford and M. Despeisse, ‘Additive manufacturing and sustainability: an exploratory study of the advantages and challenges’, *J. Clean. Prod.*, vol. 137, pp. 1573–1587, 2016.

[39] T. Pereira, J. V Kennedy, and J. Potgieter, ‘A comparison of traditional manufacturing vs additive manufacturing, the best method for the job’, *Procedia Manuf.*, vol. 30, pp. 11–18, 2019.

[40] J. P. Davim, *Additive and Subtractive Manufacturing: Emergent Technologies*, vol. 4. Walter de Gruyter GmbH & Co KG, 2020.

[41] A. Nazir *et al.*, ‘Multi-material additive manufacturing: A systematic review of design, properties, applications, challenges, and 3D Printing of materials and cellular metamaterials’, *Mater. Des.*, p. 111661, 2023.

[42] M. Langelaar, ‘Topology optimization of 3D self-supporting structures for additive manufacturing’, *Addit. Manuf.*, vol. 12, pp. 60–70, 2016.

[43] M. B. Kumar and P. Sathiya, ‘Methods and materials for additive manufacturing: A critical review on advancements and challenges’, *Thin-Walled Struct.*, vol. 159, p. 107228, 2021.

[44] T. N. A. T. Rahim, A. M. Abdullah, and H. Md Akil, ‘Recent developments in fused deposition modeling-based 3D printing of polymers and their composites’, *Polym. Rev.*, vol. 59, no. 4, pp. 589–624, 2019.

[45] K. Thrimurthulu, P. M. Pandey, and N. V. Reddy, ‘Optimum part deposition orientation in fused deposition modeling’, *Int. J. Mach. Tools Manuf.*, vol. 44, no. 6, pp. 585–594, 2004.

[46] A. Standard, ‘F2792-12a" Terminology for Additive Manufacturing Technologies". ASTM International. West Conshohocken, PA, DOI: 10.1520/F2792-12A’. 2012.

[47] O. Doğan and M. S. Kamer, ‘Farklı üretim parametreleri kullanılarak 3B yazıcı ile üretilen test numunelerinin sürünme davranışlarının deneysel olarak incelenmesi’, *Gazi Üniversitesi Mühendislik Mimar. Fakültesi Derg.*, vol. 38, no. 3, pp. 1839–1848.

[48] B. Ergene and B. YALÇIN, ‘Eriyik yığma modelleme (EYM) ile üretilen çeşitli hücresel yapıların mekanik performanslarının incelenmesi’, *Gazi Üniversitesi Mühendislik Mimar. Fakültesi Derg.*, vol. 38, no. 1, pp. 201–218, 2023.

[49] R. Singh and J. P. Davim, *Additive Manufacturing: Applications and Innovations*. CRC Press, 2018.

[50] A. J. Sheoran and H. Kumar, ‘Fused Deposition modeling process parameters optimization and effect on mechanical properties and part quality: Review and reflection on present research’, *Mater. Today Proc.*, vol. 21, pp. 1659–1672, 2020.

[51] A. Manoj, M. Bhuyan, S. R. Banik, and M. R. Sankar, ‘Review on particle emissions during fused deposition modeling of acrylonitrile butadiene styrene and polylactic acid polymers’, *Mater. Today Proc.*, vol. 44, pp. 1375–1383, 2021.

[52] M. ERMURAT and M. E. GEBEL, ‘Kompozit eklemeli imalat için polimer matrisli sürekli fiber takviyeli kompozit parça üretilebilirliğinin araştırılması’, *Gazi Üniversitesi Mühendislik Mimar. Fakültesi Derg.*, vol. 36, no. 1, pp. 57–68, 2021.

[53] X. Wang, M. Jiang, Z. Zhou, J. Gou, and D. Hui, ‘3D printing of polymer matrix composites: A review and prospective’, *Compos. Part B Eng.*, vol. 110, pp. 442–458, 2017.

[54] N. E. Zander, ‘Recycled polymer feedstocks for material extrusion additive manufacturing’, in *Polymer-Based Additive Manufacturing: Recent Developments*, ACS Publications, 2019, pp. 37–51.

[55] K. G. Mostafa, C. Montemagno, and A. J. Qureshi, ‘Strength to cost ratio analysis of FDM Nylon 12 3D Printed Parts’, *Procedia Manuf.*, vol. 26, pp. 753–762, 2018.

[56] H. R. Kricheldorf, I. Kreiser-Saunders, and C. Boettcher, ‘Polylactones: 31. Sn (II) octoate-initiated polymerization of L-lactide: a mechanistic study’, *Polymer (Guildf).*, vol. 36, no. 6, pp. 1253–1259, 1995.

[57] R. Rado and P. Zelenak, ‘Crosslinking of polyethylene’, *Int. Polym. Sci. Technol.*, vol. 19, no. 6, pp. 33–47, 1992.

[58] M. Yilmaz, N. Yilmaz, A. Kılıc, and H. Mazı, ‘Investigation of Manufacturability of in-situ crosslinked Polylactic Acid (PLA) and Peroxide composite in additive manufacturing method’, *J. Fac. Eng. Archit. Gazi Univ.*.

[59] M. Yilmaz, N. F. Yilmaz, and M. F. Kalkan, ‘Rheology, Crystallinity, and Mechanical Investigation of Interlayer Adhesion Strength by Thermal Annealing of Polyetherimide (PEI/ULTEM 1010) Parts Produced by 3D Printing’, *J. Mater. Eng. Perform.*, pp. 1–10, 2022.

[60] M. Yilmaz and N. F. Yilmaz, ‘Effects of raster angle in single-and multi-oriented layers for the production of polyetherimide (PEI/ULTEM 1010) parts with fused deposition modelling’, *Mater. Test.*, vol. 64, no. 11, pp. 1651–1661, 2022.

[61] Y. Wang *et al.*, ‘3D-printing of segregated carbon nanotube/polylactic acid composite with enhanced electromagnetic interference shielding and mechanical performance’, *Mater. Des.*, vol. 197, p. 109222, 2021.

[62] M. Nikzad, S. H. Masood, and I. Sbarski, ‘Thermo-mechanical properties of a highly filled polymeric composites for fused deposition modeling’, *Mater. Des.*, vol. 32, no. 6, pp. 3448–3456, 2011.

[63] C. M. Shemelya *et al.*, ‘Mechanical, electromagnetic, and X-ray shielding characterization of a 3D printable tungsten–polycarbonate polymer matrix composite for space-based applications’, *J. Electron. Mater.*, vol. 44, pp. 2598–2607, 2015.

[64] S. N. H. Mazlan, A. Z. Abdul Kadir, M. R. Alkahari, and T. K. Land, ‘Accuracy evaluation of thin wall features fabricated by fused deposition modeling using reinforced composite materials’, *Prog. Addit. Manuf.*, pp. 1–10, 2023.

[65] S. Hwang, E. I. Reyes, K. Moon, R. C. Rumpf, and N. S. Kim, 'Thermo-mechanical characterization of metal/polymer composite filaments and printing parameter study for fused deposition modeling in the 3D printing process', *J. Electron. Mater.*, vol. 44, pp. 771–777, 2015.

[66] K. Boparai, R. Singh, and H. Singh, 'Comparison of tribological behaviour for Nylon6-Al-Al2O3 and ABS parts fabricated by fused deposition modelling: This paper reports a low cost composite material that is more wear-resistant than conventional ABS', *Virtual Phys. Prototyp.*, vol. 10, no. 2, pp. 59–66, 2015.

[67] W. Zhong, F. Li, Z. Zhang, L. Song, and Z. Li, 'Short fiber reinforced composites for fused deposition modeling', *Mater. Sci. Eng. A*, vol. 301, no. 2, pp. 125–130, 2001.

[68] D. Yadav, D. Chhabra, R. K. Gupta, A. Phogat, and A. Ahlawat, 'Modeling and analysis of significant process parameters of FDM 3D printer using ANFIS', *Mater. Today Proc.*, vol. 21, pp. 1592–1604, 2020.

[69] I. M. Alarifi, 'PETG/carbon fiber composites with different structures produced by 3D printing', *Polym. Test.*, vol. 120, p. 107949, 2023.

[70] A. El Magri, K. El Mabrouk, S. Vaudreuil, and M. E. Touhami, 'Mechanical properties of CF-reinforced PLA parts manufactured by fused deposition modeling', *J. Thermoplast. Compos. Mater.*, vol. 34, no. 5, pp. 581–595, 2021.

[71] X. Tian, T. Liu, C. Yang, Q. Wang, and D. Li, 'Interface and performance of 3D printed continuous carbon fiber reinforced PLA composites', *Compos. Part A Appl. Sci. Manuf.*, vol. 88, pp. 198–205, 2016.

[72] A. D. Pertuz, S. Díaz-Cardona, and O. A. González-Estrada, 'Static and fatigue behaviour of continuous fibre reinforced thermoplastic composites manufactured by fused deposition modelling technique', *Int. J. Fatigue*, vol. 130, p. 105275, 2020.

[73] A. G. Andreopoulos and E. M. Kampouris, 'Mechanical properties of crosslinked polyethylene', *J. Appl. Polym. Sci.*, vol. 31, no. 4, pp. 1061–1068, 1986.

[74] W. K. Wong and D. C. Varrall, 'Role of molecular structure on the silane crosslinking of polyethylene: the importance of resin molecular structure change during silane grafting', *Polymer (Guildf).*, vol. 35, no. 25, pp. 5447–5452, 1994.

[75] H. A. Khonakdar, J. Morshedian, U. Wagenknecht, and S. H. Jafari, ‘An investigation of chemical crosslinking effect on properties of high-density polyethylene’, *Polymer (Guildf).*, vol. 44, no. 15, pp. 4301–4309, 2003.

[76] C. Yamoum, J. Maia, and R. Magaraphan, ‘Rheological and thermal behavior of PLA modified by chemical crosslinking in the presence of ethoxylated bisphenol A dimethacrylates’, *Polym. Adv. Technol.*, vol. 28, no. 1, pp. 102–112, 2017.

[77] R. Zhang, C. Cai, Q. Liu, and S. Hu, ‘Enhancing the melt strength of poly (lactic acid) via micro-crosslinking and blending with poly (butylene adipate-co-butylene terephthalate) for the preparation of foams’, *J. Polym. Environ.*, vol. 25, no. 4, pp. 1335–1341, 2017.

[78] L. Zhu *et al.*, ‘Crosslinked polyetherimide nanocomposites with superior energy storage achieved via trace Al2O3 nanoparticles’, *Compos. Sci. Technol.*, vol. 223, p. 109421, 2022.

[79] H. Bi, G. Ye, H. Sun, Z. Ren, T. Gu, and M. Xu, ‘Mechanically robust, shape memory, self-healing and 3D printable thermoreversible cross-linked polymer composites toward conductive and biomimetic skin devices applications’, *Addit. Manuf.*, vol. 49, p. 102487, 2022.

[80] J. B. Mietner, S. Willruth, R. Komban, C. Gimmler, B. Nehmeh, and J. R. G. Navarro, ‘Polymer-Modified Cellulose Nanofibrils Cross-Linked with Cobalt Iron Oxide Nanoparticles as a Gel Ink for 3D Printing Objects with Magnetic and Electrochemical Properties’, *Fibers*, vol. 11, no. 1, p. 2, 2022.

[81] M. Sharma, V. Sharma, and P. Kala, ‘Optimization of process variables to improve the mechanical properties of FDM structures’, in *Journal of Physics: Conference Series*, 2019, vol. 1240, no. 1, p. 12061.

[82] S. R. Rajpurohit and H. K. Dave, ‘Effect of process parameters on tensile strength of FDM printed PLA part’, *Rapid Prototyp. J.*, 2018.

[83] J. M. Chacón, M. A. Caminero, E. García-Plaza, and P. J. Núñez, ‘Additive manufacturing of PLA structures using fused deposition modelling: Effect of process parameters on mechanical properties and their optimal selection’, *Mater. Des.*, vol. 124, pp. 143–157, 2017.

[84] O. A. Mohamed, S. H. Masood, and J. L. Bhowmik, ‘Experimental investigation of time-dependent mechanical properties of PC-ABS prototypes processed by FDM additive manufacturing process’, *Mater. Lett.*, vol. 193, pp. 58–62, 2017.

[85] M. Samykano, S. K. Selvamani, K. Kadirgama, W. K. Ngui, G. Kanagaraj, and K. Sudhakar, ‘Mechanical property of FDM printed ABS: influence of printing parameters’, *Int. J. Adv. Manuf. Technol.*, vol. 102, no. 9–12, pp. 2779–2796, 2019.

[86] L. P. T. Huynh, H. A. Nguyen, H. Q. Nguyen, L. K. H. Phan, and T. T. Tran, ‘Effect of Process Parameters on Mechanical Strength of Fabricated Parts using the Fused Deposition Modelling Method’, vol. 36, no. 8, pp. 705–712, 2019.

[87] G. Taylor *et al.*, ‘Flexural behavior of additively manufactured Ultem 1010: experiment and simulation’, *Rapid Prototyp. J.*, 2018.

[88] K. P. Motaparti, ‘Effect of build parameters on mechanical properties of ultem 9085 parts by fused deposition modeling’, 2016.

[89] P. Han, A. Tofangchi, A. Deshpande, S. Zhang, and K. Hsu, ‘An approach to improve interface healing in FFF-3D printed Ultem 1010 using laser pre-deposition heating’, *Procedia Manuf.*, vol. 34, pp. 672–677, 2019.

[90] S. Singh, M. Singh, C. Prakash, M. K. Gupta, M. Mia, and R. Singh, ‘Optimization and reliability analysis to improve surface quality and mechanical characteristics of heat-treated fused filament fabricated parts’, *Int. J. Adv. Manuf. Technol.*, vol. 102, no. 5–8, pp. 1521–1536, 2019.

[91] J. T. Belter and A. M. Dollar, ‘Strengthening of 3D printed fused deposition manufactured parts using the fill compositing technique’, *PLoS One*, vol. 10, no. 4, 2015.

[92] S. Bhandari, R. A. Lopez-Anido, and D. J. Gardner, ‘Enhancing the interlayer tensile strength of 3D printed short carbon fiber reinforced PETG and PLA composites via annealing’, *Addit. Manuf.*, vol. 30, p. 100922, Dec. 2019, doi: 10.1016/j.addma.2019.100922.

[93] M. H. Ali, N. Mir-Nasiri, and W. L. Ko, ‘Multi-nozzle extrusion system for 3D printer and its control mechanism’, *Int. J. Adv. Manuf. Technol.*, vol. 86, pp. 999–1010, 2016.

[94] Y. J. Yoon, M. Yon, S. E. Jung, and S. K. Gupta, 'Development of three-nozzle extrusion system for conformal multi-resolution 3d printing with a robotic manipulator', in *International Design Engineering Technical Conferences and Computers and Information in Engineering Conference*, 2019, vol. 59179, p. V001T02A024.

[95] P. Zhang, P. Xu, S. Chung, S. Bandari, and M. A. Repka, 'Fabrication of bilayer tablets using hot melt extrusion-based dual-nozzle fused deposition modeling 3D printing', *Int. J. Pharm.*, vol. 624, p. 121972, 2022.

[96] H. Mei, Z. Ali, Y. Yan, I. Ali, and L. Cheng, 'Influence of mixed isotropic fiber angles and hot press on the mechanical properties of 3D printed composites', *Addit. Manuf.*, vol. 27, pp. 150–158, 2019.

[97] Stratasys, 'No Title', 2023. https://www.stratasys.com/en/3d-printers/printer-catalog/fdm-printers/fortus-450mc/

[98] A. Gebhardt and J.-S. Hötter, *Additive manufacturing: 3D printing for prototyping and manufacturing*. Carl Hanser Verlag GmbH Co KG, 2016.

[99] V. D. I. 3405, 'Additive Manufacturing Processes, Rapid Manufacturing—Basics, Definitions, Processes', 2014.

[100] F. Laverne, F. Segonds, and P. Dubois, 'Fabrication additive-Principes généraux', *Tech. l'Ingénieur*, pp. 1–15, 2016.

[101] A. Ambrosi and M. Pumera, '3D-printing technologies for electrochemical applications', *Chem. Soc. Rev.*, vol. 45, no. 10, pp. 2740–2755, 2016.

[102] O. J. Munz, 'Photo-glyph recording', *Patent, US*, vol. 2, 1951.

[103] Y. A. A. Dobah and Y. A. A. Dobah, 'Multiscale natural fibres and architected reinforced thermoplastics', *Biotechnol Adv*, vol. 32, no. 8, pp. 1494–1505, 2014.

[104] O. Abdulhameed, A. Al-Ahmari, W. Ameen, and S. H. Mian, 'Additive manufacturing: Challenges, trends, and applications', *Adv. Mech. Eng.*, vol. 11, no. 2, p. 1687814018822880, 2019.

[105] J. Jiang, 'A novel fabrication strategy for additive manufacturing processes', *J. Clean. Prod.*, vol. 272, p. 122916, 2020.

[106] T. Wohlers and T. Gornet, 'History of additive manufacturing', *Wohlers Rep.*, vol. 24, no. 2014, p. 118, 2014.

[107] M. Shellabear and O. Nyrhilä, 'DMLS-Development history and state of the art', *Laser Assist. netshape Eng. 4, Proc. 4th LANE*, pp. 21–24, 2004.

[108] Ö. Gökhan, 'Eklemeli üretim teknolojileri üzerine bir derleme', *Niğde Ömer*

Halisdemir Üniversitesi Mühendislik Bilim. Derg., vol. 9, no. 1, pp. 606–621, 2020.

[109] E. Din, 'ISO/ASTM 52900: 2017-06 additive manufacturing—general principles—terminology (ISO/ASTM 52900: 2015)', *Ger. Version EN ISO/ASTM*, vol. 52900, 2017.

[110] S. C. Ligon, R. Liska, J. Stampfl, M. Gurr, and R. Mülhaupt, 'Polymers for 3D printing and customized additive manufacturing', *Chem. Rev.*, vol. 117, no. 15, pp. 10212–10290, 2017.

[111] N. Travitzky *et al.*, 'Additive manufacturing of ceramic-based materials', *Adv. Eng. Mater.*, vol. 16, no. 6, pp. 729–754, 2014.

[112] J. J. Lewandowski and M. Seifi, 'Metal additive manufacturing: a review of mechanical properties', *Annu. Rev. Mater. Res.*, vol. 46, pp. 151–186, 2016.

[113] B. Redwood, F. Schöffer, and B. Garret, *The 3D printing handbook: technologies, design and applications*. 3D Hubs, 2017.

[114] J. Comb, W. Priedeman, and P. W. Turley, 'FDM® Technology process improvements', in *1994 international solid freeform fabrication symposium*, 1994.

[115] K. Das, P. Tandon, and A. Singh, '3D PRINTING–IMAGING THE FUTURE LAYER BY LAYER', *J. Contemp. Orthod.*, vol. 4, no. 3, pp. 44–48, 2020.

[116] J. Y. Wong and A. C. Pfahnl, '3D printing of surgical instruments for long-duration space missions', *Aviat. Space. Environ. Med.*, vol. 85, no. 7, pp. 758–763, 2014.

[117] P. Bere, C. Neamtu, and R. Udroiu, 'Novel Method for the Manufacture of Complex CFRP Parts Using FDM-based Molds', *Polymers (Basel).*, vol. 12, no. 10, p. 2220, 2020.

[118] L. Novakova-Marcincinova, J. Novak-Marcincin, J. Barna, and J. Torok, 'Special materials used in FDM rapid prototyping technology application', in *2012 IEEE 16th International Conference on Intelligent Engineering Systems (INES)*, 2012, pp. 73–76.

[119] X. Han *et al.*, 'Carbon fiber reinforced PEEK composites based on 3D-printing technology for orthopedic and dental applications', *J. Clin. Med.*, vol. 8, no. 2, p. 240, 2019.

[120] R. Sharma, R. Singh, R. Penna, and F. Fraternali, 'Investigations for mechanical properties of Hap, PVC and PP based 3D porous structures obtained through biocompatible FDM filaments', *Compos. Part B Eng.*, vol. 132, pp. 237–243, 2018.

[121] Y. Zhao, K. Zhao, Y. Li, and F. Chen, 'Mechanical characterization of biocompatible PEEK by FDM', *J. Manuf. Process.*, vol. 56, pp. 28–42, 2020.

[122] P. Rider, Ž. P. Kačarević, S. Alkildani, S. Retnasingh, R. Schnettler, and M. Barbeck, 'Additive manufacturing for guided bone regeneration: A perspective for alveolar ridge augmentation', *Int. J. Mol. Sci.*, vol. 19, no. 11, p. 3308, 2018.

[123] Q. Wang, M. Gao, L. Li, Z. Ma, and C. Liu, 'Emergy-based environmental impact evaluation and modeling of selective laser melting', *Int. J. Adv. Manuf. Technol.*, vol. 115, no. 4, pp. 1155–1169, 2021.

[124] L. E. Murr and S. M. Gaytan, 'Electron beam melting', 2014.

[125] A. A. Konta, M. García-Piña, and D. R. Serrano, 'Personalised 3D printed medicines: which techniques and polymers are more successful?', *Bioengineering*, vol. 4, no. 4, p. 79, 2017.

[126] T. T. Wohlers, I. Campbell, O. Diegel, R. Huff, and J. Kowen, *Wohlers Report 2022 3D Printing and Additive Manufacturing Global State of the Industry*. 2022.

[127] J. Izdebska-Podsiadły, *Polymers for 3D Printing: Methods, Properties, and Characteristics*. William Andrew, 2022.

[128] P. Nandwana, A. M. Elliott, D. Siddel, A. Merriman, W. H. Peter, and S. S. Babu, 'Powder bed binder jet 3D printing of Inconel 718: Densification, microstructural evolution and challenges☆', *Curr. Opin. Solid State Mater. Sci.*, vol. 21, no. 4, pp. 207–218, 2017.

[129] A. Mostafaei *et al.*, 'Binder jet 3D printing—Process parameters, materials, properties, modeling, and challenges', *Prog. Mater. Sci.*, vol. 119, p. 100707, 2021.

[130] T. D. Ngo, A. Kashani, G. Imbalzano, K. T. Q. Nguyen, and D. Hui, 'Additive manufacturing (3D printing): A review of materials, methods, applications and challenges', *Compos. Part B Eng.*, vol. 143, pp. 172–196, 2018.

[131] W. Gao *et al.*, 'The status, challenges, and future of additive manufacturing in engineering', *Comput. Des.*, vol. 69, pp. 65–89, 2015.

[132] Stratasys, ‘ULTEM 1010 Resin ULTEM 1010 Resin’. https://arti90.com/wp-content/uploads/2018/01/Spec-Sheet-ULTEM-1010-EN-A4-1.pdf

[133] H. Wu, M. Sulkis, J. Driver, A. Saade-Castillo, A. Thompson, and J. H. Koo, ‘Multi-functional ULTEM^{TM} 1010 composite filaments for additive manufacturing using Fused Filament Fabrication (FFF)’, *Addit. Manuf.*, vol. 24, pp. 298–306, 2018.

[134] U. Modi and S. Prakash, ‘Wettability of 3D printed polylactic acid (PLA) parts’, in *AIP Conference Proceedings*, 2019, vol. 2148, no. 1, p. 30052.

[135] A. J. Arockiam, K. Subramanian, R. G. Padmanabhan, R. Selvaraj, D. K. Bagal, and S. Rajesh, ‘A review on PLA with different fillers used as a filament in 3D printing’, *Mater. Today Proc.*, vol. 50, pp. 2057–2064, 2022.

[136] M. G. Jang, S. C. Ryu, K. J. Juhn, S. K. Kim, and W. N. Kim, ‘Effects of carbon fiber modification with multiwall CNT on the electrical conductivity and EMI shielding effectiveness of polycarbonate/carbon fiber/CNT composites’, *J. Appl. Polym. Sci.*, vol. 136, no. 14, p. 47302, 2019.

[137] S. PC Filament, F D M Thermoplastic, ‘Antero 800NA FDM Thermoplastic Filament Contents ’:, *Stratasys*, 2023. https://www.stratasys.com

[138] C. Hohimer, J. Christ, N. Aliheidari, C. Mo, and A. Ameli, ‘3D printed thermoplastic polyurethane with isotropic material properties’, in *Behavior and Mechanics of Multifunctional Materials and Composites 2017*, 2017, vol. 10165, pp. 213–221.

[139] A. C. Abbott, G. P. Tandon, R. L. Bradford, H. Koerner, and J. W. Baur, ‘Process-structure-property effects on ABS bond strength in fused filament fabrication’, *Addit. Manuf.*, vol. 19, pp. 29–38, 2018.

[140] R. Wichniarek, A. Hamrol, W. Kuczko, F. Górski, and M. Rogalewicz, ‘ABS filament moisture compensation possibilities in the FDM process’, *CIRP J. Manuf. Sci. Technol.*, vol. 35, pp. 550–559, 2021.

[141] M. Domingo-Espin, J. A. Travieso-Rodriguez, R. Jerez-Mesa, and J. Lluma-Fuentes, ‘Fatigue performance of ABS specimens obtained by fused filament fabrication’, *Materials (Basel).*, vol. 11, no. 12, p. 2521, 2018.

[142] R. Singh, S. Singh, and K. Mankotia, ‘Development of ABS based wire as feedstock filament of FDM for industrial applications’, *Rapid Prototyp. J.*, 2016.

[143] C. Ziemian, M. Sharma, and S. Ziemian, ‘Anisotropic mechanical properties of ABS parts fabricated by fused deposition modelling’, *Mech. Eng.*, vol. 23, pp. 159–180, 2012.

[144] S. Khabia and K. K. Jain, ‘Comparison of mechanical properties of components 3D printed from different brand ABS filament on different FDM printers’, *Mater. Today Proc.*, vol. 26, pp. 2907–2914, 2020.

[145] P. Azimi, D. Zhao, C. Pouzet, N. E. Crain, and B. Stephens, ‘Emissions of ultrafine particles and volatile organic compounds from commercially available desktop three-dimensional printers with multiple filaments’, *Environ. Sci. Technol.*, vol. 50, no. 3, pp. 1260–1268, 2016.

[146] P. Byrley, M. A. G. Wallace, W. K. Boyes, and K. Rogers, ‘Particle and volatile organic compound emissions from a 3D printer filament extruder’, *Sci. Total Environ.*, vol. 736, p. 139604, 2020.

[147] A. Y. Davis, Q. Zhang, J. P. S. Wong, R. J. Weber, and M. S. Black, ‘Characterization of volatile organic compound emissions from consumer level material extrusion 3D printers’, *Build. Environ.*, vol. 160, p. 106209, 2019.

[148] S. S. Pesetskii, B. Jurkowski, and V. N. Koval, ‘Polycarbonate/polyalkylene terephthalate blends: Interphase interactions and impact strength’, *J. Appl. Polym. Sci.*, vol. 84, no. 6, pp. 1277–1285, 2002.

[149] D. Kyriacos, ‘Polycarbonates’, in *Brydson’s Plastics Materials*, Elsevier, 2017, pp. 457–485.

[150] M. J. Reich, A. L. Woern, N. G. Tanikella, and J. M. Pearce, ‘Mechanical properties and applications of recycled polycarbonate particle material extrusion-based additive manufacturing’, *Materials (Basel).*, vol. 12, no. 10, p. 1642, 2019.

[151] J. T. Cantrell *et al.*, ‘Experimental characterization of the mechanical properties of 3D-printed ABS and polycarbonate parts’, *Rapid Prototyp. J.*, vol. 23, no. 4, pp. 811–824, 2017.

[152] N. Vidakis, M. Petousis, E. Velidakis, M. Spiridaki, and J. D. Kechagias, ‘Mechanical performance of fused filament fabricated and 3d-printed polycarbonate polymer and polycarbonate/cellulose nanofiber nanocomposites’, *Fibers*, vol. 9, no. 11, p. 74, 2021.

[153] N. Arias and F. Jaramillo, ‘Highly reflective aluminum films on polycarbonate substrates by physical vapor deposition’, *Appl. Surf. Sci.*, vol. 505, p. 144596, 2020.

[154] D. Kodali, C. O. Umerah, M. O. Idrees, S. Jeelani, and V. K. Rangari, ‘Fabrication and characterization of polycarbonate-silica filaments for 3D printing applications’, *J. Compos. Mater.*, vol. 55, no. 30, pp. 4575–4584, 2021.

[155] J. M. Puigoriol-Forcada, A. Alsina, A. G. Salazar-Martín, G. Gomez-Gras, and M. A. Pérez, ‘Flexural fatigue properties of polycarbonate fused-deposition modelling specimens’, *Mater. Des.*, vol. 155, pp. 414–421, 2018.

[156] I. M. Balashova, R. P. Danner, P. S. Puri, and J. L. Duda, ‘Solubility and diffusivity of solvents and nonsolvents in polysulfone and polyetherimide’, *Ind. Eng. Chem. Res.*, vol. 40, no. 14, pp. 3058–3064, 2001.

[157] A. Marzola, E. Mussi, and F. Uccheddu, ‘3D Printed Materials for High Temperature Applications’, in *International Conference on Design, Simulation, Manufacturing: The Innovation Exchange*, 2019, pp. 936–947.

[158] V. Kostopoulos, A. Kotrotsos, K. Fouriki, A. Kalarakis, and D. Portan, ‘Fabrication and Characterization of Polyetherimide Electrospun Scaffolds Modified with Graphene Nano-Platelets and Hydroxyapatite Nano-Particles’, *Int. J. Mol. Sci.*, vol. 21, no. 2, p. 583, 2020.

[159] F. Fischer, ‘Thermoplastics: the best choice for 3D printing’, *White Pap. Strat. Inc., Edn Prairie, MN*, 2011.

[160] A. Slonov, I. Musov, A. Zhansitov, E. Rzhevskaya, D. Khakulova, and S. Khashirova, ‘The Effect of Modification on the Properties of Polyetherimide and Its Carbon-Filled Composite’, *Polymers (Basel).*, vol. 12, no. 5, p. 1056, 2020.

[161] A. Yıldız, U. Emanetoğlu, E. O. Yenigun, and H. Cebeci, ‘Towards optimized carbon nanotubes (CNTs) reinforced polyetherimide (PEI) 3D printed structures: A comparative study on testing standards’, *Compos. Struct.*, vol. 296, p. 115853, 2022.

[162] B. Böhringer, D. Schilo, W. Birkenfeld, and W. Odenthal, ‘New filaments and fibres of polyetherimide’, in *Makromolekulare Chemie. Macromolecular Symposia*, 1991, vol. 50, no. 1, pp. 31–39.

[163] A. Chueca de Bruijn, G. Gómez-Gras, and M. A. Pérez, ‘A comparative analysis of chemical, thermal, and mechanical post-process of fused filament fabricated polyetherimide parts for surface quality enhancement’, *Materials (Basel).*, vol. 14, no. 19, p. 5880, 2021.

[164] O. Kaynan, A. Yıldız, Y. E. Bozkurt, E. O. Yenigun, and H. Cebeci, ‘Electrically conductive high-performance thermoplastic filaments for fused filament fabrication’, *Compos. Struct.*, vol. 237, p. 111930, 2020.

[165] M.-H. Lee, J.-R. Chen, M. Das, T.-F. Hsieh, and C.-M. Shu, ‘Thermokinetic parameter evaluation by DSC and TAM III along with accountability of mass loss by TG from the thermal decomposition analyses of benzoyl peroxide’, *J. Therm. Anal. Calorim.*, vol. 122, pp. 1143–1150, 2015.

[166] M. Sagransky, B. A. Yentzer, and S. R. Feldman, ‘Benzoyl peroxide: a review of its current use in the treatment of acne vulgaris’, *Expert Opin. Pharmacother.*, vol. 10, no. 15, pp. 2555–2562, 2009.

[167] R. Aarthi, S. Ramalingam, S. Periandy, and K. Senthil Kannan, ‘Molecular structure-associated pharmacodynamic investigation on benzoyl peroxide using spectroscopic and quantum computational tools’, *J. Taibah Univ. Sci.*, vol. 12, no. 1, pp. 104–122, 2018.

[168] Der-mix, ‘DERMİX JAGUAR PLUS’. https://dermix.com.tr/images/product/files/JAGUAR_PLUS.pdf

[169] Der-mix, ‘Dermix_Jaguar.pdf’. https://dermix.com.tr/images/product/files/Dermix_Jaguar.pdf

[170] Tecnical properties, ‘Stainless Fluid Pass Otomatik Dozajlama Tabancası Technical Properties’.

[171] cyconozzles, ‘The Formation Principle Of Nozzle Spray Shape’, *January 21*, 2022. https://www.cyconozzles.com/the-formation-principle-of-nozzle-spray-shape/

[172] ‘NEMA 17 STEPPER MOTOR’, 2023. https://www.circuitspecialists.com

[173] A. D638-14, ‘ASTM International’, *Stand. test method tensile Prop. Plast.*, 2014.

[174] C.-S. Wu and H.-T. Liao, ‘A new biodegradable blends prepared from polylactide and hyaluronic acid’, *Polymer (Guildf).*, vol. 46, no. 23, pp. 10017–10026, 2005.

[175] P. Singla, R. Mehta, D. Berek, and S. N. Upadhyay, 'Microwave assisted synthesis of poly (lactic acid) and its characterization using size exclusion chromatography', *J. Macromol. Sci. Part A*, vol. 49, no. 11, pp. 963–970, 2012.

[176] B. W. Chieng, I. N. Azowa, W. Yunus, M. D. Z. Wan, and M. Z. Hussein, 'Effects of graphene nanopletelets on poly (lactic acid)/poly (ethylene glycol) polymer nanocomposites', in *Advanced Materials Research*, 2014, vol. 1024, pp. 136–139.

[177] M. Takamura, T. Nakamura, T. Takahashi, and K. Koyama, 'Effect of type of peroxide on cross-linking of poly (l-lactide)', *Polym. Degrad. Stab.*, vol. 93, no. 10, pp. 1909–1916, 2008.

[178] F. R. Beltrán, C. Infante, M. U. de la Orden, and J. M. Urreaga, 'Mechanical recycling of poly (lactic acid): Evaluation of a chain extender and a peroxide as additives for upgrading the recycled plastic.', *J. Clean. Prod.*, vol. 219, pp. 46–56, 2019.

[179] X. Wang, L. Zhao, J. Y. H. Fuh, and H. P. Lee, 'Effect of porosity on mechanical properties of 3D printed polymers: Experiments and micromechanical modeling based on X-ray computed tomography analysis', *Polymers (Basel).*, vol. 11, no. 7, p. 1154, 2019.

[180] N. von Windheim, D. W. Collinson, T. Lau, L. C. Brinson, and K. Gall, 'The influence of porosity, crystallinity and interlayer adhesion on the tensile strength of 3D printed polylactic acid (PLA)', *Rapid Prototyp. J.*, 2021.

[181] A. International, 'ASTM D790− 17-flexural properties of unreinforced and reinforced plastics and electrical insulating materials', 2017.

[182] A. Standard, 'D2240-15 Standard Test Method for Rubber Property–Durometer Hardness', 2015.

[183] L. Távara, V. Mantic, E. Graciani, J. Cañas, and F. París, 'Analysis of a crack in a thin adhesive layer between orthotropic materials: an application to composite interlaminar fracture toughness test', *Comput. Model. Eng. Sci.*, vol. 58, no. 3, pp. 247–270, 2010.

[184] A. Štibler, K. Herrmann, and Z. Šušteri, 'Long-term stability of rubber hardness reference blocks'. HARDMEKO, 2004.

[185] K. Abouzaid, S. Guessasma, S. Belhabib, D. Bassir, and A. Chouaf, 'Printability of co-polyester using fused deposition modelling and related mechanical performance', *Eur. Polym. J.*, vol. 108, pp. 262–273, 2018.

[186] A. K. Sood, R. K. Ohdar, and S. S. Mahapatra, ‘Parametric appraisal of mechanical property of fused deposition modelling processed parts’, *Mater. Des.*, vol. 31, no. 1, pp. 287–295, 2010.

[187] A. Lanzotti, M. Grasso, G. Staiano, and M. Martorelli, ‘The impact of process parameters on mechanical properties of parts fabricated in PLA with an open-source 3-D printer’, *Rapid Prototyp. J.*, 2015.

[188] J. F. Rodrı´ guez, J. P. Thomas, and J. E. Renaud, ‘Design of fused-deposition ABS components for stiffness and strength’, *J. Mech. Des.*, vol. 125, no. 3, pp. 545–551, 2003.

[189] P.-G. de Gennes, ‘Reptation of a polymer chain in the presence of fixed obstacles’, *J. Chem. Phys.*, vol. 55, no. 2, pp. 572–579, 1971.

[190] Y. H. Kim and R. P. Wool, ‘A theory of healing at a polymer-polymer interface’, *Macromolecules*, vol. 16, no. 7, pp. 1115–1120, 1983.

[191] Q. Sun, G. M. Rizvi, C. T. Bellehumeur, and P. Gu, ‘Effect of processing conditions on the bonding quality of FDM polymer filaments’, *Rapid Prototyp. J.*, 2008.

[192] S. Prager and M. Tirrell, ‘The healing process at polymer–polymer interfaces’, *J. Chem. Phys.*, vol. 75, no. 10, pp. 5194–5198, 1981.

[193] T. Ge, M. O. Robbins, D. Perahia, and G. S. Grest, ‘Healing of polymer interfaces: Interfacial dynamics, entanglements, and strength’, *Phys. Rev. E*, vol. 90, no. 1, p. 12602, 2014.

[194] B.-K. Chen, C.-T. Su, M.-C. Tseng, and S.-Y. Tsay, ‘Preparation of polyetherimide nanocomposites with improved thermal, mechanical and dielectric properties’, *Polym. Bull.*, vol. 57, no. 5, pp. 671–681, 2006.

[195] A. Choudhury, ‘Dielectric and piezoelectric properties of polyetherimide/BaTiO3 nanocomposites’, *Mater. Chem. Phys.*, vol. 121, no. 1–2, pp. 280–285, 2010.

[196] R. N. Muthu, S. Rajashabala, and R. Kannan, ‘Synthesis of polyetherimide/halloysite nanotubes (PEI/HNTs) based nanocomposite membrane towards hydrogen storage’, in *AIP Conference Proceedings*, 2018, vol. 1942, no. 1, p. 50107.

[197] M. Owlad, M. K. Aroua, and W. M. A. W. Daud, ‘Hexavalent chromium adsorption on impregnated palm shell activated carbon with polyethyleneimine’, *Bioresour. Technol.*, vol. 101, no. 14, pp. 5098–5103, 2010.

[198] A. D5573-99, ‘Standard practice for classifying failure modes in fiber-reinforced-plastic (FRP) joints’, *Annual Book of ASTM Standards*, vol. 15. p. 2002, 2012.

[199] N. Wang and S. Xia, ‘Cohesive fracture of elastically heterogeneous materials: an integrative modeling and experimental study’, *J. Mech. Phys. Solids*, vol. 98, pp. 87–105, 2017.

[200] A. M. Harris and E. C. Lee, ‘Improving mechanical performance of injection molded PLA by controlling crystallinity’, *J. Appl. Polym. Sci.*, vol. 107, no. 4, pp. 2246–2255, 2008.

[201] M. Zhu *et al.*, ‘Electrospun nanofibers membranes for effective air filtration’, *Macromol. Mater. Eng.*, vol. 302, no. 1, p. 1600353, 2017.

[202] M. Hesami and A. Jalali-Arani, ‘Cold crystallization behavior of poly (lactic acid) in its blend with acrylic rubber; the effect of acrylic rubber content’, *Polym. Int.*, vol. 66, no. 11, pp. 1564–1571, 2017.

[203] C. Yang, X. Tian, D. Li, Y. Cao, F. Zhao, and C. Shi, ‘Influence of thermal processing conditions in 3D printing on the crystallinity and mechanical properties of PEEK material’, *J. Mater. Process. Technol.*, vol. 248, pp. 1–7, 2017.

[204] B. S. Thakkar and L. J. Broutman, ‘Impact strength of polymers. 3: The effect of annealing on cold worked polycarbonates’, *Polym. Eng. Sci.*, vol. 21, no. 3, pp. 155–162, 1981.

[205] J. Cao, M. A. Gharghouri, and P. Nash, ‘Finite-element analysis and experimental validation of thermal residual stress and distortion in electron beam additive manufactured Ti-6Al-4V build plates’, *J. Mater. Process. Technol.*, vol. 237, pp. 409–419, 2016.

[206] Y. Song, Y. Li, W. Song, K. Yee, K.-Y. Lee, and V. L. Tagarielli, ‘Measurements of the mechanical response of unidirectional 3D-printed PLA’, *Mater. Des.*, vol. 123, pp. 154–164, 2017.

[207] A. A. D'Amico, A. Debaie, and A. M. Peterson, 'Effect of layer thickness on irreversible thermal expansion and interlayer strength in fused deposition modeling', *Rapid Prototyp. J.*, 2017.

[208] G. Liao, Z. Li, C. Luan, Z. Wang, X. Yao, and J. Fu, 'Additive Manufacturing of Polyamide 66: Effect of Process Parameters on Crystallinity and Mechanical Properties', *J. Mater. Eng. Perform.*, vol. 31, no. 1, pp. 191–200, 2022.

CURRICULUM VITAE (CV)

General

Name Surname	Musa Yılmaz

Education

Degree	Department	University	Year
BSc	Mechanical Engineering	Gaziantep University	2010-2015
MSc	Mechanical Engineering	Gaziantep University	2015-2017
PhD	Mechanical Engineering	Gaziantep University	2017- 2023

Work Experience

Position	Place of Duty	Year
Lecturer	Gaziantep University	2018- continue

PUBLICATIONS

Parts of the work presented in this thesis have been published elsewhere, or presented at conferences. An index is provided here:

Articles:

1. Yilmaz, M., & Yilmaz, N. F., Effects of raster angle in single-and multi-oriented layers for the production of polyetherimide (PEI/ULTEM 1010) parts with fused deposition modelling. Materials Testing, 64(11), 1651-1661, 2022 (SCIE) https://doi.org/10.1515/mt-2022-0085
2. Yilmaz, M., Yilmaz, N.F., & Kalkan, M.F., Rheology, Crystallinity, and Mechanical Investigation of Interlayer Adhesion Strength by Thermal Annealing of Polyetherimide (PEI/ULTEM 1010) Parts Produced by 3D Printing. J. of Materi Eng and Perform 31, 9900–9909, 2022 (SCIE) https://doi.org/10.1007/s11665-022-07049-z
3. Yilmaz, M., Yilmaz, N.F., Kılıc, A., & Mazi, H., Investigation of Manufacturability of In-Situ Crosslinked Polylactic Acid (PLA) and Peroxide Composite in Additive Manufacturing Method, Journal of the Faculty of Engineering and Architecture of Gazi University, (Accepted in April 2023) (SCIE) https://doi.org/10.17341/gazimmfd.1213974

Conference Papers

1. Yilmaz, M., Yilmaz, N.F., Kılıc, A., & Eyercioglu, Ö., Effect of layer thickness on mechanical properties of 3D-printed polycarbonate polymer by FDM, 4th International Conference on 3D Printing (Additive Manufacturing) Technologyies, 11-14 April, 2019, Antalya/Turkey
2. Yilmaz, N.F., Yilmaz, M., & Eyercioglu, Ö., Effect of raster angle on mechanical properties of 3D printed polycarbonate polymers, 8th International Conference (ICAT'19), 26-30 August, 2019, Sarajevo, Bosnia and Herzegovina

3. Yilmaz, M., Yilmaz, N.F., & Eyercioglu, Ö., A study on process parameter in additive manufacturing, The International Conference of Materials and Engineering Technology (TICMET'19), 10-12 Octaber, 2019, Gaziantep/Turkey